TÉCNICO LISBOA

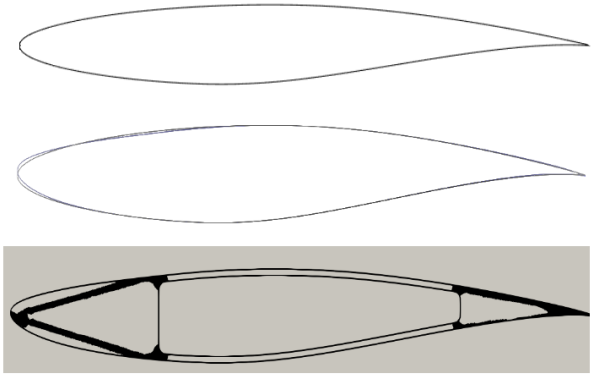

AERODYNAMIC OPTIMISATION OF A CONSTRAINED AEROFOIL'S SHAPE COUPLED WITH AN OPTIMISATION OF ITS INNER STRUCTURAL TOPOLOGY

Isaac Gibert Martínez

Thesis to obtain the Master of Science Degree in

Aerospace Engineering

Supervisors: Prof. Fernando José Parracho Lau
Prof. Frederico José Prata Rente Reis Afonso

Examination Committee

Chairperson: Prof. Filipe Szolnoky Ramos Pinto Cunha
Supervisor: Prof. Fernando José Parracho Lau
Member of the Committee: Prof. Miguel António Lopes de Matos Neves

January 2021

I declare that this document is an original work of my own authorship and that it fulfills all the requirements of the Code of Conduct and Good Practices of the Universidade de Lisboa.

Resumo

O objetivo geral da tese consiste no acoplamento dos processos de otimização aerodinâmica e estrutural recorrendo a diferentes programas de código aberto, *SU2* e *Calculix*, capazes de fornecer simulações robustas e eficientes nestes dois campos. A geometria usada para testar o código aberto é o perfil alar RAE 2822, caso de referência 2D para regimes aerodinâmicos viscosos transónicos, com um caixão de torção a restringir a sua forma no processo de otimização. A resistência aerodinâmica foi inicialmente minimizada para duas configurações diferentes, $M = 0.729$ at $\alpha = 2.31°$ e $M = 0.730$ at $\alpha = 2.79°$ para uma sustentação constante usando o método Free-Form Deformation. Posteriormente é utilizado uma otimização topológica "Bi-directional Evolutionary" de forma a otimizar no ambiente Calculix a estrutura interna do perfil alar previamente otimizado. De modo a aplicar o carregamento obtido na otimização aerodinâmica à estrutura para a otimizar topologicamente, foi desenvolvido um processo de transferência de carregamentos aerodinâmicos. A seguir, uma estratégia de acoplamento sequencial foi aplicada, pois a otimização aerodinâmica representou uma melhoria na distribuição geral de pressão, a qual consequentemente representou uma diminuição em duas ordens de magnitude do estado de tensão e os deslocamentos finais. Em conclusão, o acoplamento sequencial provou ser benéfico, pois a melhoria aerodinâmica permitiu que o estrutura interna se redistribuísse de forma mais eficiente, reduzindo o seu volume interno para 25% do inicial, ao mesmo tempo que proporciona uma estrutura robusta e segura.

Palavras-chave: Aerodynamic Optimisation, CFD, RAE 2822, Topology Optimisation, Calculix, SU2

Abstract

The overall purpose of the work lies on the coupling of two optimisation procedures for the main fields of study, the aerodynamics and the topology layout, by means of different open-source resources, SU2 and *Calculix* respectively, capable to provide robust and efficient simulations in both studied fields. The RAE 2822 geometry used to test the open-source software is the 2D benchmark case for transonic viscous aerodynamic profiles, with the wing-box as a geometric constraint. The aerofoil has been initially drag-minimised for two different configurations, $M = 0.729$ at $\alpha = 2.31°$ and $M = 0.730$ at $\alpha = 2.79°$ while setting a fixed lift constraint using the *Free-Form Deformation* methodology; afterwards, the *Bi-directional Evolutionary Topology Optimisation* was applied to the optimised shape inside the *Calculix* environment. A migratory procedure of the obtained data was required by the topology analysis from the aerodynamic output so as to apply the pressure loads on the aerofoil's surface as concentrated loads. Then, a sequential coupling strategy was followed since the aerodynamic optimisation represented an improvement to the general pressure distribution and, subsequently, it represented a diminishing of two orders of magnitude below for the loading state and the final displacements. Conclusively, the sequential coupling has proved to be beneficial as the aerodynamic improvement allowed the inner layout to redistribute in a more efficient way, reducing its inner surface to a remarkable value of 25% from the original one, while providing a robust and structurally sound design.

Keywords: Aerodynamic Optimisation, CFD, RAE 2822, Topology Optimisation, Calculix, SU2

Contents

List of Tables

List of Figures

Nomenclature

Greek symbols used for Adjoint parameters and variables

ψ	Adjoint variable matrix

Greek symbols used for Evolutionary Shape Optimisation parameters

α	Element sensitivity
$\Delta(i,j)$	Distance between cell's centers
ω	Weighing factor between nodes distance
ρ	Material filling factor [0-1]
σ_e^{VM}	Stress value of the element
σ_{max}^{VM}	Maximal loading state

Greek symbols used for structural parameters and variables

δ_{kl}	Kroenecker delta
ϵ_M	Volumetric strain tensor
ϵ'_{ij}	Shear strain tensor
ϵ_{kl}	Strain tensor
γ	First Lamé parameter
$\sigma_{\mathbf{R}}$	Reference stress tensor
σ	Cauchy stress tensor
μ	Second Lamé parameter
ν	poisson's ratio

Greek symbols used for Mesh Deformation parameters

δq_i	Velocity divergence of two continuous cells

$\mu_{l,m,n}$ Control points modification for the new frame's position

Greek symbols used for Fluid parameters and variables

α Angle of attack

χ Ratio between linear and spatial transport quantities

Δ Divergence

κ Kárman constant

μ Dynamic viscosity

μ_τ Eddy dynamic viscosity

ν_τ Eddy kinematic viscosity

Ω_{ij} Vorticity

ρ Density

σ Prandtl number

$\tilde{\nu}$ Linear transport quantity

Other symbols

$[]^T$ Transpose of the matrix

$[]^{-1}$ Inverse of the matrix

$\frac{\delta f}{\delta \rho}$ Element sensitivity

Latin symbols used for Structural parameters and variables

$\mathbf{M}$ Material conditions

$\mathbf{u}$ Displacements

C_{ijkl} Compliance matrix

E Young Modulus

G Shear modulus

K Bulk modulus

Latin symbols used for Evolutionary Shape Optimisation parameters

$\mathbf{f}$ Load vector

$\mathbf{u}$ Displacement vector

$\overline{H}_j$ Weight factor

C Compliance

c_{ar} Addition criteria

c_{rer} Evolutionary rejection criteria

c_{rr} Rejection criteria

N Set of elements in the filter

r_{min} Filter radius

V Volume

Latin symbols used for Adjoint parameters and variables

D Design variables

L Objective function

N_0 Number of output variables

N_1 Number of input variables

R Residual as a function of the variable and design variables

r Residual

u Variable of the study

Latin symbols used for Mesh Deformation parameters

$\mathbf{p_{l,m,n}}$ Control point position

$\mathbf{X_{ffd}}$ parametrisation of the free-form deformation box

$\vec{F}_i$ Hooke's force of a spring

$\vec{q}_i$ Spring displacement

$\vec{x}_i$ Node displacement

A Deformation matrix

b Bernstein polynomial

k_{ij} Spring's stiffness

l_i Length of the element

l_r Reference Length

M Shape matrix

p Cell distorsion matrix

r Weighting factor

U pure rotation matrix

v_i Number of nodes

Latin symbols used for for Fluid parameters and variables

$\mathbf{b}$ Body forces vector

$\mathbf{u}$ Velocity vector

$\tilde{S}$ Production term in the log-layer

c aerofoil's chord

c_{b1} Production term as a function of the Prandtl number

c_{b2} Second production term as a function of the Prandtl number

c_{v1} Log-layer calibrator

c_{w1} Destruction term near the wall

c_{w2} Destruction term slope limiter

c_{w3} Skin friction calibrator

Cd Drag coefficient

Cl Lift coefficient

Cp Pressure coefficient

d Distance to the wall

f_w Outer boundary layer calibrator for th destruction term

f_{v1} Log-layer calibrator

f_{v2} Production calibrator in the log-layer

g Limiter effect calibrator

l Mixing length

M Mach number

r Control function calibrator

Re	Reynolds number
S_{ij}	Fluid deformation tensor
T	Period of time
t	Time
u'	Fluctuating component of the velocity
U_i	Mean velocity components
u_τ	Friction velocity
x_i	Spatial component
y^*	Dimensionless wall distance
p	pressure

Glossary

BESO	Bi-directional Evolutionary Structural Optimisation is a technique which follows a modification of the *Evolutionary Structural Optimisation* and includes in the algorithm both of the modifications described in the previous method. It can add and remove material in the same process. xii, 6
CAM	Continuous Adjoint Methodology is a gradient-based procedure used to obtain the sensitivity of a design parameter in terms of independent variables by including the cost function term in the integration procedure of the field equations. xii, 3
CFD	Computational Fluid Dynamics is a branch of fluid mechanics which uses numerical methods and algorithms to analyse and solve situations involving fluids flows. xii, 6
CLOAD	Concentrated LOAD is a parameter used in the Calculix environment which recreates the positioning of a constant loading state into one specific point of a geometry. xii, 35
DAM	Discrete Adjoint Methodology is a gradient-based procedure used to obtain the sensitivity of a design parameter in terms of independent variables by embedding insider the field equations the discretisation of the cost function terms. xii, 3
DLOAD	Distributed LOAD is a parameter used in the Calculix environment which recreates the positioning of a constant pressure or mass loading state on a face of a geometry. xii, 35
ESO	Evolutionary Structural Optimisation is a technique employed to optimise the object's material layout for a given set of constraints and conditions, optimising a specific target of the study by adding or removing material. xii, 4, 21
FEA	Finite Element Analysis is a numerical technique used to simulate physical phenomenon such as structural and fluid dynamics, thermal analysis and wave propagation. xii
FEM	Finite Element Method is a numerical approach used to solve partial differential equations in two or three space variables by discretising the domain in small parts, the finite elements.. xii

FFD	Free-Form Deformation boxes are based on enclosing a body with a hull object and transferring a deformation to the embedded geometry using specific parametrisation curves such as *NURBS*. xii, 4, 14
FI	Failure Index is a criteria used to determine if a material is going to fail under a certain loading state, being the value a smaller than 1 a safe design while having a value equal or higher than it a dangerous state. xii, 44
FVM	Finite Volume Method is a discretisation procedure for the approximation of a set of partial differential equations by following the conservation laws. They describe the relations between unknown field variables with respect to variables in the domain. xii, 26
NACA	National Advisory Committee for Aeronautics is a U.S. Federal Agency founded in 1915 to undertake, to promote and institutionalise aeronautical research. In this thesis, this entry refers to the set of airfoil shapes for aircraft designed by this committee. xii, 3
NURBS	Non-Uniform Rational B-Splines is a mathematical model used to represent and create curves and surfaces by means of a distribution of control points and a correspondent weighted value for each of them. xii, 14
PDE	Partial Differential Equations in mathematics is an equation which imposes relations between various partial derivatives of a multivariable function. xii, 3
RANS	Reynolds Averaged Navier-Stokes equations are time-averaged equations which represent the fluidic motion, specially for the turbulent regimes, by decomposing an instantaneous quantity into a time-averaged set and into a fluctuating one. xii, 7
SA	Spalart-Allmaras model is a one-equation model which solves a modelled transport equation by means of the kinematic viscosity. xii, 9
SIMP	Solid Isotropic Material with Penalisation method is a procedure used to predict an optimal material layout given a design space, loading, manufacturing and boundary constraints and performance requirements by means of a constrained density-based study. xii, 4
SLSQP	Sequential List SQuares Programming is a technique created for constrained nonlinear optimisations. It optimises a quadratic version of the objective function subject to a linearised form of the constraints.. xii, 47
SU2	Stanford University Unstructured is a multiphysics simulation and design software developed by Thomas D. Economon, Francisco Palacios, Sean R. Copeland, Trent W. Lukaczyk and Juan J. Alonso and distributed freely in the community. xii, 7

Chapter 1

Introduction

The term '*efficiency*' in the aeronautical industry is gaining more and more weight every passing year as, apart from leading a transversal innovation across all the engineering fields, it is always trying to reach the excellence and perfectionism of its science. Apart from performance efficiency the new aircraft designs have to cope with two of the hardest enemies of the human specie and the world itself have had to face, the climate change and the environmental resources management. This engineering sector is evolving towards a clean energy resource point of view, a high-efficient design and towards the leadership of future environmentally-friendly technologies in the society. In that way, companies such as *AIRBUS* [1], which has emerged recently in the news because of their new hydrogen-powered commercial aircraft concepts which aim a 50% emission reduction, pretend to drive the new investigations of aeronautics towards the consideration of the previous aspects as a primary cause of their work.

Nevertheless, it is not explicitly necessary to rearrange the actual concept of an aircraft so as to provide more efficient designs, even though it is preferred if they are born from a more beneficial idea. By improving the different technologies embedded in the process, it is possible to reach the specified high goals in terms of the new aeronautical field, thus a broad range of possibilities are available for the community to discover, investigate and bring them to life.
Within them, the most renowned areas of improvement are found in the geometry optimisation features [2] [3], combustion and gas exhaust systems [4], and the weight reduction target [5].

In this work, two optimisation approaches will be followed and applied to the RAE 2822 aerofoil considering the study to be bi-dimensional. Moreover, it has been decided to apply a geometric constraint in the study, the one based on the wing-box position in the aerofoil. Both approaches pretend to reduce the fuel consumption but following two alternative paths by just reordering and removing material areas of the aerofoil, yet making it compliant to the structural and aerodynamic requirements. One of them is optimising the aerodynamics of the aerofoil by modifying its geometry for specific flow conditions thus reducing the required thrust power to provide the motion to the aircraft, while the other procedure works in rearranging the material inside the aerofoil aiming at the highest stiffness-to-weight ratio and, therefore, the lowest lift force required to fly the aircraft.

To do so, a sequential point of view has been followed. This means that the optimisations are not carried out in parallel or at the same time, where the optimisation sensitivities are mixed between fields of study, thus any modification may affect on the other physical case, but, initially, developing a new and more efficient aerofoil's shape which is afterwards going to be 'filled' with material in the structural study. Then, as the outer geometry has already been optimised for the case study, its inner material layout is also going to be modified so as to optimise even more the definition of the aerofoil.

Finally, the optimal aerodynamic results joined with the inner, more efficient, structural layout will be analysed, filtering the positive output gained from the study, and proposing new future milestones for the community.

1.1 Topic Overview

When referring to aeronautics, different uses of the optimisation procedure have been given by the community the last 60 years [6], but not only in the aeronautical field, but also the automotive [7], civil structures [8] or even medical devices [9]. A key parameter is the aerodynamic behaviour of the design, thus its variables as well, such as the drag, lift and pitching moment. Therefore, the optimisation procedure has reached this field of study and numerous investigations have been deployed by the engineers and scientists. Initial discoveries where found while studying the aerofoil (and/or the wing) of an aircraft for specific flow conditions [10], but nowadays the methodology has expanded towards other parts of the aircraft such as the position of the engine's nacelle [11].

From this point, where the target of optimisation is fixed, the mathematics behind the diverse procedures need to be described as specific techniques are more suitable for different cases. For instance, three main methodologies arise. The simplest from the implementation point of view is the *finite difference method*, but for heavy loaded simulations, the procedure results to be inefficient because of what the computational cost implies. Behind this last statement is found the *gradient-based* methodology which, in order to avoid those computational limitations, uses a different perspective of the problem. The other technique, the *gradient-free* method, faces a negative characteristic of the gradient-based procedures for certain cases. For studies where there is a baseline design which provides a continuous geometry, it is feasible to provide the gradient (derivative) of the objective function related to the independent variables so as to, afterwards, apply deformations to the initial shape. But, for the latter technique, the user can avoid using polynomials or splines and carry a general-purpose (domain independent) search for a local optimal and, afterwards, by mimicking the genetic algorithms which use mutations and crossovers, a global optimal is obtained [12] [13] by studying the memory distribution in the computer for the 'parents' and applying the modifications. In this thesis, the gradient-based technique is going to be employed as the used software provides the capabilities to obtain an optimal redistribution of an initial design, while the gradient-free procedure lies out from the scope of the thesis.

Hereafter, the gradient-based algorithm analyses a fluid domain variable (solution) in terms of independent parameters. For instance, if an optimisation of the lift-to-drag ratio is intended, this is going to be defined as the state variable, while the sensitivities are going to be given by the design variables which, as an example, can be different locations of the aerofoil. From this point, the adjoint solution is obtained by applying the mathematics behind the procedure. This technique provides afterwards the local optimal which follows the gradient direction or, in other words, where to move the design parameters to improve the previous state, while the distance to travel is provided by an one-dimensional search in the line for a acceptable modification, until the optimal is reached [14].

Then, specific methods are created for certain tasks and, for flow conditions, the adjoint method is a reliable candidate [15] [16]. This method gathers the idea behind the gradient-based theory and specifically adapts towards the studied situation. One way to move towards the gradient-based technique is by using the adjoint solution, which starts from a flow solution state where an objective function is obtained *e.g.* lift or drag. By using the definition of the independent variables, which tend to be the variation of the position of certain control points distributed and embedded inside the mesh, the gradient is obtained.

Nevertheless, inside the gradient-based adjoint methodology, two different techniques can be applied. Both of them require from the gradients calculation, but their collecting is different. From a first approach, the studied geometry can be understood to be the independent variable of the setup, meaning that the system of equations must be solved by including the residual function (in terms of the control points) inside the definition of the equations and, afterwards, solve the linear system. This is what is called the Continuous Adjoint Method (CAM). It has been demonstrated [17] that, for a numerous number of design variables, it is not efficient. This reason induced the application of a new technique, the Discrete Adjoint Methodology (DAM) which, instead of defining the residual or cost function along the boundary, the discretisation of the flow variables is applied directly to the field equations. In that case, the direct numerical inversion is avoided, which may be adequate for costly computational processes involving substantial number of design variables.

For instance, the work done by *Alfonso Bueno-Orovio et al.* in [18] describes the methodology and numerical implementation of the CAM into the Spalart-Allmaras turbulence model for the same case study of this thesis, the RAE 2822 aerofoil, and a whole wing model, the ONERA-M6. In this study, the fluid equations in the adjoint process are treated as a set of Partial Differential Equations (PDE) meaning that the control function is the geometry shape itself. Examples of the DAM can be found in the work done by *Marian Nemec* and *Michael J. Aftosmis* in [19] where a NACA 0012 profile is lift-constrained and drag minimised, complemented with another test regarding the optimisation of the lift-to-drag ratio for a model of the Apollo reentry capsule.

As seen previously in all the methodologies described, there are different paths to reach a specific goal. Then, the definition of this control points also might be described using different procedures. On one hand, there are the parametrisation techniques, involving a continuous line defined by a set of weighted points and, on the other hand, the Free-Form Deformation (FFD) technique which embeds a specific shape to optimise inside a box or a cube, depending on the volumetrical character of the study, by means of a set of boundary nodes. Both of them apply the sensitivity analysis in all of the defined new nodes and, afterwards, its correspondent modification which is going to lead the reshape of the geometry by means of, again, parametrisation techniques. The main difference between both methodologies is that using a FFD, the user has a wider range of possibilities as it is not constrained by the weighting factors of the nodes defining the aerofoil's shape [20].

The study done by *Sam Teherkhani et al.* in [7] provides an example of an aerodynamic design of the light bar of a police car using the Bézier curves as a parametrisation technique while, for the latter, *Olivier Amoignon et al.* in [21] uses the FFD method to minimise the produced drag at a constant lift state of a transonic swept wing.

Structural optimisation sets as a target the maximisation of the material resources to fulfill a defined constraint. In [22] three main categories of optimisation are defined. The first of them, and probably the more general perspective of the problem, is the shape's design which has to be adapted to the needs of the environment. Certain geometries may have better performances by just this 'visual' focus. Following, there is the size of the component. It refers to not only satisfying the initial constraints, but optimising as well the amount of resources involved. Finally, once the general product is obtained and sized, a more accurate output can be extracted by analysing its inner layout, trying to reduce the amount of material while redistributing the loads to other regions of the layout while being inside the safety behaviour. By doing so, an fully-functional and optimal design would be obtained reducing the cost and the material involved.

To do so, a few recent techniques appeared in the state of the art. The first investigation was done by *Bendsøe* [23] in 1989 where he first applied the density-based approach for a solid isotropic material in different setups. Actually, one of the most common and used techniques is the stated previously, which is called *Solid Isotropic Material with Penalisation* (SIMP). Following, there is the *Evolutionary Structural Optimisation (ESO)*, developed by *O. Querin*, *Y.M. Xie* and *G.P. Steven* [24] in 1993. The foundations of both techniques are quite the same. One parameter of the study is set to be optimised (*e.g.* Young modulus) and a density variable is generated. The latter provides information about the material state of the finite element inside the geometry boundary, being null when its void and one when filled. From this point, the optimisation is developed by a sensitivity analysis as it was stated before. This one gives the solver the information regarding the weight the element has in the optimisation process and then, in terms of the previous result, the layout is modified by means of the general volume constraint.

Regarding the *SIMP* methodology, the sensitivity analysis adds a penalisation factor to the element material density which has a secondary impact on the design variable sensitivity as it regulates their structural weight in the layout, thus the amount of removed material. *Pedro Gomes* and *Rafael Palacios* [25] from *Imperial College London* applied this technique into a fully-coupled aerodynamic and stiffness-based topology optimisation of a compliant aerofoil thus introducing the fluid-structure interaction science. They as well describe two different strategies, the first one using a more aerodynamic profile as an initial state followed by the inverse procedure, where, initially, the inner layout is optimised. The same technique may be applied but using a different perspective as starting point, as it can be seen in the job done by *Gabrielle Capasso et al.* in [26], where, instead of using a global parameter as the stiffness is, they focus on local quantities, which in this case is the stress magnitude. The path to be followed then depends on the input parameter the topology optimisation receives.

The *ESO* technique applies a gradual removal rate of inefficient material when reaching a global optimum. Therefore, a removal rate is set by the user and the less efficient elements are suppressed and, afterwards, a new structural analysis recalculates the parameters for the new layout. The work done by *Liang Xia et al.* in [27] apart from applying the *ESO* method to a wide variety of tests, they also reformulate the problem by adding a bidirectional character to the evolution, meaning that not only the material can be removed but added. The reason behind this is that, after an iteration is carried out and a certain amount of elements are deleted, it is not possible to regenerate the structure thus missing probably more efficient designs including the previously suppressed layout. After this modification of the technique's main idea, other scientists have as well tried the new formulation such as in [24] and [28].

Research has been done and new innovations, in terms of the topological and aerodynamic studies, are starting to be implemented in the aeronautical industry. A general perspective of the actual procedures and applications is gathered in the work done by *Ji-Hong Zhu et al.* in [29], were, for instance, the topological optimisations of an aircraft engine's pylon, an aircraft fuselage and the support for a 4-satellite component are provided among others procedures. Following a more detailed point of view, in terms of the topological optimisation in the aeronautical field, *Airbus* with *Altair Engineering* provide in [30] the application of this methodology to the design of the wing ribs, then it should be highlighted that the described optimisation is already expanding towards the actual components setup. Moreover, an aerodynamic optimisation is coupled in the analysis to an aeroelastic-born case in the study made by *K. Maute et al.* [31] where, apart from dealing with a mixing of sensitivities between fluid-induced structural loads, the material behaviour is considered to behave inside the non-linear response, thus forcing the analysis to use a coupled strategy between optimisations and, consequently, a higher-degree of difficulty is involved.

1.2 Motivation and Goals

In terms of the fluid dynamics simulations, the actual state of the art of commercial and open-source software show high-fidelity and powerful tools to provide realistic and useful data, in which the physics behind the phenomena are showcased along the CFD study. Then, from this point where practically the biggest improvements are reached from the computational procedures and techniques, new ideas should arise in order to bring new glows of development in this field.

This is why, while waiting for the whole scientist community to bring this jump in improvement, the aeronautical sector has had to restructure itself so as to provide small steps of development for the actual state of its science. Therefore, the aerodynamic shape optimisation is one of the bridges built to bring a knowledge expansion until more efficient and powerful computational research is implemented in the society.

The aim of the thesis is then, the use of this quite recent methodology to improve a bi-dimensional aerodynamic shape, specifically the *RAE 2822* aerofoil, for certain transonic flow conditions with different goals i.e. lift-to-drag ratio maximisation and drag minimisation at a constant lift constraint, and a geometrical constraint, defining the wing-box. Then, a more developed and improved geometry is created by using the open-source software resources.

Nevertheless, the thesis takes one step forward and couples the aerodynamic efficiency output with the material and structural layout improvement aiming to achieve the highest stiffness-to-weight ratio, leading towards an optimal use of the involved material resources, the improvement of air-navigation procedures and the impact it has as well in the aerodynamics study, as the material optimisation is directly linked with the energy management of the vehicle.

1.3 Thesis Outline

The fluid dynamics and structural theoretical basis, where the computational approaches emerge from, are described in *Chapter 2*, followed in *Chapter 3* by the CFD software used, its methods and the validation of the extracted results. Then, in *Chapter 4* and by following an analog scheme as in the previous chapter, the structural mesh verification and the *BESO* principles which will lead the investigations are presented. In *Chapter 5*, the aerodynamic results are unveiled and analysed and the first optimisation is carried out. Next section is *Chapter 6*, where the structural results are plotted and, finally, the coupling between both optimisation methodologies is shown in *Chapter 7*. Once the thesis' goals are reached, in *Chapter 8*, the conclusions are described while including the future work of the subject.

Chapter 2

Theoretical notes

2.1 Aerodynamics

In this chapter of the thesis, the physics behind the case study are described and, afterwards, the computational implementation is commented. For the first feature, the flow's behaviour is modelled by an approximate methodology, the so called *Reynolds Averaged Navier-Stokes* (RANS) equations, specifically using the turbulent model provided by *Spalart* and *Allmaras* [32], because of its simplicity and accuracy. For the latter, the approach will drive towards not the general theory behind its implementation, but the one used in the *SU2* software, as it provides a general optimisation framework in its design. Then, the computational fluid dynamics weight of the thesis is going to lean on their methodologies due to the coupling's simplicity of the required techniques.

After the initial conditions results are obtained, the idea behind this field of study in the thesis lies in the optimisation of the first setup so as to reach a specific goal or target. Therefore, in this section, the set of techniques involved in that procedure are also included.

2.1.1 Reynolds Averaged Navier-Stokes equations

Following the comments made above, RANS equations were deemed to be adequate for the report's purposes, but before immersing ourselves in the simulation parameters of *SU2* (section 3.3), a brief introductory theoretical description of the case study is presented, aiming at the full understanding of the physics and further selected simulation features. Thereafter, the general fluid equations for the flow's continuity and momentum conservation are presented, which are the well-known *Navier-Stokes* equations [33]:

$$\frac{\partial \rho}{\partial t} + \nabla \cdot (\rho \mathbf{u}) = 0 \tag{2.1}$$

$$\frac{\partial \rho \mathbf{u}}{\partial t} + \mathbf{u} \cdot \nabla (\rho \mathbf{u}) = -\nabla p + \mu \nabla^2 \mathbf{u} + \rho \mathbf{b} \tag{2.2}$$

being ρ the fluid density, μ the dynamic viscosity, p the pressure, $\boldsymbol{u} = (u_x, u_y, u_z)$ the fluid velocity and $\boldsymbol{b}$ a body force. From this point, the RANS equations must be found and furthermore described. For clarity purposes, the notation is changed to index notation.

$$\frac{\partial u_i}{\partial x_i} = 0 \tag{2.3}$$

$$\frac{\partial u_i}{\partial t} + u_j \frac{\partial u_i}{\partial x_j} = -\frac{1}{\rho}\frac{\partial p}{\partial x_i} + \frac{\partial}{\partial x_j}\left(\frac{\mu}{\rho}\frac{u_i}{x_j}\right) \tag{2.4}$$

Following the theoretical notes provided by the *University of Stanford* [34], the *Reynolds-averaged* quantities are defined, in which U_i is the mean time-averaged velocity and *u'* is the fluctuating component:

$$u_i(x_k, t) = U_i(x_k) + u'(x_k, t) \tag{2.5}$$

$$U_i(x_k) = \lim_{T\to\infty} \frac{1}{T}\int_0^T u(x_k, t)\, dt \tag{2.6}$$

Knowing that, for time-averaged approach the unsteady term from equation (2.4) disappears and applying equations (2.5) and (2.6) to it, the general equations for a time-averaged approach are obtained, noting that the term $\overline{u_i' u_j}$ is the Reynolds stress tensor, which account for the total stress tensor in the turbulent fluctuations for the RANS equations:

$$\frac{\partial U_i}{\partial x_i} = 0 \tag{2.7}$$

$$U_j \frac{\partial U_i}{\partial x_j} = -\frac{1}{\rho}\frac{\partial p}{\partial x_i} + \frac{\partial}{\partial x_j}\left(\frac{\mu}{\rho}\frac{U_i}{x_j}\right) + \frac{\partial\left(-\overline{u_i' u_j}\right)}{\partial x_j} \tag{2.8}$$

One way to relate the Reynolds stress tensor with the known averaged quantities is by using the *Boussinesq* relationship, which, in a simply way, relates the tensor with the velocity gradients using what is known as the *eddy dynamic viscosity* μ_τ (in *Spalart-Allmaras* [32] nomenclature, it is used the kinematic viscosity ($\nu_\tau = \mu_\tau/\rho$)), being it an scalar value. It is necessary to point out that there are other ways to approach the translation of the tensor, such as the Reynolds Stress Transport models, but for simplicity and effectiveness, the *Boussinesq* model is applied:

$$-\overline{u_i' u_j} = 2\frac{\mu_\tau}{\rho} S_{ij} = 2\frac{\mu_\tau}{\rho}\cdot\frac{1}{2}\left(\frac{\partial U_i}{\partial x_j} + \frac{\partial U_j}{\partial x_i}\right) = \frac{\mu_\tau}{\rho}\cdot\left(\frac{\partial U_i}{\partial x_j} + \frac{\partial U_j}{\partial x_i}\right) \tag{2.9}$$

2.1.2 Spalart-Allmaras turbulence model

From this point, different authors have proposed a set of strategies capable of solving the transport equations. The most known models are the *Spalart-Allmaras* (SA) (1eq) [32], $\kappa-\epsilon$ (2eq) [34], $\kappa-\omega$ (2eq) [34] or the *Baldwin-Barth* (1eq) [35]. In this work, SA is chosen. This one has been especially developed for aerodynamic purposes and mixes the viscous sublayer information, with the logarithmic formulation as a function of the y^+ value.

$$U_j \frac{\partial U_i}{\partial x_j} = -\frac{\partial}{\partial x_i}\left(\frac{p}{\rho}\right) + \frac{\partial}{\partial x_j}\left(\frac{\mu}{\rho}\frac{U_i}{x_j}\right) + \frac{\partial}{\partial x_j}\left(\frac{(\mu+\mu_\tau)}{\rho}\frac{\partial U_i}{\partial x_j}\right) \tag{2.10}$$

For this new approach, new nomenclature is used. For instance, the turbulent Prandtl number σ, empirical constants in the turbulent model, *e.g.* $\mathbf{c_{b1}}$, and the measure of the deformation factor $\boldsymbol{S}$. If equation (2.9) is recalled, and the eddy's viscosity ν_τ is the central variable, it is possible to obtain a transport equation by an empirical way if the total or material derivative is applied to the parameter and then, it is equaled to a production term and a diffusion one:

$$\frac{D\nu_\tau}{Dt} = \frac{\partial \nu_\tau}{\partial t} + U_i \frac{\partial \nu_\tau}{\partial x_i} \tag{2.11}$$

As ν_τ is a scalar term, the deformation tensor $\frac{\partial U_i}{\partial x_i}$ must be a scalar value as well. This deformation tensor is also known by the variable S_{ij}. From this point, the production (of eddies) term is defined via the vorticity Ω_{ij} and, for the diffusion phenomena, it can be described by the gradient:

$$S_{ij} = \sqrt{2\Omega_{ij}\Omega_{ij}} \tag{2.12}$$

$$\Omega_{ij} = \left(\frac{\partial U_i}{\partial x_j} + \frac{\partial U_j}{\partial x_i}\right) \tag{2.13}$$

$$\text{Diffusion} \longrightarrow \nabla\cdot\left(\frac{\nu_\tau}{\sigma}\nabla\nu_\tau\right) \tag{2.14}$$

As it is not stated that the integral of ν_τ along the boundaries should be conserved, a non-conservative parameter is added. Something similar happens with the two-equation models, which end up having this kind of relation. Therefore, by this analogy, SA [32] reformulated the diffusion term (2.14) in order to obtain the new transport equation:

$$\frac{D\nu_\tau}{Dt} = c_{b1} S \nu_\tau + \frac{1}{\sigma}\left[\nabla\cdot(\nu_\tau\nabla\nu_\tau) + c_{b2}(\nabla\nu_\tau)^2\right] \tag{2.15}$$

Near the wall region and for high Reynolds numbers, SA could demonstrate by a dimensional analysis that the starting point of the eddies' destruction started at a specific distance from the wall combined by other parameters described as $-c_{w1}(\nu_\tau/d)^2$, where d is the distance to the wall and c_{w1}, an empirical constant related to the destruction term near the wall. When the distance is much higher than the shear layer, this term vanishes thus representing the non-influenced behaviour of the flow.

It is stated in [32], that the previous equation shows accurate results in the logarithmic layer[1] but it shows a weak skin friction coefficient in the outer part of the layer then, the free flow. To correct it, the dimensionless multiplier f_w is defined, and it refers to an experimental calibrator for the destruction term in the outer region of the boundary layer, being null at the free flow regime and 1 in the log-layer. A second term is added but, in this case, for the production phenomena, the c_{b2}. The resulting equation is:

$$\frac{D\nu_\tau}{Dt} = c_{b1} S \nu_\tau + \frac{1}{\sigma}\left[\nabla \cdot (\nu_\tau \nabla \nu_\tau) + c_{b2} (\nabla \nu_\tau)^2\right] - c_{w1} f_w \left[\frac{\nu_\tau}{d}\right]^2 \tag{2.16}$$

where the graphical representation is depicted in Figure (2.1):

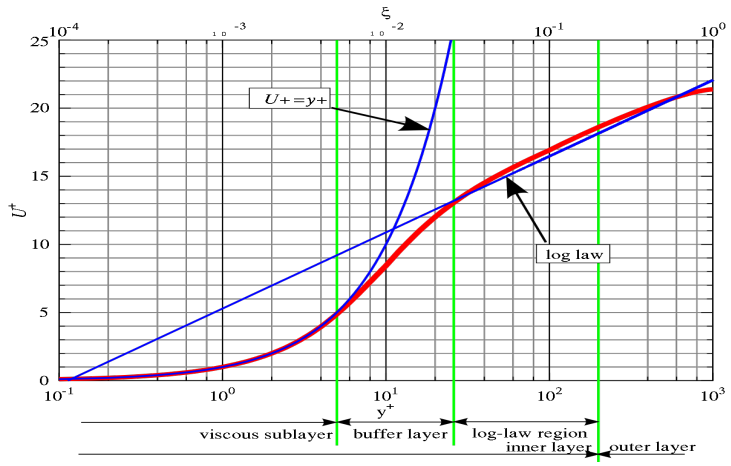

Figure 2.1: Law of the wall representation. Extracted from [36].

The left-hand side of the equation represents the transport model for the eddy viscosity and must equal to the production term, followed by the diffusion one and ending with the destruction term, respectively. As well as other coefficients present in equation (2.16), it can be described by the next set of parameters where: g is a limiter effect calibrator; c_{w3} a skin friction calibrator; r is a control function calibrator; l is the mixing length; u_τ is the friction velocity; c_{w2} is a slope limiter for the destruction term; and κ is the Kárman constant.

$$f_w = g\left[\frac{1 + c_{w3}^6}{g^6 + c_{w3}^6}\right]^{1/6} \tag{2.17}$$

$$g = r + c_{w2}\left(r^6 - r\right) \tag{2.18}$$

$$c_{w1} = c_{b1}/k^2 + (1 + c_{b2})/\sigma \tag{2.19}$$

$$l \equiv \sqrt{\nu_\tau / S} \tag{2.20}$$

$$S = u_\tau / (kd) \tag{2.21}$$

$$\nu_\tau = u_\tau k d \tag{2.22}$$

$$r \equiv \frac{\nu_\tau}{S k^2 d^2} \tag{2.23}$$

[1] (also known as "*law of the wall*") (Figure (2.1)). The velocity of a point inside the boundary layer for a turbulent flow follows a proportional relationship with the logarithmic value of the distance between the stated point and the closest point in the wall [36].

Near-wall treatment

All the previous development has not considered the viscous sublayer neither the buffer zone[2]. It is known that the eddy viscosity in the log-layer can be defined as $\nu_\tau = \kappa y u_\tau$ [32], being y the height. In order to extend it to the wall, a new parameter is generated, $\tilde{\nu}$, which basically describes a linear behaviour of the transport quantity until the wall boundary. This last parameter equals ν_τ except in the viscous sub-layer. An intermediate variable, χ, that represents the ratio between these two transport quantities, $\chi = \tilde{\nu}/\nu$, it is used.

Following the statement made in *Mellor* and *Herring* [38] regarding the behaviour of the previous ratio from the wall to the log-layer, χ is defined as $\chi = \kappa y^+$ and knowing from [32] that $\nu_\tau = \kappa y u_\tau$, two new coefficients allow us to represent the near wall behaviour, being f_{v1} and c_{v1}, log-layer calibrators:

$$\nu_\tau = \tilde{\nu} f_{v1} \tag{2.24}$$

$$f_{v1} = \frac{\chi^3}{\chi^3 c_{v1}^3} \tag{2.25}$$

Moreover, the production term needs also to be adapted by introducing a production calibrator in the log-layer, f_{v2}:

$$\tilde{S} \cong S + \frac{\tilde{\nu}}{\kappa^2 d^2} f_{v2} \tag{2.26}$$

$$f_{v2} = 1 - \frac{\chi}{1 + \chi f_{v1}} \tag{2.27}$$

That previous definition allows the production term to follow the log-layer behaviour all the way to the wall ($\tilde{S} = u_\tau/(\kappa y)$). Analysing then the previous statements, one can check the $\tilde{\nu}$ is null in the ground as $\tilde{S}$ is singular, therefore, the logarithmic formulation couples all along the layer. Bounding together the last definitions with equation (2.16), the general one-equation turbulence model from Spalart-Allmaras is given by:

$$\frac{D\tilde{\nu}}{Dt} = c_{b1}\tilde{S}\tilde{\nu} + \frac{1}{\sigma}\left[\nabla\cdot((\tilde{\nu}+\nu)\nabla\tilde{\nu}) + c_{b2}(\nabla\tilde{\nu})^2\right] - c_{w1} f_w \left[\frac{\tilde{\nu}}{d}\right]^2 \tag{2.28}$$

[2] Space found between the viscous sub-layer description and the logarithmic one, where neither laws describe the phenomena. It is usually found between $y^+ = 5$ and $y^+ = 30$ [37]

Laminar region and trip term

If more accuracy is desired, the user can still implement the discerning between a separated shear layer and the recirculation region after the creation of the boundary layer and bound them together when inevitable via two trips, one that separates and the other which destroys the boundary between both, as it can be seen in Figure (2.2).

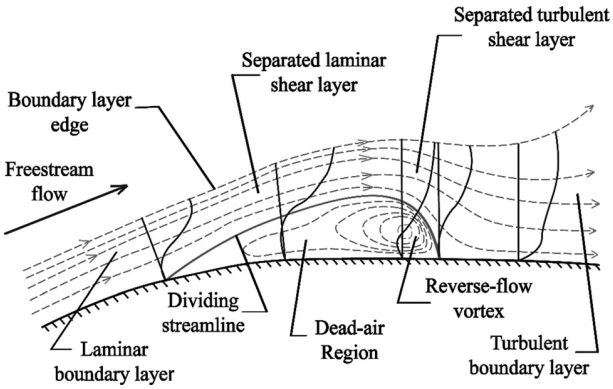

Figure 2.2: Schematic of a laminar-separation bubble. Extracted from [39]

It is necessary to point out that the first term regarding the layers has a turbulent behaviour. The final and general formulation is given in equation (2.29). For further details, check [32].

$$\frac{\partial \tilde{\nu}}{\partial t} + u_j \frac{\partial \tilde{\nu}}{\partial x_j} = c_{b1}\left(1 - f_{v2}\right)\tilde{S}\tilde{\nu} + \frac{1}{\sigma}\left[\frac{\partial}{\partial x_j}\left((\tilde{\nu}+\nu)\frac{\partial \tilde{\nu}}{\partial x_j}\right) + c_{b2}\frac{\partial \tilde{\nu}}{\partial x_j}\frac{\partial \tilde{\nu}}{\partial x_j}\right] - \left[c_{w1} f_w - \frac{c_{b1}}{\kappa^2} f_{v2}\right]\left(\frac{\tilde{\nu}}{d}\right)^2 \tag{2.29}$$

The computational implementation in *SU2* for the Spalart-Allmaras equation follows the model presented in *Turbulence Modeling Resource* [40] of the Langley Research Center from NASA which is the one described before in equation (2.29).

2.1.3 Sensitivity analysis

One of the thesis' targets is to be able to find an optimal geometry for an aerofoil in specific flow conditions. From now on, in this theoretical chapter where the fluid behaviour has been described already, the focus is turned to the optimisation procedure.

For instance, in each of the volumes cells of the domain there is a certain number of variables that shape the final result of the setup. Design variables affect the established objective function and constraints, thus knowing how design variables affect the objective function and constraints, it can be used as a feature where useful information can be extracted.

This information is required in gradient-based algorithms, which for heavy computational simulations such as CFD is normally preferable to gradient-free algorithms such as genetic algorithms, as the one

used in the study by *M. Lohry et al.* [13]. By performing small perturbations to each design variable, it is possible to evaluate sensitives that these have on the objective function and constraints. This process can be carried out using the finite differences method, which is the most common procedure for sensitivity analysis. However, for large problem such as those involving high fidelity CFD analyses, the application of the finite differences method might become expensive from the computational point of view.

To improve the numerical efficiency of the optimisation, adjoint methods are now becoming more common, where sensitivities are already coded in the analysis solver [41]. Specifically for aerodynamics, it is common to use the *gradient-based* functions as a tool to produce the *sensitivity* model. This procedure can deal with a large number of input variables to work with and the required computational cost is not really demanding, as it gives only one output as a solution. But, to begin with, a specific total variable must be selected for the study, the objective function L, for instance, lift, drag or moment coefficients. As in [42], L depends on the flow variables of the study (solution) u, and the design variables (or parameters), D, which represent the modifications in the original state. Afterwards, the sensitivity formulation is defined:

$$\frac{dL}{dD} = \frac{\partial L}{\partial D} + \frac{\partial L}{\partial u}\frac{\partial u}{\partial D} \tag{2.30}$$

Sensitivity is basically the output obtained when analysing the effect that an independent parameter has on a dependant one by means of its uncertainty (in this case, the difference to an original value). In equation (2.30) turns out to be a Jacobian matrix, which expresses the variation of an input function at each differentiable point, and one sensitivity term. Consider the number of input and output variables as *Ni* and *No*, respectively:

$$\frac{\partial L}{\partial D} = \begin{bmatrix} \frac{\partial L_1}{\partial D_1} & \cdots & \frac{\partial L_1}{\partial D_{Ni}} \\ \vdots & \ddots & \vdots \\ \frac{\partial L_{No}}{\partial D_1} & \cdots & \frac{\partial L_{No}}{\partial D_{Ni}} \end{bmatrix} \tag{2.31}$$

Moreover, the flow solution must be constrained after the sensitivity analysis as it is required to converge. In other words, if any modification or disturbance is applied to the flow variables, the final variation of the residual R is null when totally converged, thus:

$$r = R\left(u((D), D\right) = 0 \tag{2.32}$$

$$\frac{dr}{dD} = \frac{\partial R}{\partial D} + \frac{\partial R}{\partial u}\frac{\partial u}{\partial D} = 0 \tag{2.33}$$

The problematic arises when trying to compute the term that involves the gradient of the variables from the actual solution (u) of the flow with respect to the design variables (D), $\partial u/\partial D$ in equation (2.30).

By imposing the residual constraint of the sensitivity, equation (2.33), and substituting by imposing the residual constraint in equation (2.30), one yields to the final formulation of the procedure, equation (2.35), presented in the works made by the authors of references [15] [42]:

$$-\frac{\partial R}{\partial D} = \frac{\partial R}{\partial u}\frac{\partial u}{\partial D} \tag{2.34}$$

$$\frac{dL}{dD} = \frac{\partial L}{\partial D} - \frac{\partial L}{\partial u}\left[\frac{\partial R}{\partial u}\right]^{-1}\frac{\partial R}{\partial D} \tag{2.35}$$

From this point, once the sensitivity formulation has been described, the adjoint method must be applied by defining the adjoint variables matrix as Ψ, such in equation (2.36):

$$\Psi = -\frac{\partial L}{\partial u}\left[\frac{\partial R}{\partial u}\right]^{-1} \tag{2.36}$$

Note that the adjoint solution is only dependant of the objective function *L* and not of the design parameters *D* and that there is an adjoint solution for each objective function that has been defined. By manipulating the latest equation, a linear system is obtained which complexity depends on the number of the design variables:

$$\left[\frac{\partial R}{\partial u}\right]^{T}\Psi = -\left[\frac{\partial L}{\partial u}\right]^{T} \tag{2.37}$$

Embedding it to the final form of the sensitivity formulation (or total derivative), the final form is:

$$\frac{dL}{dD} = \frac{\partial L}{\partial D} + \Psi^{T}\frac{\partial R}{\partial D} \tag{2.38}$$

2.1.4 Parametrisation techniques

Parametrisation is the procedure used to define a geometry with a certain quantity of independent parameters by a mathematical approach. Its appearance is due to the computational approaches followed towards the design stages of a component, specially for the implementation of curves and surfaces. The most common techniques in the aerofoil's shape modelling can be grouped into: *Bézier curves* [43], the *Non-Uniform Rational B-Splines*, also known as NURBS [44], *Hicks-Henne* [45] bump functions and the *Free-Form Deformation box* (FFD) [46].

In this work, FFD methodology is used. This technique provides better accuracy in results while using a fewer amount of design variables compared with the other presented procedures. In fact, by basing the procedure in an already existing geometry, the slight deformations applied by the technique demonstrate better convergence ratio and smoothness. The latter feature is provided by analysing the sensitivity values of the control points, which is beneficial in terms of costs and effectiveness [20].

Free-Form Deformation box

The Free-Form Deformation technique was developed by *Sederberg* in [46] to model solids and it has its recognition because of its versatility and that, oppose to other parametrisation techniques, it does not manipulate directly the geometry of the object but the lattice of a certain space in the domain where the object is embedded. For two-dimensional cases, the box looks like a rectangle and like a cube for 3D cases. FFD can treat all kind of surfaces and has no interference with the meshes used in a diverse variety of engineering problems as the FFD also deforms it. The latest statement has attracted interest in terms of optimisation design features as just one grid is needed to provide an optimal final design. Of course, the deformation must be controlled so as to check its accuracy and realistic representations of the physical phenomena.

The formulation deals with some vectorial and spatial embedding and deformations. If a point $\boldsymbol{X}$ with coordinates (x_1, x_2, x_3) is embedded into a new reference frame $\hat{\mathbf{s}}, \hat{\mathbf{t}}, \hat{\mathbf{u}}$, ends up being defined by equation (2.39) as shown in Figure (2.3a):

$$\mathbf{X} = X_0 + s\hat{\mathbf{s}} + t\hat{\mathbf{t}} + u\hat{\mathbf{u}} \tag{2.39}$$

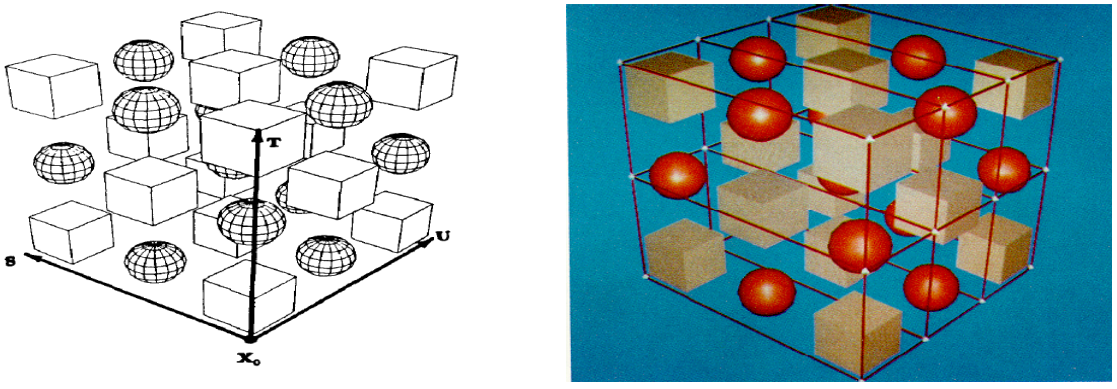

(a) s,t,u Coordinate system. Extracted from [46].

(b) FFD definition. Extracted from [46].

Figure 2.3: Free-Form Deformation Box definition.

From this point, the FFD box must be constrained and defined in the new coordinates, where the original and unperturbed control points ($P^0_{l,m,n}$) are defined with white dots along the closed box. Therefore, the control points are defined by their location in the axis: $l = 0,\ldots,L$, $m = 0,\ldots,M$ and $n = 0,\ldots,N$ such as in Figure (2.3b):

The next step is to introduce the deformation in a parameter, $\mu_{l,m,n}$, whose dimension considers the 3-axis movement, thus $3 \times (L+1) \times (M+1) \times (N+1)$. From this point, every control point is deformed by the latest parameter such as:

$$\mathbf{P}_{l,m,n} = \mathbf{P}^0_{l,m,n} + \mu_{\mathbf{l,m,n}} \tag{2.40}$$

Then, the new parametric map is constructed with 1D Bernstein basis polynomials following the definition of Figure (2.3a) [47].

$$b_l^L(s) = \binom{L}{l}(1-s)^{(L-l)}s^l \tag{2.41}$$

$$b_m^M(t) = \binom{M}{m}(1-t)^{(M-m)}t^m \tag{2.42}$$

$$b_n^N(u) = \binom{N}{n}(1-u)^{(N-n)}u^n \tag{2.43}$$

therefore, the final parametrisation is defined as,

$$\mathbf{X}_{ffd} = \sum_{l=0}^{L}\sum_{m=0}^{M}\sum_{n=0}^{N} b_{l,m,n}^{L,M,N}(s,t,u)P_{l,m,n}\left(\mu_{l,m,n}\right) \tag{2.44}$$

Once the formulation has been described, the properties of the box only influence the inner objects, thus the Bernstein polynomials and, as a matter of fact, all the piecewise segments joined to describe the geometry keep being constrained to remain continuous and smooth. Another aspect to consider, specially in this project, is that FFD allows the user to provide individual local displacement to specific nodes while keeping the box structure together.

Koshakji et al in [48] describe the theory behind the formulation made by *Sederberg* [46] in the 80's and they add as well a variety of examples in which an optimisation to its shape has been carried out. For a similar path as the one followed in this thesis regarding the aerodynamic shape optimisation, *Duvigneau* [49] expresses, step-by-step, which is the theory behind the chain of algorithms that should be applied in order to optimise a geometry and, at the end of his document, he also applies the described knowledge into research cases so as to provide specific results for certain cases of study.

2.1.5 Mesh deformation

For problems in which certain components of it are movable, such as aero-elastic phenomena or rotatory parts, the mesh has to be modified so as to follow the events and its respective information. It is then highly important to control the deformation of the grid nodes, keeping the solving procedure robust and efficient, apart from being able to embed all the required physical features. In the optimisation procedure, there will be also modifications in the mesh as the control points are subjected to the sensitivity analysis, but it requires a "translation" from the adjoint solution towards the respective displacements of the nodes.

The *SU2* environment provides a general coupling of the whole optimisation procedure, which includes the CFD simulation, the gradient-based adjoint method and the following geometry modification that also includes a mesh rearranging. Then, this software uses what is known to be the *spring* mesh deformation

procedure, which, recalling [50], considers each of the edges of the cell as a spring that follows the linear behaviour of Hooke's law for the node's displacement. Then, the equilibrium length is considered to be equal to the original edge's length and the stiffness of the spring, $k_{ij} = 1$, between nodes *i* and *j*. If the force applied is defined along with the spring's stiffness:

$$\vec{F}_i = \sum_{j=1}^{v_i} k_{ij}(\vec{q}_j - \vec{q}_i) \tag{2.45}$$

$$k_{ij} = \frac{1}{\sqrt{(\vec{x}_j - \vec{x}_i)\cdot(\vec{x}_j - \vec{x}_i)}} \tag{2.46}$$

where $\vec{q}_i$ and $\vec{q}_j$ refer, respectively, to the displacements of the spring in node *i* and *j*, F_i is the force applied at node *i* and v_i is the number of nodes which assembly an edge with the studied one (*i.e.* node *i*). Then, the force equilibrium is applied at each node so as to find the new displacement of node *i* by an iterative procedure:

$$\vec{q}_i^{k+1} = \frac{\sum_{j=1}^{v_i} k_{ij}\vec{q}_{ij}^{k}}{\sum_{j=1}^{v_i} k_{ij}} \tag{2.47}$$

so when the displacement is obtained, the new position can be extracted by:

$$\vec{x}_i^{k+1} = \vec{x}_i^{k} + \vec{q}_i^{k+1} \tag{2.48}$$

To understand how it works, at a specific time *t*, there is an existing configuration for the boundary, *B*, and the distribution of stresses. At the following time-step, the boundary *B* has moved to *B'* following the physics of the setup. In [51], one of the precursors for the mesh deformation algorithms, the authors recommended to provide a control in the produced deformations by following 3 steps. The first, considers constraining a positive value of its volume, while the second is based on treating the new mesh so as to eliminate extremely deformed cells and its respective nodes. Finally, the number of nodes should be again compatible with the initial discretisation; therefore, the mesh should be enriched to recover the suppression of the previous cells.

The first topic to deal with is the mesh movement. For instance, after applying the adjoint solver, small perturbations have been applied to the geometry of the model and, by imposing the equilibrium of forces and the spring methodology [41], the new node positions for the deformed case are available, thus, by applying the spring-analogy equations (2.45) with (2.47) at the original grid points, the deformed mesh is obtained.

The stated deformations are saved in spaces of memory called shape matrices *M*, related between them by this linear equation: $M_2 = AM_1$, where *A* is the deformation matrix. To control the volume constraint, the deformation matrix can be expressed by a pure rotation matrix (unitary), *U*, and a parameter which controls the cell distorsion, also expressed in a matrix way, which is *P*. Therefore, $A = PU$

The eigenvalues of *P* represent the modes of distorsion of the cell so, if the eigenvalue is larger than one, the cell is stretching, while if it is smaller, it is compressing. Then, if the distorsion is too drastic, the eigenvalue tend to be null. Therefore, any following deformation will create negative volumes. To avoid this, weighting coefficients are used in order to limit the deformation. Furthermore, those eigenvalues are also used to control the mesh quality thus the second phase of the deformation study.

Once the deformation has been applied and checked by the quality parameters, the coarsening is the next topic to deal with. In that stage, the nominated cells to be eliminated are analysed and, if they should be erased, the vertices of the shortest of its edges are made coincident. Therefore, the number of nodes in the mesh decreases by one for each deleted cell, making it coarser than the original.

Finally, once the non-profitable cells are removed, there are different schemes used to refine the final mesh. In [41], the study carried by [52] is implemented, which presents an algorithm to provide a robust and accurate solver for deformations in unstructured meshes.

In Figure (2.4), the information is given by the edges instead of considering the nodes. During the CFD computation, the quality of the edges is stored so as to apply, afterwards at the mesh adaptation procedure, the modification regarding the stated quality. If the quality threshold is exceeded, a subdivision of the edge is applied. For instance, for a quadrangular mesh design, the division provided at the edge will represent a change in the cell discretisation from quadrangular to triangular. Tetrahedral examples are shown in Figure (2.4), extracted from [52].

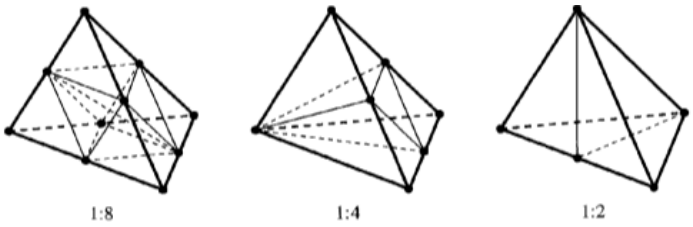

Figure 2.4: Tetrahedral subdivisions provided by the algorithm designed by *Biswas* [52].

This quality parameter uses two criteria [53]: the first is based on the results obtained by the CFD solver and the second is the number of divisions or adding nodes stated in the previous paragraph. The initial, when there is a region of the fluid domain with high gradients, it is considered that the same region has an influential error. Therefore, this error quantification can be described by the difference, in magnitude, of the velocity (Δq_i) between two continuous cells, multiplied by a length scale factor computed by the ratio between the length of the element, l_i, and a reference one, l_r. Then, considering the second factor for the new discretisation, *r* is selected: $|E_i| = \left(\frac{l_i}{l_r}\right)^{1/r} |\Delta q_i|$

2.2 Structures

The second field of study of the thesis is the computational approach towards the structural analysis of a component. Here, analyses of the stresses, displacements and force reactions are studied in order to describe and verify the behaviour of the design. During this theoretical section of the document, the hypothesis of the study plus the phenomena description is going to be presented by following the limits established in the scope of the thesis. To begin with, the ideas behind the notes that will follow below, are closely related with the methodologies used in the software *Calculix* and an open-source code for topology optimisation named as *BESO* developed by *František Löffelmann* in [28], as it is involved in this project for the structural analysis.

Regarding the science behind the case study, the aerofoil is going to be considered to behave inside the elastic region of the material, specifically inside the linear region, which implies a proportional relation between the stresses and the correspondent strains.

Since the weight parameter in aeronautics gains plenty of attention, the procedure of optimisation will drive through the best stiffness-to-weight ratio, which basically minimises the compliance of the model or, in other words, the overall flexibility. To do so, the open-source code uses the *Bi-directional Evolutionary Structural Optimisation* (*BESO*) method, developed by *Y.M. Xie* and *X. Huang* [54], a variant of the proposed work done initially by the same author and *O. M. Querin* in 1998 [24]. Hence, another consideration for the study is the isotropic distribution inside the body, which assumes an equal material behaviour in all the directions and points of a volume.

2.2.1 Elastic behaviour of the model

Ideally, in order to set the conditions for the elastic analysis, it should be considered the material conditions, defined by: the material unit vector ***M***; the Cauchy stresses σ; the displacements ***u*** and the reference stress situation, $\sigma_{\mathbf{R}}$. By forcing the behaviour to follow the elasticity rules stated above, a general definition is obtained:

$$\mathbf{f}(\sigma, \sigma_{\mathbf{R}}, \mathbf{u}, \mathbf{M}_1, \mathbf{M}_2, \mathbf{M}_3) = \mathbf{0} \tag{2.49}$$

but it is usually considered that the reference state represents the stress-free condition and that the material follows an isotropic behaviour, thus $\mathbf{M}_i = 0$. Then:

$$\mathbf{f}(\mathbf{u}) = \sigma \tag{2.50}$$

where in that case, the stress loading only depends on the deformation state.

Next step is finding the relation between the 6 independent stresses and the nine independent components of the motion, ϵ_{kl}.

$$\sigma_{ij} = C_{ijkl}\epsilon_{kl} \tag{2.51}$$

From this point, by recalling the procedure followed in [55], Hooke's law for isotropic materials should be embedded inside the elastic theory of a solid. Then, to begin with, the Cauchy stress is directly related with the deformation gradient and this latter should not be expressed dependant of the coordinates. This strain tensor must be then symmetric and is composed by a volumetric component, ϵ_M, and a distortion behaviour one, $\epsilon_{ij}^{'}$, related with the shear phenomena. If linear behaviour hypothesis are applied, a relation between the Cauchy stresses σ_{ij}, the Kronecker[3] delta, δ_{kl}, and the deformation gradient, u_{kl}, can be found. Then, the description of the strain is as follows:

$$\epsilon_{ij} = \epsilon_M \delta_{ij} + \epsilon'_{ij} \tag{2.52}$$

The volumetric deformation can be expressed by the trace of the strain tensor while the deviatoric strain tensor is obtained by using the general strain tensor and the volumetric one such as follows:

$$\epsilon_M = \frac{\epsilon_{kk}}{3} = \frac{\epsilon_{11} + \epsilon_{22} + \epsilon_{33}}{3} \tag{2.53}$$

$$\epsilon'_{ij} = \epsilon_{ij} - \frac{\epsilon_{kk}}{3}\delta_{ij} \tag{2.54}$$

then,

$$\epsilon_{ij} = \left(\frac{1}{3}\epsilon_{kk}\delta_{ij}\right) + \left(\epsilon_{ij} - \frac{1}{3}\epsilon_{kk}\delta_{ij}\right) \tag{2.55}$$

Aiming at a direct relation between the elastic modulus *E* and the strain definition, the *bulk* modulus *K* and the *shear* modulus *G* are used. The former expresses the response of a material to loads applied to the axial direction, and the latter describes the material response to cutting stresses (shear). Then, the general form of the Cauchy stress that follows the Hooke's law form is expressed [55]:

$$\sigma = \lambda tr(\epsilon)\mathbf{I} + 2\mu\epsilon \tag{2.56}$$

where ***I*** is the rank-2 identity tensor while λ and μ are the *Lamé* constants defined by:

$$\begin{aligned} \lambda &= K - \frac{2}{3}\mu \\ \mu &= G \end{aligned} \tag{2.57}$$

As Lamé constants are not given for each of the materials, equation (2.56) can be arranged by using the

[3]Mathematical function which involves two variables, *i* and *j*. Its formulation is: $\delta_{ij} = \begin{cases} 0 & \text{if } i \neq j, \\ 1 & \text{if } i = j. \end{cases}$

Young's modulus E and the *Poisson* ratio ν relation (eqs. (2.58) with the previous constants. Thus, the final expression is the one from equation (2.59):

$$\lambda = \frac{E\nu}{(1+\nu)(1-2\nu)} \qquad \mu = \frac{E}{2(1+\nu)} \tag{2.58}$$

$$\sigma = \frac{E\nu}{(1+\nu)(1-2\nu)} tr(\epsilon)\mathbf{I} + \frac{E}{(1+\nu)}\epsilon \tag{2.59}$$

2.2.2 (B)ESO methodology

The *Bi-directional Evolutionary Structural Optimisation* provided by [28], is an improved procedure from the development made by [24] in the *Evolutionary Structural Optimisation* as it does not usually suffer from mesh-dependency and divergence failures. The main difference between the procedures named above is that the former, the bi-directional, not only removes mass of the geometry, but it also can add mass. The latter technique did not consider the removed mass in the previous iteration for the following ones, thus once it is removed to a more optimised geometry, it cannot be reused again. Therefore, a possible more optimised state may be neglected.

The idea behind the ESO methodology is the material removing of less stressed areas of a certain domain, which leads to a more efficient layout of the structure. For the BESO procedure, it is possible to recover already deleted low-stressed cells, specially the ones that surround a highly-stressed demanded region. More information regarding both techniques is presented below.

Evolutionary Structural Optimisation

The first documentation provided for this method was the book written by *Xie*, *Querin* and *Steven* in the early 90's [24] as an idea to reproduce the optimisation procedure for an efficient design carried out by the environmental figures such as shells or apples.
As it was stated in the introduction of this subsection, the ESO methodology removes the low-stressed areas of a domain which it is understood to be inefficient. From this point, a doubt arises. Which should be the rate of removal or the conditions to be satisfied so as to consider the cell as inefficient? For the initial proposal a 'hard-kill' method was used, which uses a rejection ratio (c_{rr}) to mark as removable the ones below it. This rejection criteria used the von Mises stress of a cell and it was compared with a threshold, which could be a maximum or a prescribed value, thus:

$$\sigma_e^{vM} \leq c_{rr}\sigma_{max}^{vM} \tag{2.60}$$

but, as most computational procedures, a stable solution is not yet found thus an iterative process should be done.

Then, this cycle of element removal is carried out by using the same rejection ratio until a convergent state is found which, in other words tend to say that no other cells are inefficient and the remaining ones are critical for the well-behaviour of the geometry. It is also possible to provide an evolutionary rejection criteria (c_{er}) to be able to remove more mass of the object by adding it to the general one: $c_{rr}^{new} = c_{er} + c_{rr}^{old}$. Then, a new stable state is found. An example of the ESO procedure is found in Figure (2.5), where an optimal solution for a square hanging object under its own weight is provided. Note the resemblance with nature, in this case with an apple.

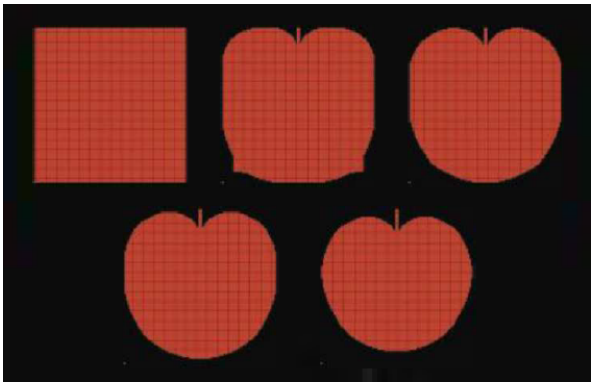

Figure 2.5: ESO solutions for an object hanging under its own weight. Extracted from [27].

Bi-directional Evolutionary Structural Optimisation

This modification of the ESO methodology intended to provide the most-optimal efficient state for a topology optimisation procedure, as the previous could lead to an efficient layout but not the best as some of the removed regions, which were not available for the solver afterwards, may have lead to a better distribution. Therefore, the ideas behind the procedure are the same, but including the mass addition problem to the equation as shown in equation (2.61).

$$\begin{cases} \sigma_e^{vM} \leq c_{rr}\sigma_{max}^{vM} \rightarrow \text{Element removal} \\ \sigma_e^{vM} \geq c_{ar}\sigma_{max}^{vM} \rightarrow \text{Element addition} \end{cases} \tag{2.61}$$

A secondary effect of this procedure is that the user can start from a certain and random layout that complies with the case's loading conditions and, from the iterative process, it can obtain the efficient model totally different from the initial one. *X. Yang* [56] shows how, for two opposite initial cases, a full filled mass domain and a slender shape, the same optimal solution is found.

The solver by itself is going to understand that the more optimal solution is the one with less mass, thus applying holes to the layout is always intended. Then, the finer the mesh, the higher the amount of holes, which may lead to a mesh instability and dependence, also know as the 'checkerboard' layout.

A. Díaz and *O. Sigmund* in [57] initially came up with this common phenomena as it appeared in the majority of the layout optimisations. This feature is characterised by a periodic distribution of void and solid cells, *i.e.* ones and zeros, representing a similar shape as the checkerboard. This is the result of a numerical instability and it must not be accepted as a solution for the optimisation.

In most cases where the checkerboard analogy applies, the final structure will not be compliant not even a solution of the problem. Then, the user can avoid it by limiting the solver's behaviour, such as the perimeter control term, which provides an extra restriction.

This feature occurs when discretising the model and applying the minimisation of the compliance constraint. It is, for instance, usual for topology optimisation problems to use 4-nodes cells. In that case, as the work uses binaries, the strain for this type of setup can result being $\epsilon_{11} = \epsilon_{22} = 1$ and $\epsilon_{12} = \epsilon_{21} = 0$ and periodic along the domain, thus the stated pattern.

To avoid the phenomena, filters are applied. *O. Sigmund* in [58] gave a formulation to modify the sensitivities $\partial f / \partial \rho$ by averaging a set of neighbouring cells:

$$\rho_i \frac{\partial f^{new}}{\partial \rho_i} = \frac{1}{\sum_{j=1}^{N} \overline{H}_j} \sum_{j=1}^{N} \overline{H}_j \rho_j \frac{\partial f}{\partial \rho_j} \tag{2.62}$$

where $\overline{H}_j$ is a weight factor and *N* is the set of elements for which the distance between centers $\Delta(i, j)$, is smaller than an specific radius r_{min}, being the studied center, *i*, and the neighbours, *j*. A visual representation for a $r_{min} = 2R$ filter radius can be seen in Figure (2.6).

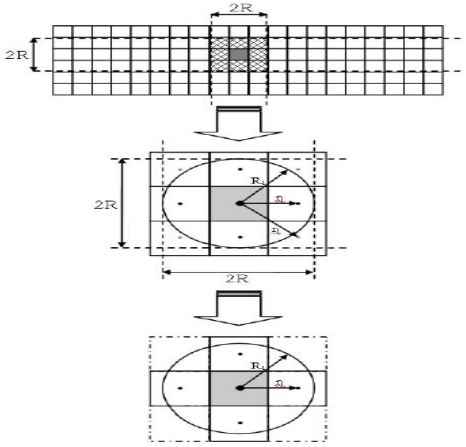

Figure 2.6: Elements participating in the filtering for element *i*. Extracted from [59]

On one hand, note that the area has been increased as well as the number of computing nodes. This interval of distances avoids to use directly the cell nodes, which gave inconsistencies, and is defined by:

$$H_j = max\big(0, r_{min} - \Delta(i, j)\big) \tag{2.63}$$

then, by applying this feature, the sensitivities inside the domain are averaged, meaning that the distribution of zeros and ones is modified towards a more balanced domain in order to be structurally sound and avoiding the checkerboard distribution. For instance, the stiffness of the void elements changes to a higher magnitude, thus a solid but weak component.

On the other hand, a second drawback of the topology optimisation procedures, apart from the checkerboard layout, is that the solution may be worse and worse at each iteration driving the process towards a divergent behaviour. It usually happens when the objective function is a material property, thus it is recommended to define the volume modification as the objective function, then an objective volume. One of the solutions for the divergence tendency, found by the same authors of [54], was to modify the obtained sensitivity values by using previous iterations values of the element studied so as to re-accommodate the tendency, thus stabilising the process. It is recommended then to use the sensitivity value of the previous iteration and average it with the actual one:

$$\alpha_e^{it} = \frac{\alpha_e^{it} + \alpha_e^{it-1}}{2} \tag{2.64}$$

The formulation of the methodology depends on the case study, which should consider which is the objective to maximise/minimise and how the algorithm is going to apply the mass modifications along the domain. Then, by finding the stiffest geometry for a given volume, one of the most common tendencies for the topology optimisation, the procedure is going to be explained.

To begin with, the strain energy of the volume is minimised, thus the compliance parameter follows. The design variables are the mesh elements, as they face their own optimisation by adding or removing mass, while the constraint is the element's volume. Gathering the last statement into an equation:

$$\begin{aligned} \text{Minimise} \quad & C = \frac{1}{2}\mathbf{f}^T\mathbf{u} = \frac{1}{2}\sum_{i=1}^{N} {u_i}^T K u_i \\ \text{Subject to} \quad & V^{Fin} - \sum_{i=1}^{N} V_i \chi_i = 0 \\ & \chi_i \in \{0,1\} \end{aligned} \tag{2.65}$$

where *C* is the mean compliance of the material and ***u*** and ***f*** are the displacement and load vectors respectively. The target value is the volume modification V^{Fin}, established by the user and dependant of each of the domain elements V_i, where *N* is the total amount of cells and χ is the binary description of the presence of mass, being 0 a void and a 1 a filled state.

When an element's mass is modified, the variation of the mean compliance or the total strain energy can be obtained. This change is also understood to be the elementary strain energy:

$$\alpha_i^e = \Delta C = \frac{1}{2}{u_i}^T K u_i \tag{2.66}$$

being α_i^e the sensitivity of the element and u_i and *K* the element displacement vector and stiffness matrix respectively.

Note that for void elements, the sensitivity is null, $\alpha_i^e = 0$, as they are not involved in the analysis and it may be where the *checkerboard* layout appear. It is then when the filter should be applied by using the nodal sensitivity of the node. This node's sensitivity is defined as an average of the elements' sensitivity surrounding it.

By recalling the general filter provided by [60] in equation (2.62), authors of the BESO method provided the adaptation for its own procedure:

$$\alpha_i = \frac{\sum_{j=1}^{M} w(r_{ij})\,\alpha_j^n}{\sum_{j=1}^{M} w(r_{ij})} \tag{2.67}$$

where *M* is the number of neighbouring nodes in the sub-domain and $w(r_{ij})$ is a linear weighing factor as a function of the distances between nodes, r_{ij}, and the minimal radium, r_{min}:

$$w(r_{ij}) = r_{min} - r_{ij} \quad where \quad j = 1, 2, \ldots, M. \tag{2.68}$$

In order to take profit of the method, the minimal r_{ij} should be higher than half of the element length. Usually, values between 1 and 3 are recommended [23].

To clarify the methodology, is always helpful to provide the general flowchart as it is presented in Figure (2.7):

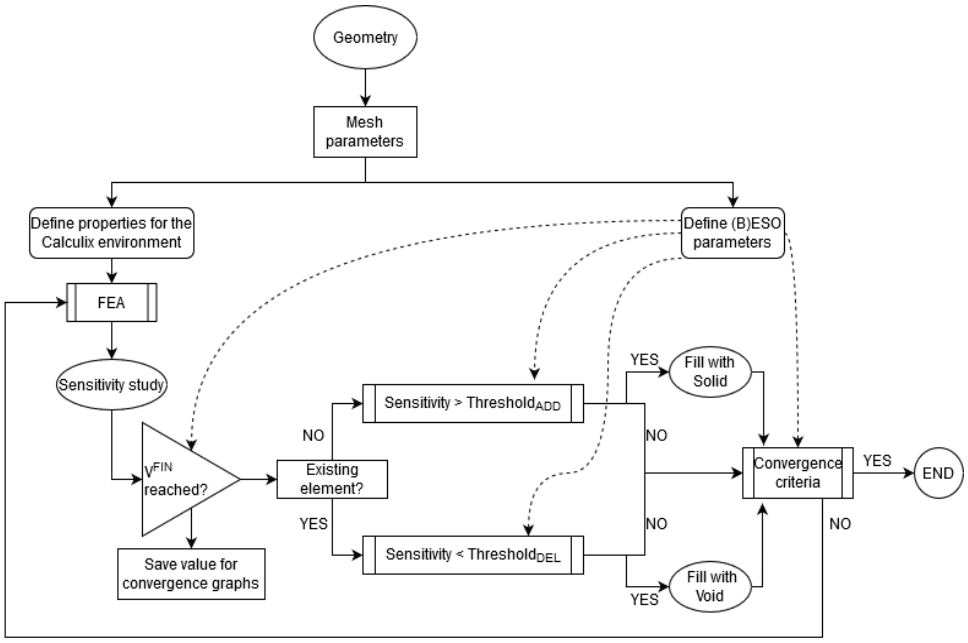

Figure 2.7: General flowchart for the BESO methodology.

Chapter 3

CFD Methodology

The initial implementation of a methodology in the thesis should be based on the fluid dynamics field, as it is the one responsible for transmitting the loads to the structure. Therefore, the initial setup is going to be described and complemented with the different developed techniques followed so as to obtain results. In that case, a geometry for the study is commented and followed by the conditions at which it is going to be subject to. Moreover, the different techniques adopted to obtain results will be described, including the software used and the set of ideas which drive the analysis to the specific goal.

3.1 Case study introduction

The goal of this part of the project is to be able to optimise the aerodynamics of any aerofoil's shape by using the software *SU2*. To start with, the simulation must be carried out with accuracy and respecting the output results from the reality, thus experimental data. Then, using a common geometry, it is recommended to compare the results with the state of the art and, therefore, the validation of the code can be reached so as to continue afterwards with the optimisation feature.

The *SU2* software suite uses the *Finite Volume Method* (FVM) [41] to solve the PDE for the RANS equations and its corresponding application towards the adjoint methodology. The FVM procedure considers the volume integrals of the fluid model as surface integrals, thus analysing the fluxes between elements. By doing so, a conservative and consistent procedure is followed. Moreover, the user can distinguish between centered and upwind schemes and explicit or implicit time integration methods, apart from the availability for the user to choose features regarding robustness and convergence tools.

The RAE 2822 aerofoil has been previously studied by influencing organizations in the world and in a wide variety of conditions, such as *NASA* and the *Imperial College London*. It has been a common topic in scientific articles regarding the computational fluid dynamics science, for instance, the studies carried out by *Roberto Palacios* and *Pedro Gomes* in [25] and the [61].

This aerofoil, showed in Figure (3.1), is designed for transonic regimes of flight, so the shockwave phenomena is intended to be withstand and, moreover, it is understood to be one of the standard testcase to study turbulent phenomena in CFD simulations.

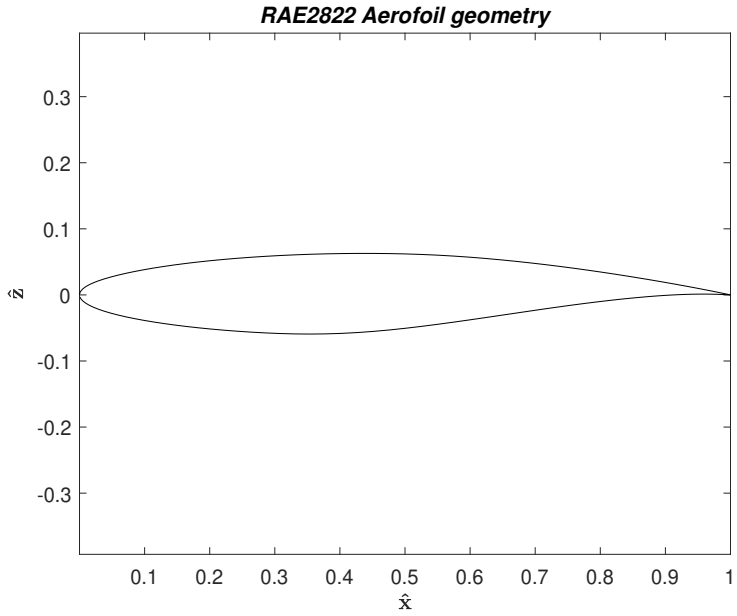

Figure 3.1: Geometry of the RAE 2822 aerofoil in dimensionless coordinates respect to the chord.

As was stated before, the selected geometry is the RAE 2822 aerofoil, designed specifically for transonic purposes where a shockwave is present, specially at the Reynolds number for which the simulation is going to be established ($Re = 6.5e^6$). This Reynolds number is selected due to the availability of experimental data to validate the obtained results. In the following table, Table 3.1, a summary of the flow conditions is presented.

Table 3.1: Case study flow conditions

Mach	**Reynolds**	**Angle of Attack**	**Temperature**	**Pressure**
0.729	$6.5 \cdot 10^6$	$2.31°$	288.15 K	101325 Pa

Once one notices the flow features, it is clear to point out that the flow for the specified Reynolds number is going to be turbulent and probably an interference between the shockwave and the boundary layer is going to appear. Therefore, aiming at simplicity and low computational costs, the RANS equations were ran by using the one-equation *Spalart-Allmaras* [32] turbulence model.

On one hand, the y^+ value must be revised so as to check the correct approach of the script written and the current computational process during the simulation. On the other hand, the post-process must be decided from the beginning as it intends to show up the stated objectives of the current study.

In this case, for the CFD approach, the lift and drag coefficients ($C_l - C_d$) together with the y^+ value must be all tracked in order to, afterwards, provide the sufficient tools to carry out the *aerodynamic shape optimisation* in section 2.1.3, using the *discrete-adjoint methodology*, and the interaction of the loads between the fluid and the structure, aiming at the topology optimisation of the inner part of the aerofoil.

3.2 Mesh generation

The first critical point in a CFD simulation, in order to obtain realistic results with the lowest computational cost, is the design of a mesh. This feature provides the solver with the physical phenomena foundations, then, a good definition and simplicity, is going to facilitate the operations and the avoidance of errors, such as the non-representation of the physics behind the study, divergence of the solution or the amount of required effort.

The software used in the study is *Gmsh* developed by *Christophe Geuzaine* and *Jean-François Remacle*, which it is an open-source tool capable to describe a geometry in 2D and 3D, and it also provides a function that, via own algorithms, generates the grid which afterwards is going to be used, for instance, by the CFD solvers. All of these features are defined by the user and therefore, the generation can be adapted to the goals of the project.

To begin with, the aerofoil's geometry data must be obtained so as to be applied inside the *geometry* module in *Gmsh*. Data can be obtained from *UIUC Airfoil database* [62], which provides a discretisation of the geometry using a cosine distribution towards the leading and trailing edges. Nevertheless, *Gmsh* cannot read the output file of the discretisation so it needs to be translated to **.geo* input format.

Once the points are read by the geometry module, using a *Spline*, a *Bézier* curve or straight lines between points, it is possible to bound the dots into a line (2D geometry). Next step relies on defining the fluid domain, which for a good development, different considerations must be kept in mind.

These considerations are: the physical domain boundary's interference; the boundary conditions; and the shape coupling with the aerofoil's geometry. The first has been demonstrated by *Spalart et al.* in [63] and gathered as a theoretical review in [64], that the size of the domain can influence the results as it can be considered as a restriction for the flow's behaviour. The next one must represent correctly the physical problem which is being studied. The latter, is directly related with the grid generation and the parameters which it works, for instance, the orthogonality of the cells, the avoidance of embedding cells with others and, the most important, the coupling with the solver's numerical scheme. Depending on the selected one, the data can come from an edge, a point or by a combination of both.

Gmsh also offers the user the capacity to decide how their meshing algorithms must aim for, for instance, the RAE 2822 aerofoil requires the tracking of the particles next to the shape's boundary and the downstream flow that comes afterwards. Moreover, as the domain is large compared with the aerofoil's size, the outer areas, less influenced by the perturbation of the element, can be defined in a coarser form, thus diminishing then the number of cells and the computational cost.

From that point, infinite ways of meshing can be selected but, the user must be able to decide the one with more optimal results. Different approaches can be used: a very dense mesh with small control volumes along domain, ensuring the fidelity of the model with the reality but increasing the computational costs; declare different sub-areas inside the domain and meshing them with the specific number of divisions aiming for good accuracy but decreasing the previous effort.

The counterpart of the latter, which is the most used one, is that it requires a verification process of the output values by analysing the mesh dependence in the results. This is why every single CFD simulation needs a validation of the used mesh. This topic is discussed forward in the document, specifically in section 3.4. Finally, in Figure (3.2), the used grid domain can be checked.

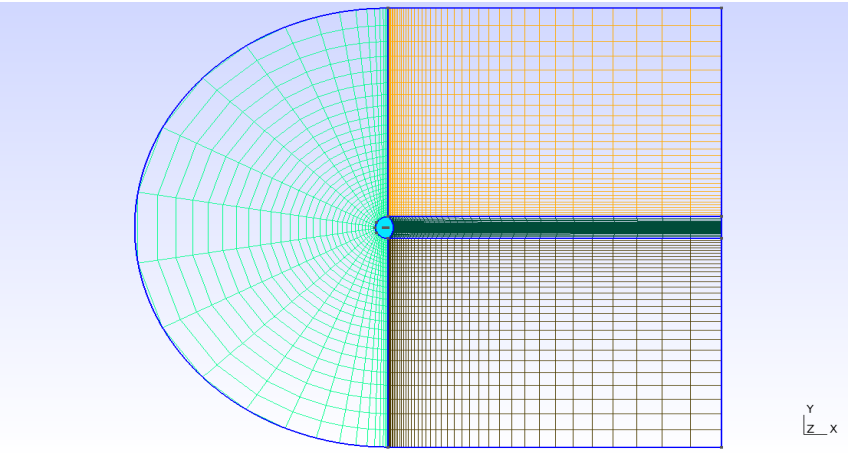

Figure 3.2: General view of the grid

For the correct discretisation of the boundary layer, a specific refinement from a triangular unstructured mesh to a quadrangular structured one has been done, as it can be seen in Figures (3.3a) and (3.3b).

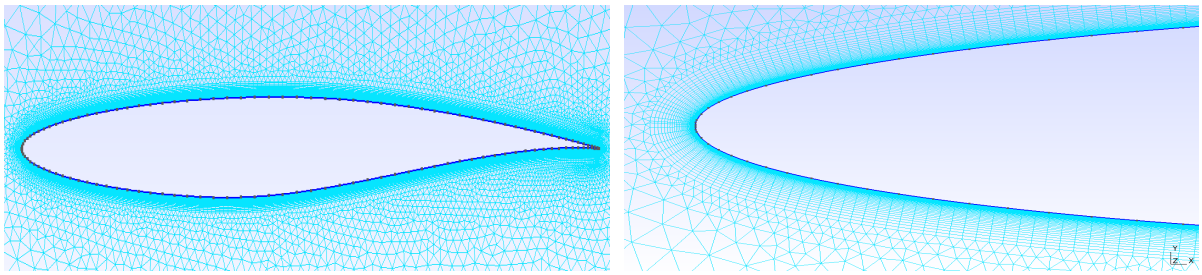

(a) View of the boundary layer refinement.

(b) Zoom in the leading edge discretisation.

Figure 3.3: Mesh refinement surrounding the aerofoil.

It can be clearly seen which areas of the domain gather more importance and how small are the cells in the boundary layer subregion. Moreover, one can notice that outside of the boundary layer region, the mesh is unstructured. The reason behind this, is that the *SU2* software can deal perfectly with unstructured meshes and, in that case where it is difficult to keep the orthogonality of the cells when coupling the aerofoil's geometry with the surrounding grid, it is preferred. Nevertheless, by applying the *BoundaryLayer* function of *Gmsh*, the orthogonality is kept at the most critical region, near the aerofoil.

3.3 Approach towards the simulation

In order to carry out the simulation and to see the results, a script has to be written as a configuration file (**.cfg*) and then, the *SU2_CFD *.cfg* terminal command must be run. A summary of the script is defined in Table 3.2.

FUNCTION	COMMAND	**FUNCTION**	COMMAND
SOLVER	RANS	**CONV_NUM_METHOD_TURB**	SCALAR_UPWIND
KIND_TURB_MODEL	SA	**MUSCL_TURB**	NO
MARKER_HEATFLUX	(AEROFOIL, 0, 0)	**TIME_DISCRE_TURB**	EULER_IMPLICIT
MARKER_FAR	(FARFIELD)	**OBJECTIVE_FUNCTION**	DRAG
MARKER_PLOTTING	(AEROFOIL)	**CONV_NUM_METHOD_ADJFLOW**	JST
MARKER_MONITORING	(AEROFOIL)	**MUSCL_ADJFLOW**	NO
NUM_METHOD_GRAD	WEIGHTED_LEAST_SQUARES	**ADJ_SHARP_LIMITER_COEFF**	3.0
CFL_NUMBER	10	**SLOPE_LIMITER_ADJFLOW**	VENKATAKIRSHNAN
CFL_ADAPT	NO	**ADJ_JST_SENSOR_COEFF**	(0.0, 0.01)
ITER	12000	**CFL_REDUCTION_ADJFLOW**	0.8
LINEAR_SOLVER	BCGSTAB	**TIME_DISCRE_ADJFLOW**	EULER_IMPLICIT
LINEAR_SOLVER_ERROR	1E-6	**FROZEN_VISC_CONT**	YES
LINEAR_SOLVER_ITER	10	**CONV_CRITERIA**	RESIDUAL
MGLEVEL	0	**CONV_RESIDUAL_MINVAL**	-7
LINEAR_SOLVER_PREC	LU_SGS	**CONV_STARTITER**	20
REF_ORIGIN_MOMENT_X	0.25	**DEFORM_LINEAR_SOLVER**	FGMRES
REF_ORIGIN_MOMENT_Y	0.00	**DEFORM_STIFFNESS_TYPE**	INVERSE_VOLUME
REF_ORIGIN_MOMENT_Z	0.00	**DV_KIND**	FFD_CONTROL_POINT_2D
REF_LENGTH	1.00	**DV_MARKER**	(AEROFOIL)
REF_AREA	1.00	**FFD_DEGREE**	(30,1,0)
CONV_NUM_METHOD_FLOW	ROE	**FFD_CONTINUITY**	2ND_DERIVATIVE
MUSCL_FLOW	YES	**FFD_ITERATIONS**	500
SLOPE_LIMITER_FLOW	VENKATAKIRSHNAN	**FFD_TOLERANCE**	1E-12
VENKAT_LIMITER_COEFF	0.05	**VISUALIZE_SURFACE_DEF**	YES
JST_SENSOR_COEFF	(0.5, 0.02)	**OPT_OBJECTIVE**	DRAG * 0.01
TIME_DISCRE_FLOW	EULER_IMPLICIT	**OPT_CONSTRAINT**	NONE

Table 3.2: General view of the user's *SU2* script features

3.4 Mesh convergence study

The procedure used in this study contemplated different aspects to check that the results represent a realistic phenomena. Initially, the information provided by the flow must be gathered and to do so, a y^+ tracking along the aerofoil wall is needed. Once it has been accepted, in order to validate the rest of the mesh and the obtained results, a comparison with the experimental data for the first study, from the report [65] is done. From this point, in Table 3.3 the reader can check which are the different meshes used and how accurate they are.

Table 3.3: Resume of mesh properties

MESH	**# nodes Grid**	**# nodes Aerofoil**	max$\{y^+\}$	*Cl*	*Cd* counts
Coarse	43322	200	0.405	0.6737	138.8
Medium	53492	220	0.105	0.7164	137.4
Fine	75130	240	0.103	0.7205	130.2
Fine (Improved)	85098	240	0.103	0.7215	130.5
Experimental	-	-	-	0.7436	127.0

The *medium* mesh option is the one selected for the thesis, considering the trade-off between the computational costs it involves and the academic purpose of the work. The error in the lift coefficient compared to the experimental setup is low (**3.66%**) but it is possible to notice yet the difference in drag counts, approximately a 7%, but, for the purpose of this work and the limited interval of available time, it is considered to be acceptable, knowing that more accurate results could be obtained then by using finer meshes. More details of the mesh are found in Figure (3.4).

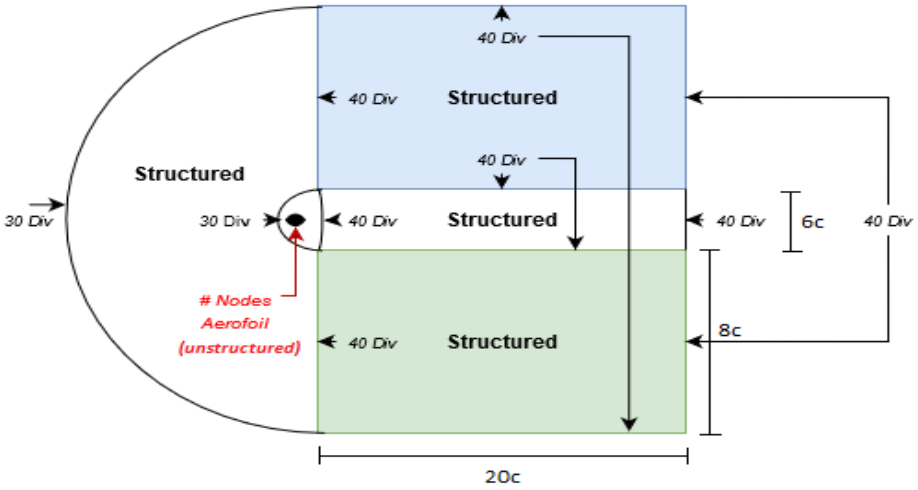

Figure 3.4: Grid accounted for the extraction of the results.

3.5 Free-Form Deformation box

To optimise a rigid shape of a geometry, one of the most common technique used is the *Free-Form Deformation* (FFD) procedure, which is able to modify the initial position of the object by embedding another geometrical shape. Any modification at the free-form control points, will act as a movement in the original shape.

For the aerodynamic shape optimisation, the aerofoil must fit inside the designed deformation box without intersecting any of the control points (CP) nor the connecting lines, even though the closer, the better. In that way, the deformation of the CP would have more influence in the geometry closer to it. Therefore, the designed FFD box is represented in Figure (3.5).

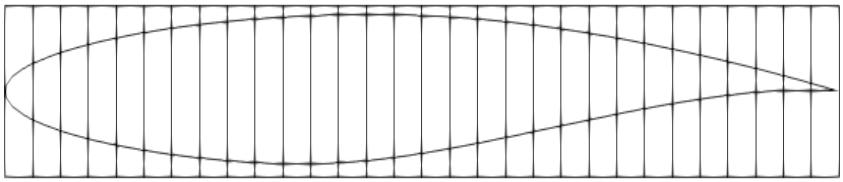

Figure 3.5: Distribution of the Control Points for the Free-Form Deformation box.

An example of a modified aerofoil is the one presented in Figure (3.6), where only one CP has been deformed and no wing-box constrain has been applied. It is possible to note how a simple movement on a CP has an influence towards the position of the neighbouring ones so as to comply with the geometrical continuity formulation of the model (e.g. splines or Bézier curves).

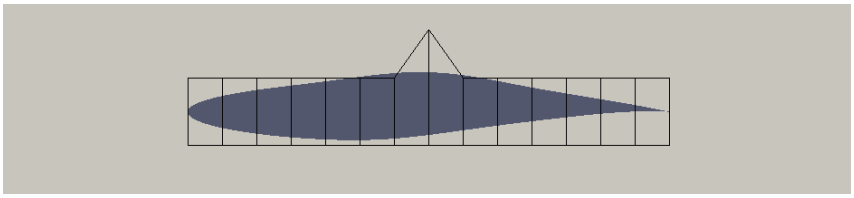

Figure 3.6: Deformation of the FFD by one CP and the aerofoil embedded inside.

Once the basis of the deformation methodology have been presented, the focus should be redirected again towards the case study. Recalling the information stated in section 3.1, the RAE 2822 shape must consider the presence of the wing-box constraint. Usually, it is considered to be located between *0.25c - 0.75c*, therefore, the control points in this interval will not serve as a design variable as no movement or deformation can be applied to them. In Figure (3.7), the RAE 2822's wing-box is defined in red.

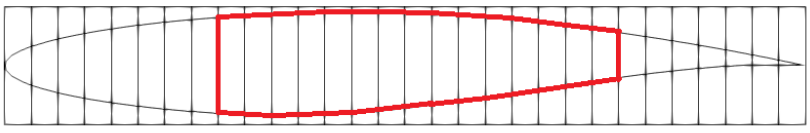

Figure 3.7: Wing-box structure constraint.

After the constraint, only the leading and trailing edge (LE and TE) geometries can be modified. On one hand, it should be noted that the source with higher influence in the domain, regarding the aerodynamic coefficients, is the shockwave appearance, as it can be seen in the studies [66] and [67], which unfortunately is found inside the wing-box constraint, meaning that the main root for optimisation of the aerofoil's shape is inaccessible. On the other hand, studying the LE and TE can also reproduce a big improvement towards the design features as it is going to be shown in section 5.2.

3.6 Adjoint methodology

In this section, the sensitivities of the adjoint method are going to be analysed and discussed so that, afterwards, it can be understood how the deformation in the geometry has been carried out. From this point, surface sensitivities are presented for the actual case study and, following them, a brief description of their meaning and forward procedures are given. Before that, the control points identification is presented:

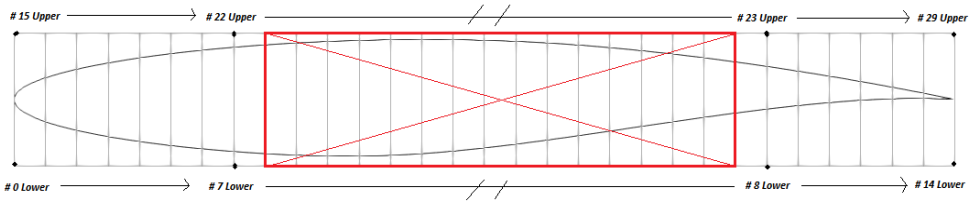

Figure 3.8: Control Points identification

The sign of the sensitivity parameter is the result of the influence that has a modification of an input parameter (vertical movement of the CP in the case study) into the output (*lift-to-drag ratio*) one, for example, a positive axis displacement input will lead to a negative variation of the output. To check this phenomena, the sensitivity has been plotted for each of the control points in Figure (3.9) but note that the first 15 CP refer to the lower side of the aerofoil while the rest refer to the upper side. One can notice that the values presented represent how influential are the present nodes in the aerofoil's geometry to the studied objective function, the lift-to-drag ratio. One can understand that near the trailing edge the influence is higher than those in the leading edge and the rest of the aerofoil, which are nearly non-influential.

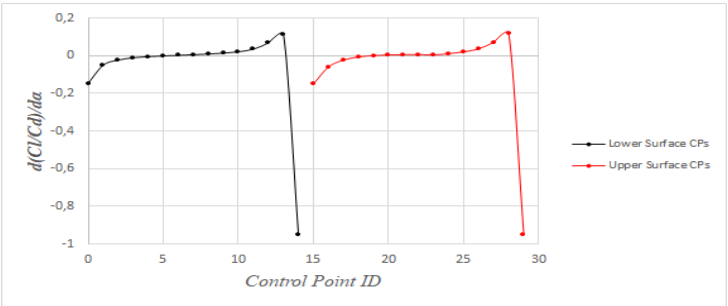

Figure 3.9: Sensitivity behaviour for the *lift-to-drag* ratio for each control point.

Chapter 4

Structural methodology

In this chapter of the thesis, the first steps of the aerofoil structural analysis are going to be established and presented. The target is to set the general case study, with its corresponding definition and simulation components, and how the methodologies to obtain significant results, are going to be implemented.

4.1 Case study

Once the aerodynamics results are obtained, the pressure distribution along the surface of the aerofoil can be used as an input to *Finite Element Methodology* (FEM) implementation. A skin thickness of 0.002c is imposed to the geometry previously defined. A graphical representation of its application is shown in Figure (4.1).

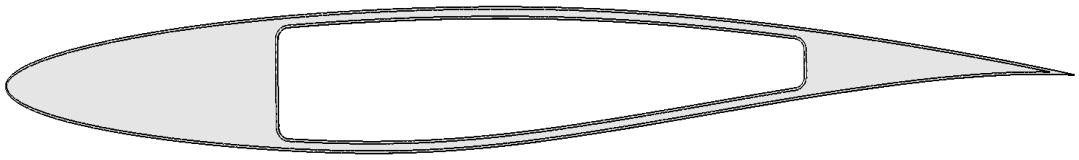

Figure 4.1: Graphical representation of the RAE 2822 case study complemented with the aerofoil and wing-box skins.

The structural layout refers to the selected design for the wing-box structure, according to the methodology process presented in section 3.5, and to the skin of the aerofoil which is, afterwards, going to be used as a constraint for the topology analysis. Moreover, by referring to Figure (3.7), a thickness-related constraint of 0.008c for the wing-box geometry conservation in the topology analysis is added.

An aluminum alloy is chosen as the material for this study, due to its wide application in aeronautics [68] [69]. The starting structural properties and characteristics employed in this study are summarised in Table 4.1.

Table 4.1: Aerofoil structural properties and initial surface.

Material	**Elastic Modulus** ***E*** $[GPa]$	**Poisson's coefficient** ν	**Density** $\rho_m[Kg/m^3]$	**Surface** $S_{aero}[c^2]$
Aluminum alloy 6061	68.9	0.33	2700	0.03086

A model has been designed again using *Gmsh*, with an interval between 75000 and 80000 triangular elements which their value depend on the geometry. Note that the element's size is in the order of 0.001c. After the mesh is generated, *Calculix* provides a FEM solver that enables the user to analyse any given structure such as the one studied here. Before running the FEM solver, the boundary conditions should be established. These consist not only of the loads applied to the structure, but also the physical constrains applied to it.

The load applied to the structure is the pressure distributed throughout the aerofoil surface. This load is given by *SU2*, which provides data for each node of the surface mesh as an output. A pre-processing analysis should be done to translate the output file obtained by *SU2* to the one read by the *Calculix* software, which is based on a data file written in the format code **.inp* and used as an input for engineering problems. To do so, a Matlab® script was written to provide this input file, which is attached at the end of this document in case the reader is interested.

Initially, and specifically if the used CFD mesh provides a disordered nodes' distribution, it is recommended to modify that initial file. Therefore, the steps to be followed depend on the procedure to be used and, for this thesis, there are just pressure values at the nodes. Thus it would be appropriate to modify them such that proper loads are transferred to the structural mesh.

Then, two options arose and in terms of the *Calculix* nomenclature, the *CLOAD* and the *DLOAD*. The first one uses concentrated loads at the specific nodes and with their correspondent vector direction, while the second applies a pressure value at a certain line/surface (2D or 3D). It may seem clear, that the easiest path to be followed, is the latter, but because of the studied case it may not be possible or just be too complex. The reasons behind this is that to apply the *DLOAD* technique, the nodes should be contiguous to each other, thus following a sequential positioning. In the majority of the cases, that depends on the meshing software and methodology used.

In the studied case, a mesh refinement along the trailing edge was needed for the CFD analysis and this modification lead to a more complex output file. Moreover, the *DLOAD* used as a space variable the line (in 2D) which connected the two nodes and, since the aerofoil geometry was defined as a polyline (spline) for simplicity and accuracy purposes, there was not any specific segment that acted as a bridge between nodes. The only solution then was to use the edge created by the meshing algorithm but for a approximately 80000 elements it is clearly inefficient.

From this point, it was clear that the methodology should keep the nodal character of the CFD output, but a modification to the pressure values should be done. First of all, it is clear that surfaces are needed to translate pressure distributions to loads thus, as the case is bi-dimensional, the third-axis direction was established as the unity. Subsequently, the second direction needed would be the segment involving the nodes.

The next task to be accomplished is the positioning of the load itself. As the pressure was discretised in the nodes, the loads should follow the same behaviour. Therefore, the load is applied in the node where its correspondent pressure value was obtained. To do so, the second space variable is defined using the initial geometry lines between nodes. By coupling the halves of the previous segment and the following one coming from the primary geometry, a balanced and accurate representation is achieved. In addition, the pressure value is not applied then in the initial node, but in an similar and close location inside the new formed line and, by following the direction of its normal vector. Then, the sign of the vectorial force depends on the magnitude of the pressure, being towards the inner structure when the pressure is positive and vice versa. A graphical support is shown in Figure (4.2).

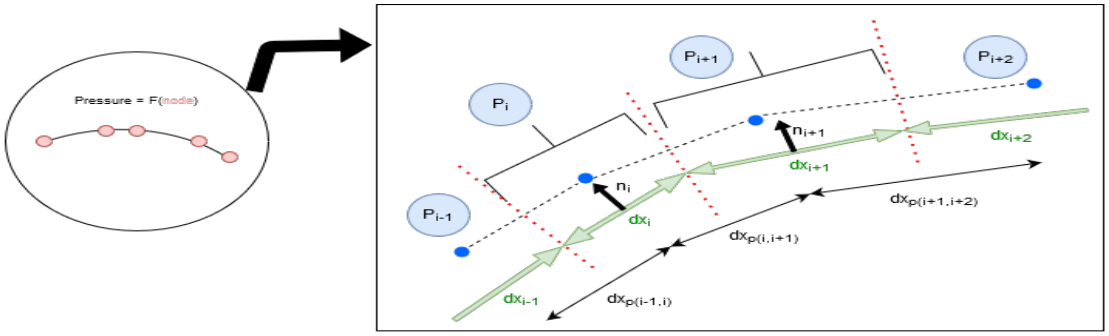

Figure 4.2: Methodology used to apply concentrated loads from discrete pressure values.

In Figure (4.2), initial nodes are marked in blue and the geometry is represented by black dashed lines. Then, the distance between nodes is also provided with the variable $dx_{p(node1,node2)}$. The pre-processing before the FEM analysis consists in dividing the initial segments in their mid-point, as seen with the dotted lines in red, subsequently there are the new segments which connect the mid-nodes and save the information in the dx_i variable, which has also its own normal vector $\hat{n}_i$. Therefore, and showed by the brackets, the pressure value from the specific node is applied along that surface defined by $(dx_i \times 1c) \cdot \hat{n}_i$. A representation of the results is shown in Figure (4.3).

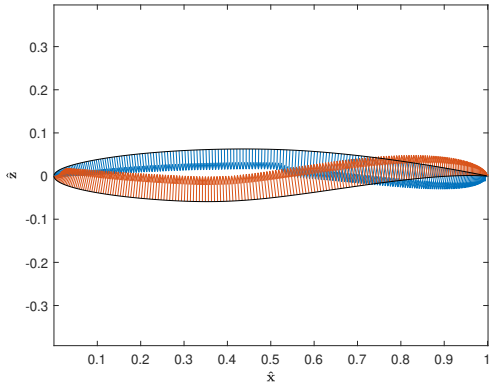

Figure 4.3: Pressure field translated into loads for the RAE 2822 case study.

One can note the influence that the shockwave has on the load distribution along the upper surface, specifically around the x-coordinate 0.5c and 0.6c. The reason behind this is the flow's speed reduction, thus the increase of the pressure magnitude. Moreover, all the loads follow each of the normal vectors obtained by the discretisation procedure illustrated in Figure (4.2) and how the lower surface magnitudes are higher than the upper ones, leading to an upwards lift force.

Once the migratory procedure of the surface pressure from the CFD environment to the FEM is done, the implementation of the *Calculix* script should be defined. First of all, the mesh provided by the *Gmsh* software needs to be adapted to the **.inp* format style. To do so, the physical groups should be defined previously in the *Gmsh* environment and then export the mesh file as the stated format. By doing so, it is simpler and easier to define the boundary conditions and the constraints of the setup.

The constraints of the model have been applied at the wing box, forcing null displacements at its internal faces as it can be seen in green in Figure (4.4) apart from the thickness-related threshold of 0.008c specified previously for the topology optimisation process.

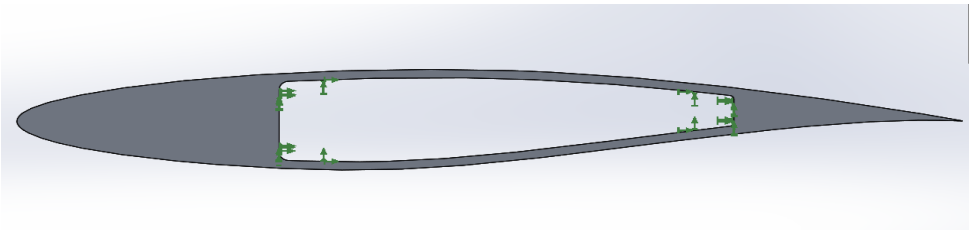

Figure 4.4: Fixed faces constraint at the wing-box.

4.2 Verification of the structural mesh

The procedure used in this study follows the same path as the one described for the aerodynamic's case. Then, different aspects were contemplated to check that the results represent a realistic phenomena. Initially, and because of the mesh dependence feature, the results vary in distribution along with the mesh quality and quantity, so the first task carried out was to find a mesh distribution able to provide consistent results and practically not influenced by the number of nodes.

After that, a convergence study on the mesh size was done by comparing the main variables of the study, which are the displacements suffered by the structure and the stress distribution which may lead to certain failures. Six different meshes were built and their results are shown in Table 4.2 and Figure (4.5). Because of the acceptable computational cost involved and a better expected accuracy in the results, the mesh with 77144 elements has been selected for the study.

Table 4.2: Resume of mesh properties

MESH	# nodes	σ_{VM}^{MAX} [*MPa*]	abs(*Max-Displacement*) [10^{-6} c]
Coarse	20812	3.78	91.8
Medium	31532	1.36	5.15
Fine	60916	2.24	8.82
Fine (Improved)	67184	2.51	14.5
Extra-Fine	73640	2.59	14.7
Extra-Fine (Improved)	77144	2.63	14.7

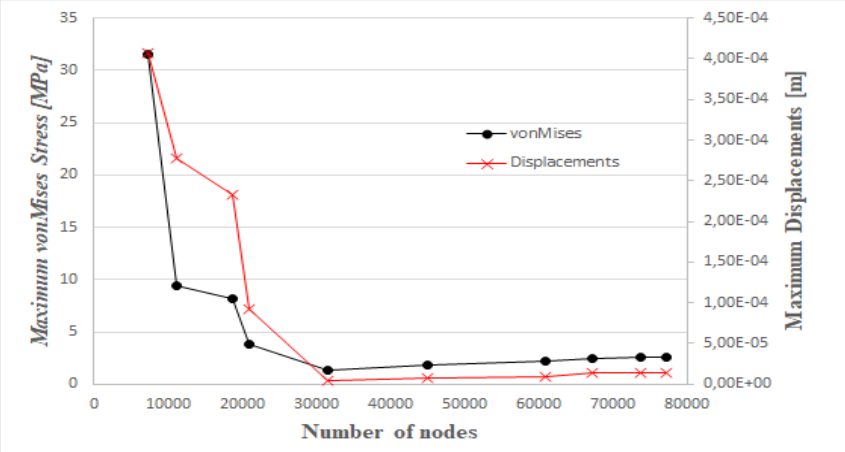

Figure 4.5: Structural variables' evolution with the number of nodes.

4.3 BESO procedure and the selected variables.

The Bi-Directional Evolutionary Structural Optimisation (BESO), which it is graphically described in Figure (2.7), a few parameters should be selected in order to start the process. Take into consideration that the output results given by the solver are completely dependent of those (*e.g.* filter radius and mass removal ratio among others) thus an infinite value of possibilities may arise from one general case study. During this chapter of the thesis, a general review of the effects that one parameter has along the optimisation is going to be given and complemented with its general considerations for its use.

To begin with, the user must setup the constraints for which the optimisation is aimed. Inside the BESO code [28] developed for *Calculix*, there is: the mass (or volume) constraint, which is common for all this type of studies; the structural optimisation parameter, which can be chosen between: the maximisation of the stiffness (minimisation of the compliance), the failure index, minimisation of the buckling phenomena or the maximisation of the heat flow; the sensitivity filter to avoid the checkerboard layout; and the material ratios.

In order to achieve the targeted value for the weight reduction parameter, the mass addition and removal ratios are defined. Therefore, if the mass of the object has to be decreased, the proportion of these two ratios should be balanced towards the extraction of mass. Depending on the magnitude of the difference between ratios, more or less iterations are going to be required by the solver, but note that the higher the difference between ratios the harsher the convergence evolution. Moreover, sometimes the mass target may not be reached due to structural failures, thus the code by itself provides the more stable and compatible solution with the structural and lower mass constraint, such as on cases shown in Figures (4.6) and (4.8), where its correspondent convergence graphs show their final insufficient mass magnitude.

The first parameter used to check the behaviour of the optimisation is the filter radius, but initially the set of different filters should be presented, as it has been done in Table 4.3.

Table 4.3: List of filters used in the BESO script provided by [28]

Filter type	**Description**	**Main influence**
Over Nodes	Filtering using the *Heaviside* step function over geometric nodes providing binary results	Neighbour cells
Over Points	Filtering using the *Heaviside* step function over mesh points providing binary results	Neighbour cells
Simple	The one described in section 2.2 where the sensitivity value is obtained by averaging the ones from the neighbouring cells	Neighbour cells
Dilate Sensitivity	The density of the element *e* takes the maximum of the densities in the surrounding nodes. Then, it can only set to solid conditions	Radius range after sensitivity domain
Erode Sensitivity	Opposite form of the Dilate filter, thus a minimisation is aimed and void conditions are given inside the specified radius	Radius range after sensitivity domain
Open Sensitivity	Erosion filter followed by the Dilation one	Radius range after sensitivity domain
Close Sensitivity	Dilation filter followed by the Erosion one	Radius range after sensitivity domain
Open-Close or Close-Open Sensitivity	Used to obtain minimum hole size and structural detail. Then, 4 filter operations are required	Radius range after sensitivity domain
Combine	Combination of the close and open filters	Radius range after sensitivity domain
For further detail on filters, check the work made by *Sigmund, O. [70]*.		

Following the BESO authors [28] way of working, the simple filter is going to be applied along all the optimisations. Then, for the selected approach, the mesh elements size should be considered as is an approximate idea about the extension of the solid elements sensitivities towards the void ones. From this point, it is necessary to point out that the larger the parameter the higher it would be the result of its influence and vice-versa.

Initially, a fixed mass removal ratio of -2 and two different radius have been selected. The first one considers an area of radius 0.01c (approximately 10 times the mesh element's length) while the second, 0.005c. Then, it is expected that the latter has a finer distribution of solid elements. Moreover, the

chosen material has been randomly selected to be polypropylene, just for demonstration purposes, and a 90% weight reduction is aimed. This initial threshold of the weight reduction has been set by understanding that, in order to demonstrate the effect the BESO variables have, it requires a less constrained path to develop completely, thus allowing the software to produce noticeable changes. Nevertheless, in the future sections of the thesis, different volume constraints will be shown.

From this point and by checking Figures (4.6-4.9), the influence of the filter can be understood. Initially, the mass-reduction procedure will be checked until a final solution is achieved. By then, a graph showing the solution's convergence will be plotted and, afterwards, a review will be provided.

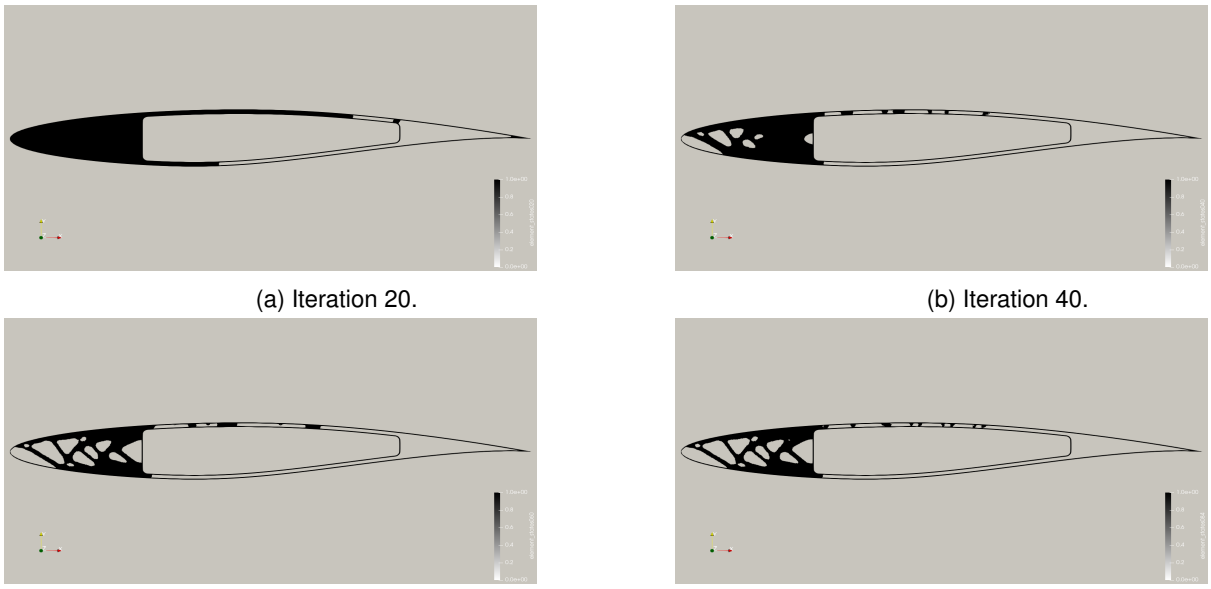

(a) Iteration 20.

(b) Iteration 40.

(c) Iteration 60.

(d) Final iteration.

Figure 4.6: Topology optimisation procedure development for the case study using polypropylene, mass constraint of 10% and filter radius of 0.01c.

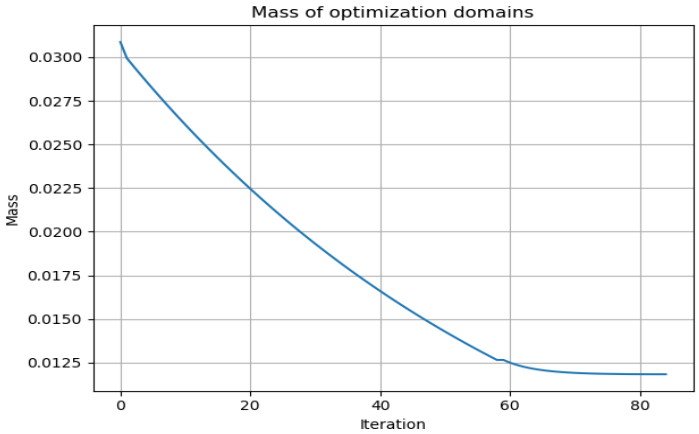

Figure 4.7: Mass convergence using polypropylene, mass constraint of 10% and filter radius of 0.01c.

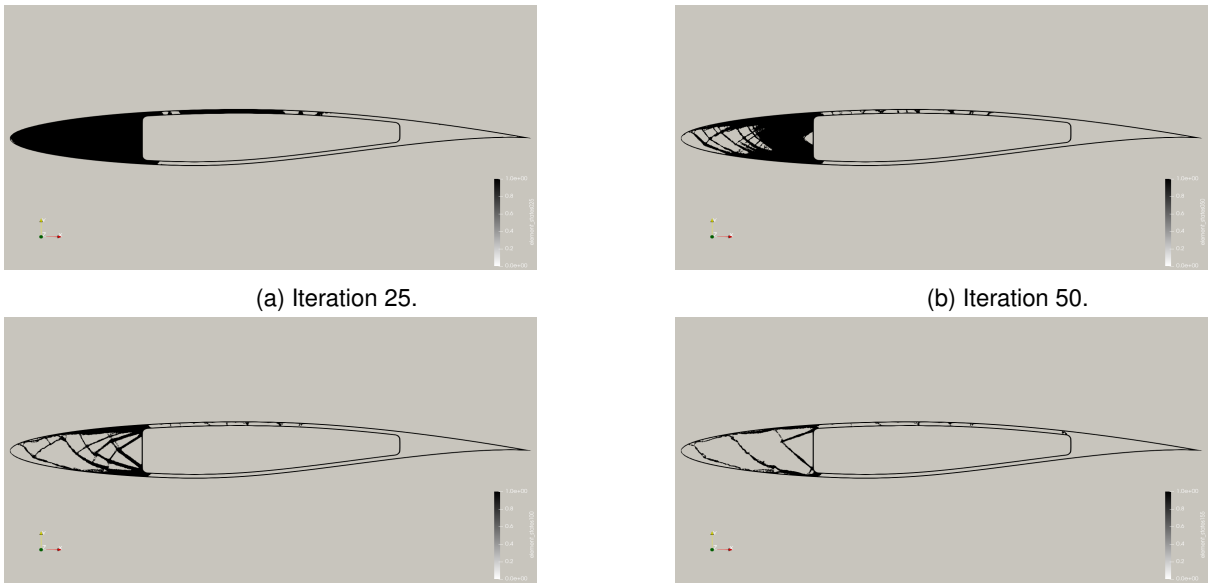

(a) Iteration 25.

(b) Iteration 50.

(c) Iteration 100.

(d) Last iteration.

Figure 4.8: Topology optimisation procedure development for the case study using polypropylene, mass constraint of 10% and filter radius of 0.005c.

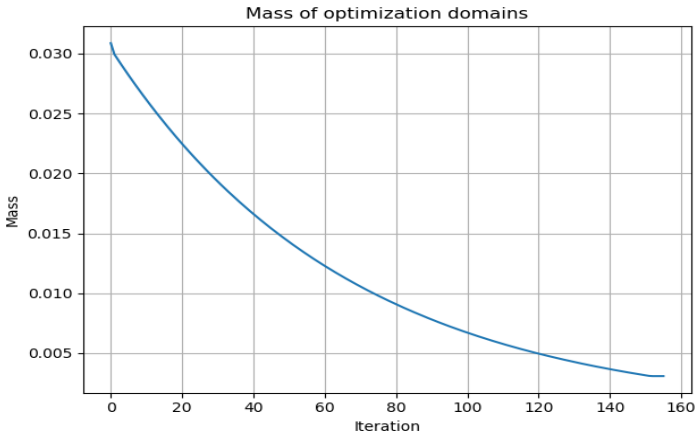

Figure 4.9: Mass convergence using polypropylene, mass constraint of 10% and filter radius of 0.005c.

Note that the value shown in the graph regarding the mass magnitude is a representative value of the amount of remaining aerofoil's surface[1]. Check that for the polypropylene material using the same mass constraint and different filter radius, just the case of the 0.005c length filter radius reaches the targeted surface constraint ($\sim 0.003086c^2$).

Then, the thicker filter radius would provide an insufficient weight reduction state when reached the final iteration. Therefore, the selection of the material and the properties within it are also a field of study. For the other case, a finer filter may lead to a more accurate state as the solver has more availability (less

[1] The BESO software considers: $mass = Volume \cdot \rho_{mat}$, where ρ_{mat} is the average density between the void and filled elements, being $\rho_{void} = 0$ and $\rho_{fill} = 1$, thus $\rho_{mat} = \frac{\sum_i^N (\rho_{void} + \rho_{fill})}{N}$

constraints) to remove and create elements inside the domain. Then, it is possible to reach a lower final mass. For instance, for the case shown in Figure (4.8), the final surface is $0.011833c^2$ while for Figure's (4.6) is $0.003086c^2$, both with starting point $0.03086c^2$, meaning an approximate difference of 75%. It is also possible to distinguish the influence of the filter's radius in the latest scheme for each of the simulations by looking at the generated truss structure at the proximity of the leading edge.

Nevertheless, from Figures (4.7) and (4.9) it can be concluded that, for a smaller filter radius, the number of iterations required to reach convergence increases as more diversity of states can be achieved.

Hereafter, having in mind already the effects of the selected material and the sensitivity filter radius, the ratio between the added and removed mass is studied. As the geometry of the aerofoil starts by being completely filled, the mass removal ratio should be higher than the adding one, but the influence of them at each iteration is going to be analysed.

Moreover, in order to just note the influence the mass removal ratios have in the process, the initial conditions from which this exploratory study started (mass removal target of 90% and filter of radius 0.01c) are going to be applied, even though better results could be obtained by, for instance, reducing the filter radius. Then, beginning with a ratio of -2, followed by a ratio of -8 and ending with a ratio of -15, in Figures (4.10-4.13) the extracted results will be plotted and checked.

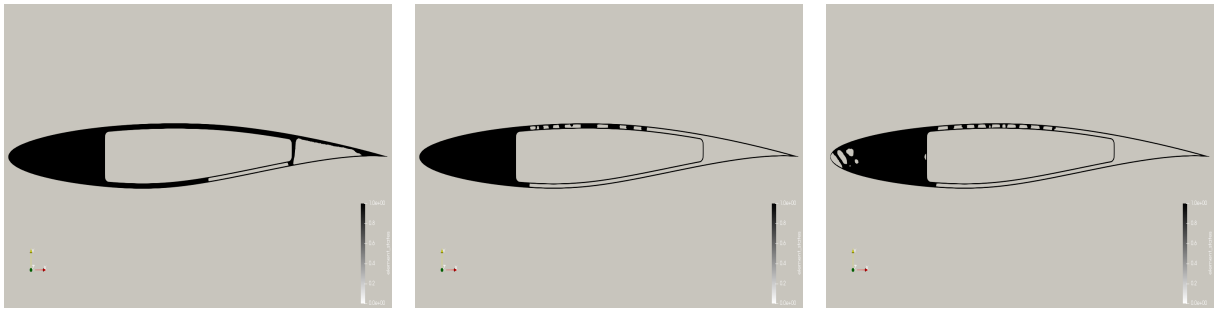

(a) Iteration 20. (b) Iteration 40. (c) Last Iteration.

Figure 4.10: Topology optimisation procedure development for the case study using polypropylene, mass constraint of 10%, filter radius of 0.01c and mass ratio of -2.

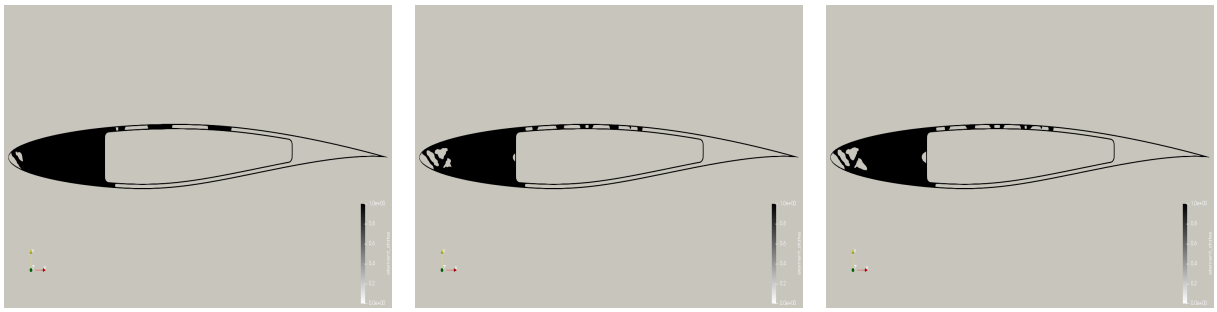

(a) Iteration 10. (b) Iteration 20. (c) Last Iteration.

Figure 4.11: Topology optimisation procedure development for the case study using polypropylene, mass constraint of 10%, filter radius of 0.01c and mass ratio of -8.

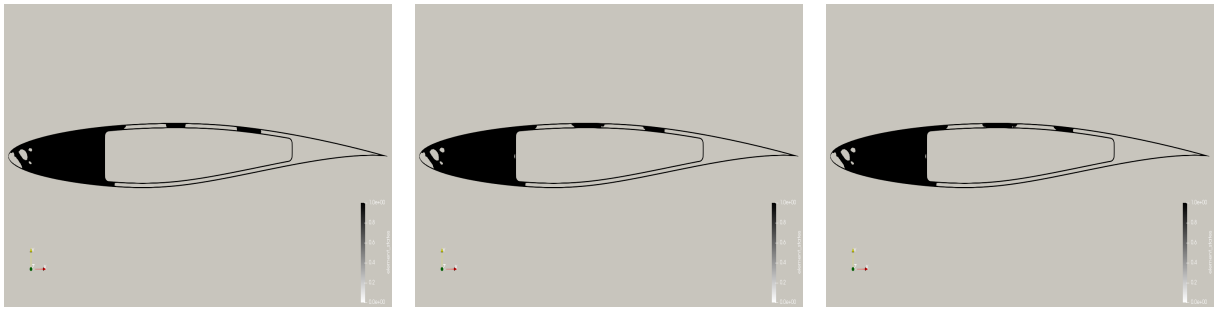

(a) Iteration 10. (b) Iteration 20. (c) Last Iteration.

Figure 4.12: Topology optimisation procedure development for the case study using polypropylene, mass constraint of 10%, filter radius of 0.01c and mass ratio of -15.

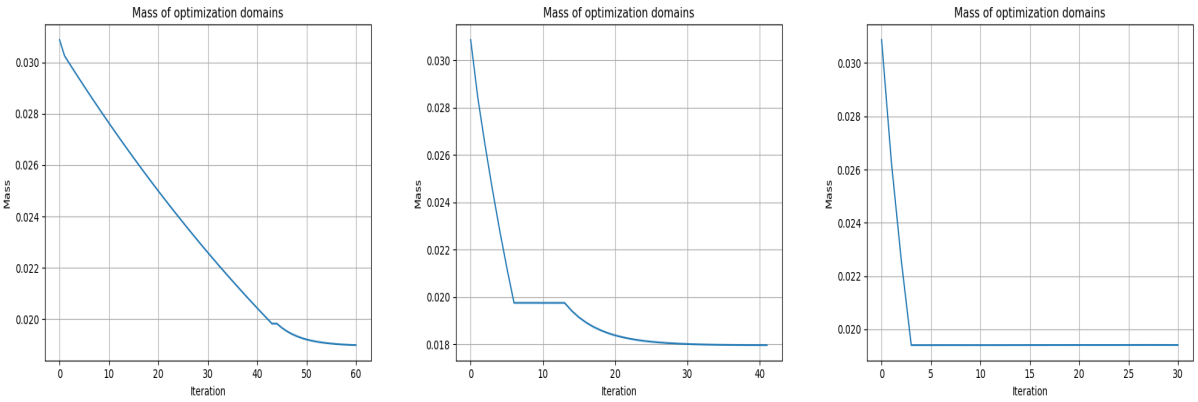

(a) (b) (c)

Figure 4.13: Mass convergence using polypropylene, mass constraint of 10%, filter radius of 0.01c and mass ratio of: (a) -2, (b) -8, (c) -15.

The first aspect to point out from the volume removal evolution is that, by comparing Figure (4.6) and (4.10), which both of them have the same properties, the final solution is totally different. The reason behind this lies not in the mass removal ratio but the values used to define it. For instance, in Figure (4.6)'s case, the removal magnitude is 0.03 and the adding one is 0.015, while for the other case, they are 0.02 and 0.01 respectively.

This unbalance in the final solution is generated by the conditioning properties of the material modifiers, as for each of the iterations, they try to reach the target specified by the user. Therefore, an adequate ratio should be procured as it can provide a more efficient layout design.

Moreover, the higher the ratio the lower the number of iterations required to find a final state. Nevertheless, as it can be seen in Figure (4.13), a more softer and continuous evolution is achieved in this specific rate. This means that a wider field of topology options are available. Furthermore, by having a higher ratio of mass removal, the final weight of the object may not be the smaller value, as it tends to force the generation of void elements and thicker structures are generated until there is no more available mass to remove following the established ratio. In Figure (4.13a), the achieved value is $0.0189c^2$, a remaining magnitude of 61.24%. For a ratio of -8, the resulting volume value is $0.0187c^2$, a remaining magnitude of 60.59%, and, finally, for the -15 removal ratio, $0.0194c^2$, a remaining magnitude of 62.86%. Therefore, it is necessary to point out that none of the cases reached the volume constraint target but that the higher the ratio, the faster but less accurate the solution is.

On one hand, a reason that may be laying behind this underachieved target is the value of the mass addition ratio. If it is too low, the solver by itself has difficulties to recover all the needed voids to become solid and then stiffer. Then, a balance should be found between both ratios and it only can be done by a list of experimental setups.

On the other hand and, as a counterpoint of the increased ratio of removal, the skin's failure index (*FI*) increases drastically. For the highest removal ratio, Figure (4.12), the FI is two times higher than the yield stress parameter of the polypropylene material ($\sigma^{PP}_{yield} = 35$ MPa). Therefore, the solution is totally unaccepted for the established conditions. Differently for the other two cases, the provided solutions are inside the material resistance domain. For the intermediate, $FI \approx 50\%$, and, for the softer, $FI \approx 20\%$. All of the maximum values were reached in the skin layer. These values are completely dependant on the selected material, thus more efficient magnitudes could be obtained by an exhaustive study regarding the mechanical properties of the element.

As a concluding remark from this exploratory study, which will lead to the future study of the main purpose of the thesis, a stronger and more resistant material will be used so as to reach the volume constraint of a 90% mass reduction, even though its density may be higher. The maximum value for the mass removal target is set to a 10% as, for values below this magnitude, the remaining surface expressed random non-connected inner structures, thus not a converged final solution. Moreover and aiming at a simpler design with thicker truss structures in the inner distribution, a filter radius of 0.01c, which represents 8-10 times the mesh element size, will be selected. Then, a mass removal ratio of 4% and the additive of 1% are set to obtain the desired results regarding the established targets.

Chapter 5

CFD Results

In this section of the document, the CFD results obtained along the project are going to be presented and described. Initially, the reader is going to be introduced towards the flow behaviour for the selected case study and afterwards, a step-by-step analysis for the aerodynamic shape optimisation methodology is presented.

5.1 Flow simulation

Once the mesh has been validated, one can provide the obtained results and compare them with the experimental data. In that case, for validation purposes, the pressure coefficient of the simulation and the one from the experimental setup [71], validated by the *NPARC Validation Organization* are compared in Figure (5.1).

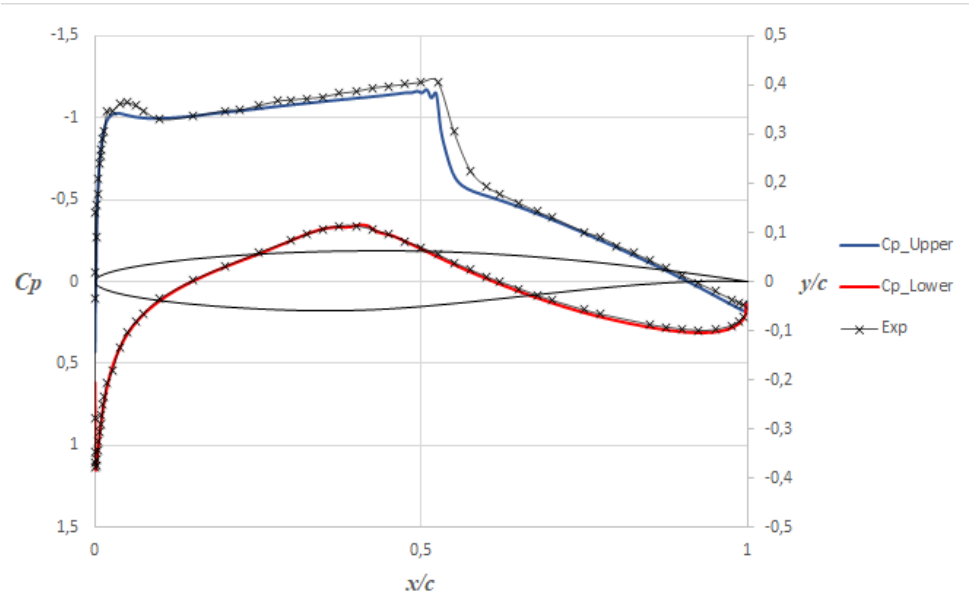

Figure 5.1: Pressure coefficient of the simulation and the one from the experimental setup.

It is possible to see the similitude between results and where the shockwave appears, which is approximately at the x-axis position of 0.55c. In Figures (5.2) and (5.3), the behaviour of the flow surrounding the *RAE 2822* aerofoil is given.

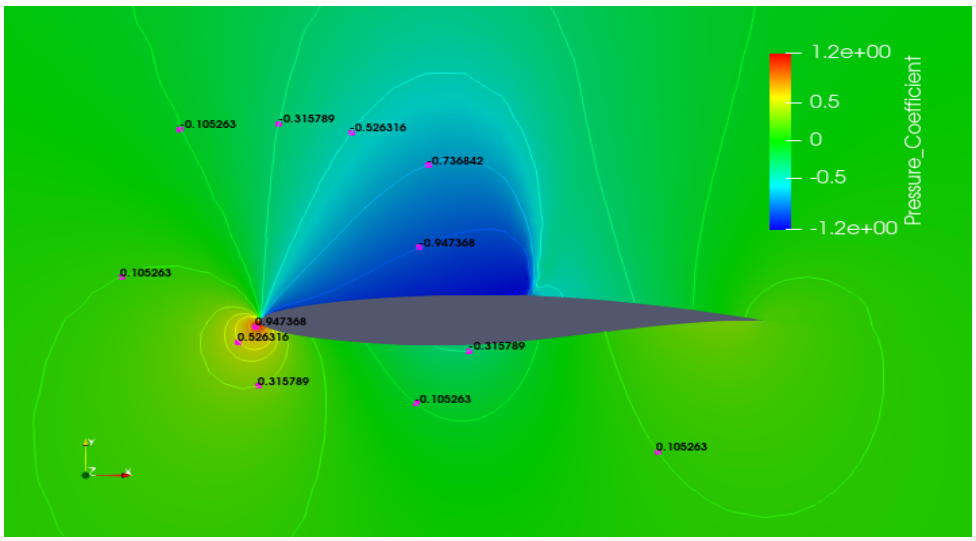

Figure 5.2: Pressure coefficient distribution along the aerofoil.

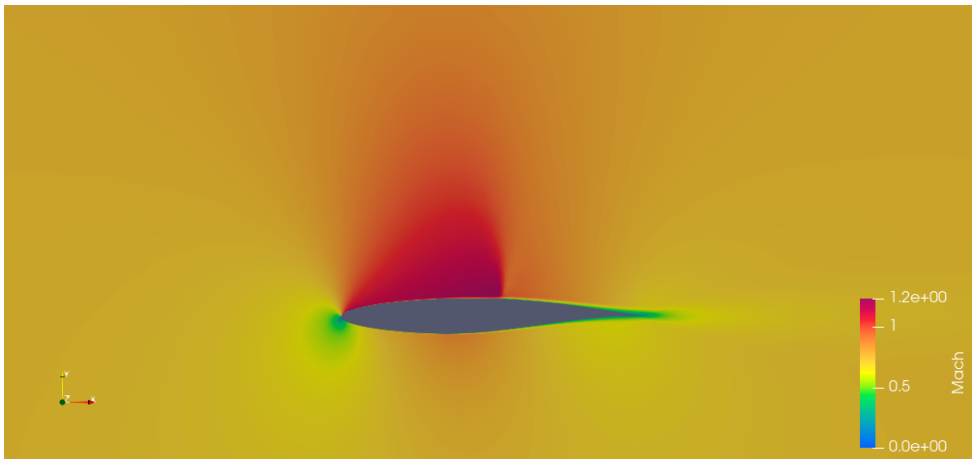

Figure 5.3: Mach distribution along the aerofoil.

From the last figures regarding the pressure coefficient and the Mach's number distribution, it is possible to note where the shockwave appears and how it modifies the behaviour. That shockwave position slows down the flow to values below Mach 1 and, afterwards, as the pressure gradient provided by the aerofoil's geometry is positive, the flow's speed further reduces. Moreover, one can see that, even though the appearance of the discontinuity, the boundary layer does not separate.

Focusing in the trailing edge region, the boundary layer thickness grows with the positive pressure gradient provided by the geometry but at the ultimate vertex, the upper and lower flows, tend to be driven in the same direction.

5.2 Optimised aerofoil's shape

SU2 software incorporates in its environment the capability to couple the whole CFD optimisation framework. To do so, *SU2* gathers a set of scripts involving the CFD, the adjoint and the mesh deformation analysis by using the *Sequential Least SQuares Programming* (SLSQP) module from the *SciPy* library of Python for the minimisation procedure of a given objective function. By coupling the open-source packages *NumPy* and *SciPy* the resulting optimisation procedure in *SU2* is numerically and computationally efficient and robust. The features of both libraries can be found in [72] and [73] respectively.

The idea behind the process comes from a modification of the *Lagrangian* multipliers for an optimisation process, the Karush-Kuhn-Tucker [74], which by default is set at 10^{-10}, and provides a *global optimal* by satisfying the conditions build by the objective function, the design variables, the equality constraints and a convex function state.

In order to proceed with the optimisation procedure, the python script must be defined so as to execute a recurrent set of functions which include the CFD analysis, the geometry checks, the adjoint methodologies, deformations of the FFD and the general mesh and then the application to the original shape. The solver will be testing new geometries until convergence criterion has been reached.

The main goal of the project was to optimise the aerofoil by means of its efficiency (lift-to-drag ratio), which is one of the most interesting from the aeronautical point of view. However, the test gave as an output only a **0.15%** of improvement. This means that the aerofoil, for this specific flow conditions and wing-box constraint, is quite optimised and that there is a balance in the final result between the changes in the lift coefficient and the drag one. In order to avoid this type of 'loop' in the efficiency optimisation, it has been decided that for this case study, the lift is going to be established as *fixed* while the variable to optimise is going to be the drag produced by the aerofoil. The value of the lift coefficient is the one output from the simulation, *Cl = 0.7164*.

The optimised solution for the case study involves small deformations (seen in blue in Figures (5.5a) and (5.5b)) near both aerofoil's edges. Despite small, these changes reduced the drag coefficient by **13.9%** as it can be seen from Table 5.1. The convergence behaviour is also presented below, in Figure (5.4).

Table 5.1: Aerodynamic Coefficients for the optimised aerofoil's shape.

Shape	***Cl***	***Cd* counts**
Original	0.7164	137.40
Optimised	0.7164	118.23

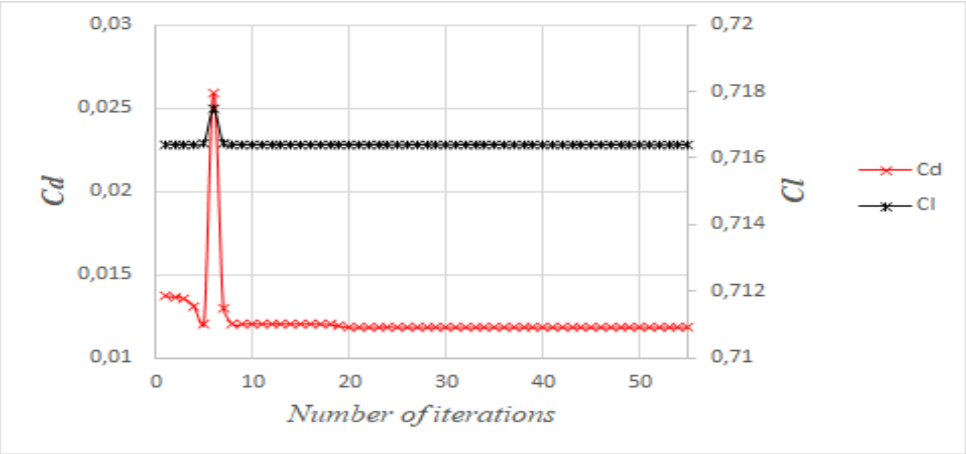

Figure 5.4: *Cl* and *Cd* variations along the shape optimization process

Peaks in the *Cl* and *Cd* variations in Figure (5.4) are caused by the optimisation algorithm when searching for solutions further away from the original, which may lead to divergence. That is why the script incorporates a scaling factor for the objective function and for the gradient methodology.

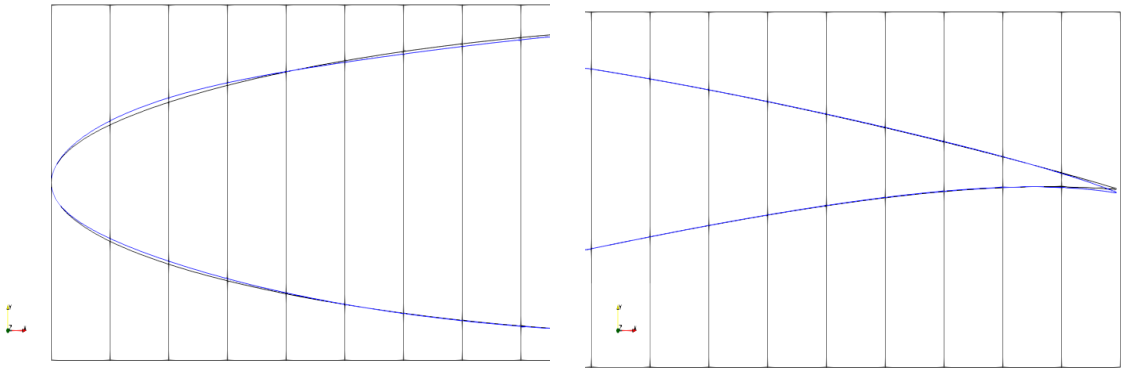

(a) Shape modification at the leading edge.

(b) Shape modification at the trailing edge.

Figure 5.5: Shape modifications applied in the original RAE 2822 aerofoil.

When analysing the pressure distribution shown in Figure (5.6), it is possible to observe that even for small modifications in shape the pressure distribution substantially changes. The magnitude of the largest deformation is $0.1\%c$, thus the sensitivity of the changes in the geometry have plenty of weight towards the final result. Note that the solver, in order to reduce the drag while constraining the lift, tries to slow down the flow when getting closer to the formation of the shockwave so as to absorb some of the kinetic energy of the flow and, as the counterpart, this speed decrease is adjusted close to the leading edge by providing more curvature, thus a higher pressure gradient.

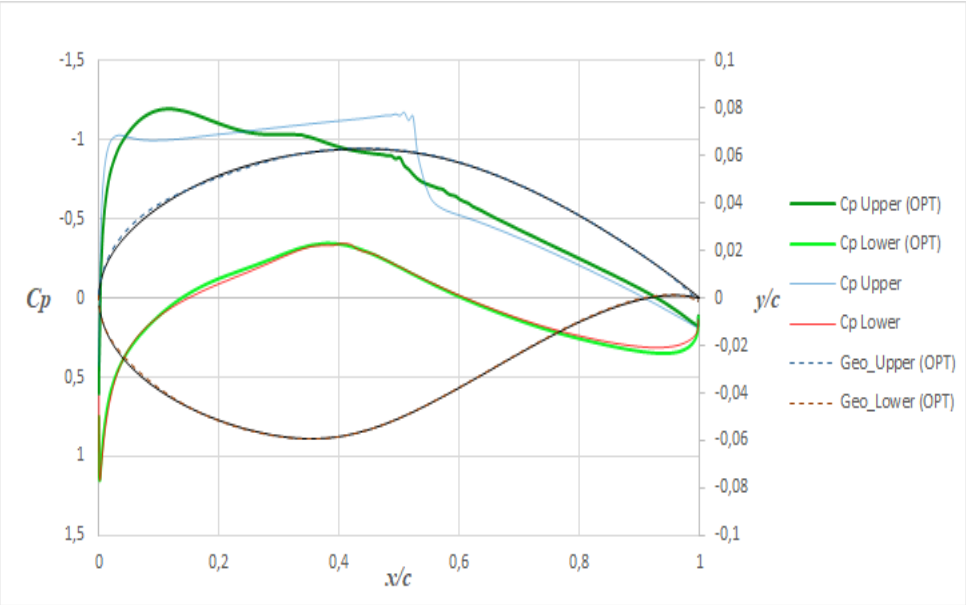

Figure 5.6: Pressure coefficient comparison.

The shock was soften by the optimised shape as can be seen from both Mach and pressure distributions in Figures (5.7) and (5.8).

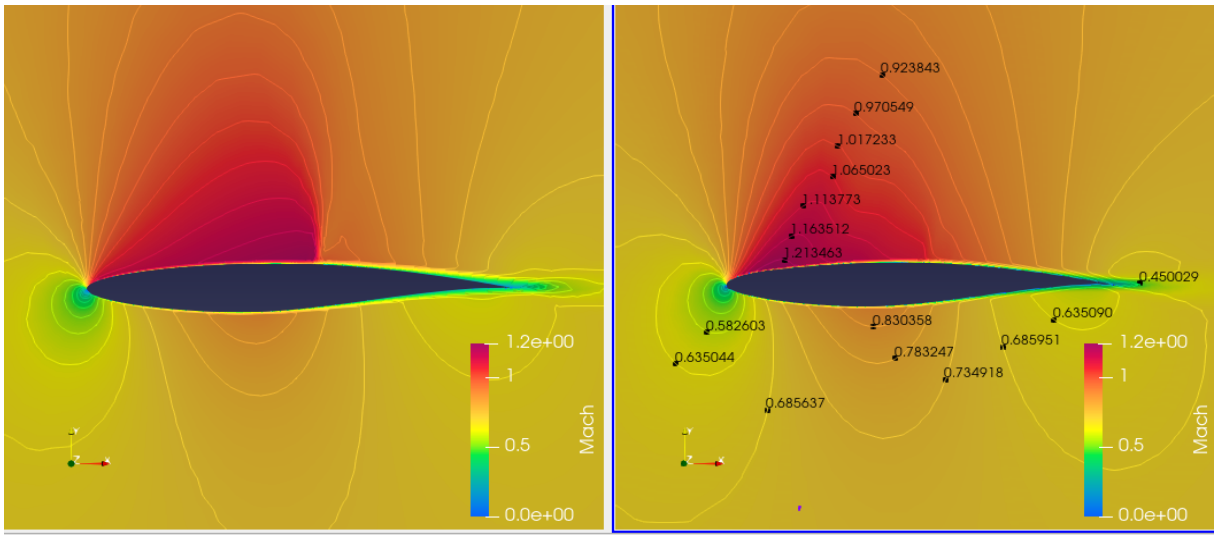

Figure 5.7: Mach distribution for the Initial vs. Optimised aerofoils.

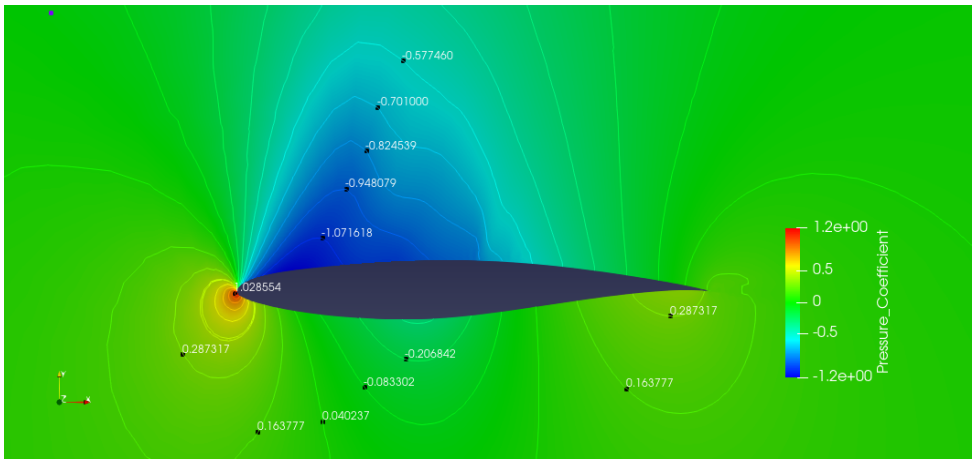

Figure 5.8: Pressure coefficient field surrounding the aerofoil for the drag-optimised case.

The objective function in this new test case is not the same as in the original one. Before, it was the *lift-to-drag* ratio while in this case is the *drag coefficient* at a constant lift. Then, a new sensitivity analysis is presented in Figures (5.9) and (5.10):

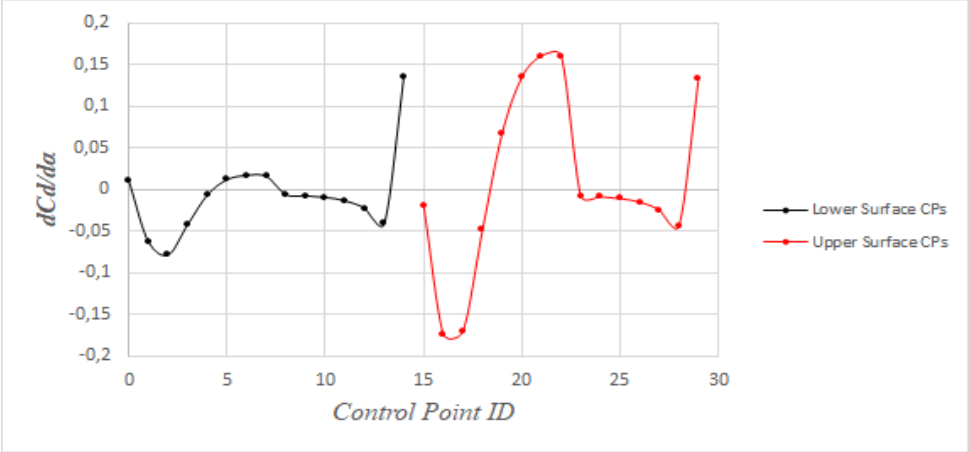

Figure 5.9: Sensitivity behaviour for the *drag* coefficient for each control point.

It is important to point out that: (1) the magnitude of the sensitivities is now different than in the previous case (see Figure (3.9)) due to the new objective function; (2) the regions which present higher sensitivities to the objective function are now wider, especially in the upper surface where the shock occurs. The wing-box area still has a significant responsibility for the drag generation, specially at the upper surface where the shock-wave appears but it is not an option to modify.

As well as in the lift-to-drag sensitivity analysis, the trailing edge seems to be responsible for a noticeable part of the produced drag and, by looking at the general shape of the aerofoil (Figure (3.1)), it should be due to the change given in pressure values when the upper and lower flows converge in that area. Then, this aerofoil region is expected to be changed by the optimisation algorithm.

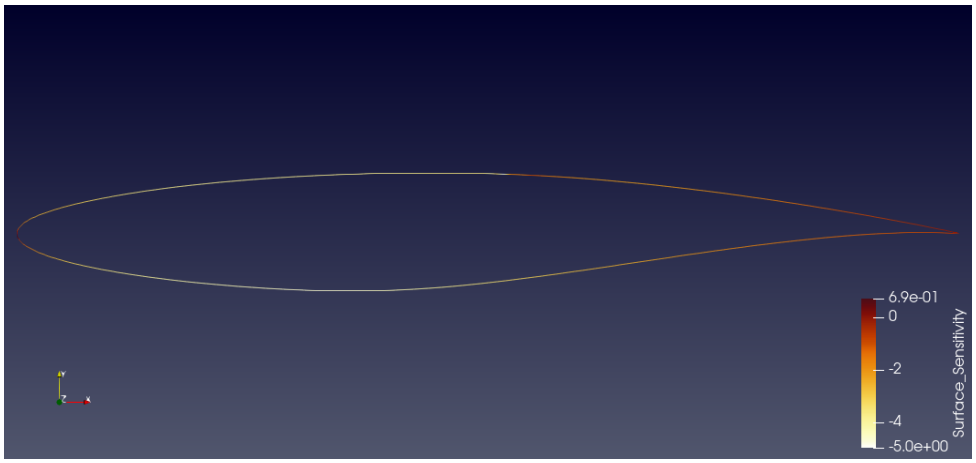

Figure 5.10: Sensitivity for the C_d along the surface of the aerofoil.

In order to see more drastic changes in the geometry, another study is going to be carried out. For instance, the ninth case from [65] with the correction stated in [75]: angle of attack is increased from $2.31°$ to $2.79°$; and the Mach number changes to $M = 0.730$. Moreover, drag minimisation is set objective, while maintaining lift fixed.

Shape optimisation for $M = 0.730$ and $\alpha = 2.79°$

On one hand, in Table 5.2 it is possible to appreciate a **29.04%** reduction of the drag coefficient, higher than the previous case. On the other hand, the geometric changes in the leading edge, Figure (5.12a) in blue, increased while keeping the conditioning of the shockwave's occurance by lowering the speed in that sub-region. In the trailing edge, Figure (5.12b), an analog change from Figure (5.5b) is made. Moreover, one can see that the solution has converged after 63 iterations in Figure (5.11)

Table 5.2: Aerodynamic coefficients for the second case optimised aerofoil's shape.

Shape	***Cl***	***Cd* counts**
Original	0.803	183.62
Optimised	0.803	130.29

The reason behind this higher reduction in the drag coefficient comes from its dependence with the angle of attack and the increase of the flight condition speed. Therefore, so as to soften the interaction between the aerofoil's geometry and the airflow, a re-adjustment of the initial contact conditions in the leading edge is done by the optimisation algorithm, clearly seen in Figure (5.12a).

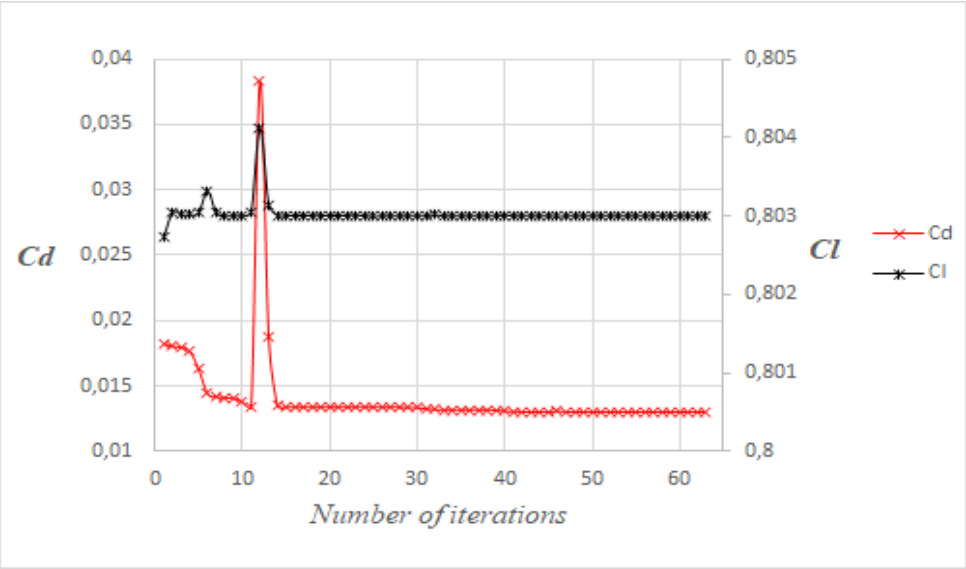

Figure 5.11: *Cl* and *Cd* variations along the shape optimization process for $\alpha = 2.79°$

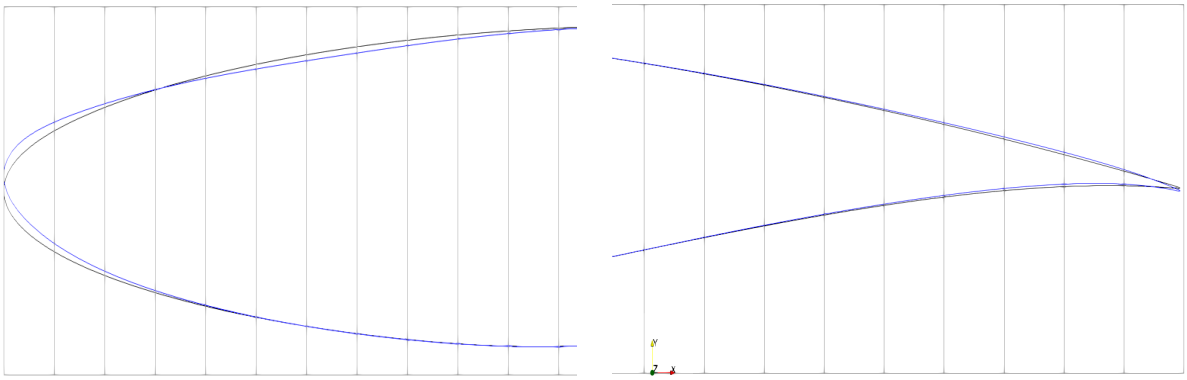

(a) Second case shape modification at the leading edge. (b) Second case shape modification at the trailing edge.

Figure 5.12: Shape modifications applied for the second case in the original RAE 2822 aerofoil.

Regarding the pressure coefficient distribution, Figure (5.13), along the aerofoil, there is a higher peak of suction closer to the leading edge than in Figure (5.6) and the position of the shockwave has not been practically modified, although softened. That decrease in pressure close to the leading edge can be understood by looking at Figure (5.12a) as the geometry modification leads to a higher pressure gradient. As well as in the general case, the greater magnitude of the modifications of the geometry is in the order of $0.5\%c$ (if the chord was defined as 1 meter, the deformation would be 5 *mm*) thus is not easily noticed.

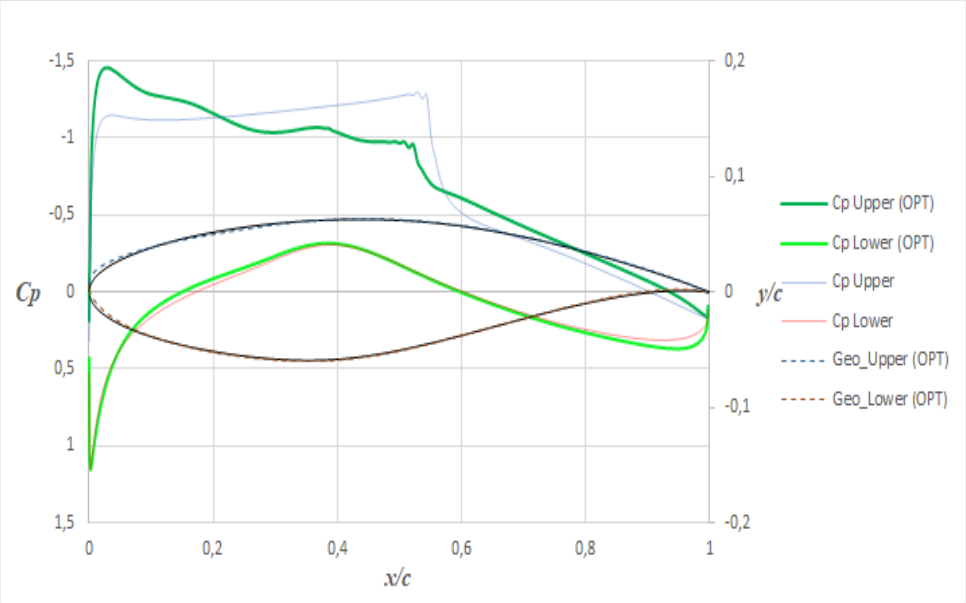

Figure 5.13: New pressure coefficient distribution comparison for the $\alpha = 2.79°$ case.

The new flow distribution along the aerofoil in the domain is shown in Figures (5.14) and (5.15) in terms of Mach and pressure coefficient distribution, respectively. Note the higher suction phenomena happening at the upper surface close to the leading edge and how the shockwave is softer than in the previous cases.

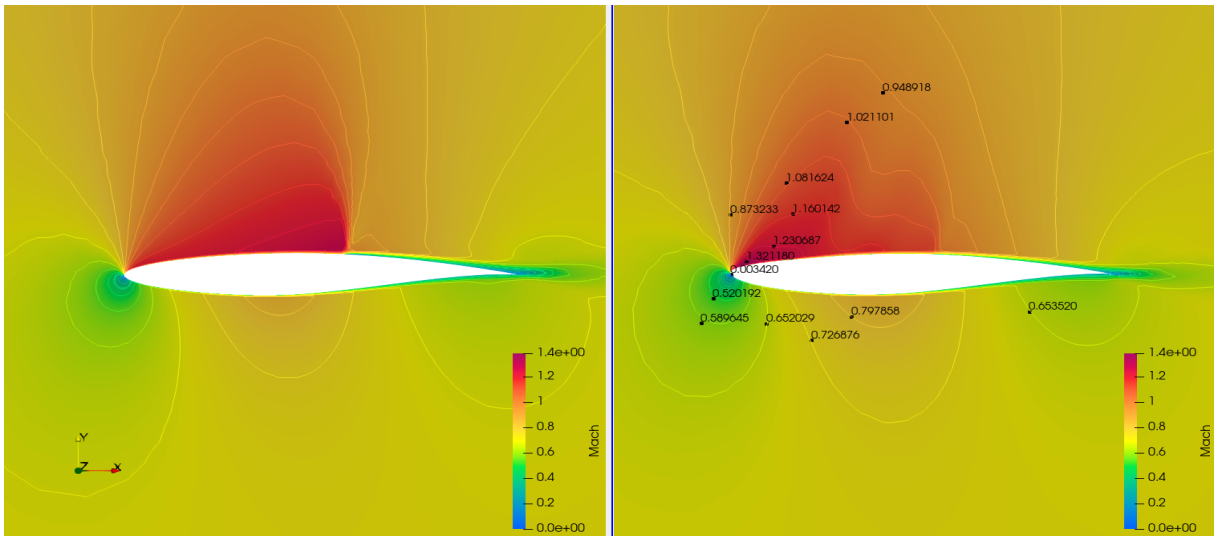

Figure 5.14: Mach distribution for the Initial vs. Optimised aerofoils.

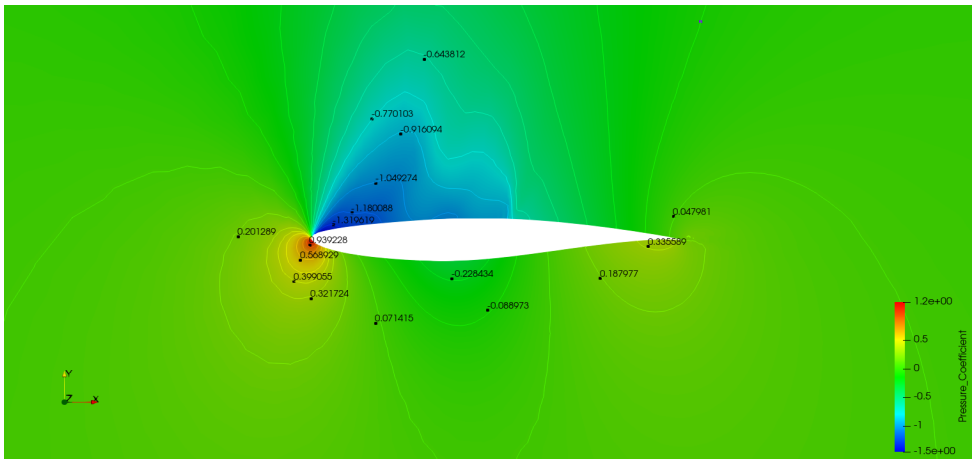

Figure 5.15: Pressure coefficients field surrounding the aerofoil for the drag-optimised case.

Regarding the behaviour of the CP towards the sensitivity analysis, for a higher angle of attack, the sensitivity has changed by terms of the maximum magnitude and introduced new sub-regions with higher influence, meaning that there is more availability to optimise the aerofoil. The results shown in Figure (5.16) follow the same tendency as in the work done by *Economon et al.* [16] for the same aerofoil and flow conditions. However, keep in mind that in this section of the thesis, not all the aerofoil's geometry has been discretised with the control points since the wing-box area is fixed.

Note that the upper surface has a major influence inside the optimisation process, which was expected as the shockwave carries along with it a key drag creation impact, and, moreover, a peak of this sensitivity is found between CPs 17 and 22 (Figure (3.8)), just before the wing-box area constraint and the flow discontinuity occurance . Furthermore, the leading edge in both upper and lower surfaces also has its influence, but mostly related to the constant lift constraint even though a benefit by means of drag reduction is also going to be obtained as the optimisation focuses in this specific element.

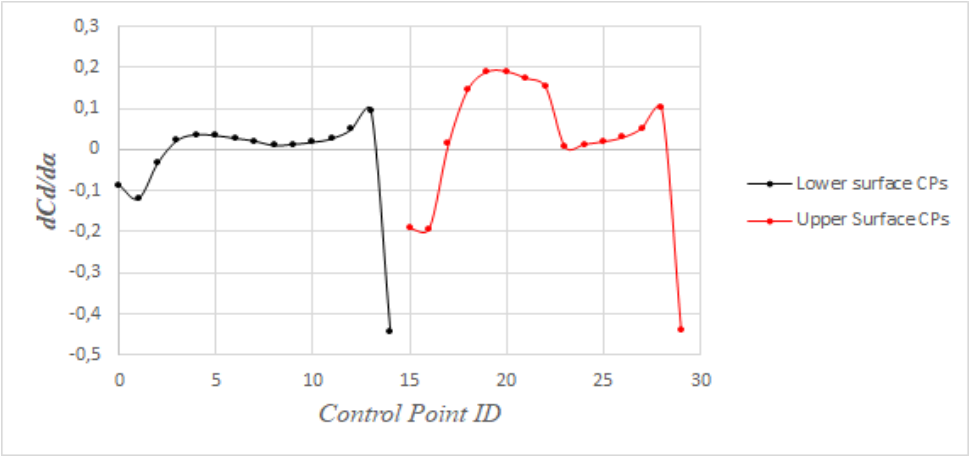

Figure 5.16: Sensitivity behaviour for the *drag* coefficient for each control point.

Keep in mind that the aircraft weight reduces during flight, thus lift coefficient is also reduced during flight (unless a constant CL strategy is fixed by increasing the angle of attack). This makes an ideal case for morphing the shape of the aerofoil during the flight to seek for the minimum drag possible throughout the entire cruise segment (which can be extended to the remainder of the mission segments). In addition, the reader has had the chance to see how influential are the small-scale deformations in the aerodynamic behaviour, which, by using computational methods, an unique efficient solution may be found while, contrary for wind-tunnel testing, it is not unreachable but extremely time and resources consuming.

Moving forward in the thesis development and as an introductory description, the behaviour of the structure then has a key influence in the aerodynamic behaviour. If the deformations suffered by the material which made the wing shape are found inside the interval specified at the optimisations shown in this section, none of the improvements provided by the process are going to be useful, thus, for the material selection and structural conduct, it is essential to consider and involve the previous study in their constraints so as to couple two designs in an efficient way.

Chapter 6

Structural results

The next field of study for the thesis is the structural point of view of the aerofoil. In this section, the geometry is going to be analysed so as to check its compliance with the loads for which it is subjected to. To do so, and by considering initially an elastic behaviour, the stress distribution and the general displacements are going to be studied and, afterwards, the topology optimisation procedure is going to be applied and studied to the base cases.

6.1 Results

Once the methodology for the structural analysis has been defined, by recalling the information described in chapter 4, the stresses and the displacements can be plotted and commented. To begin with, and in order to group the plain main two-axial stresses so as to check the elastic behaviour of the component, it has been decided to plot the von Mises stresses, Figure (6.1). As the case follows a two-dimensional reference, only three components of the Cauchy stress tensor are not null, being them σ_x, σ_y and τ_{xy}. Then, to obtain the von Mises stress, the principal directional stresses are used:

$$\sigma_{VM} = \sqrt{\frac{(\sigma_1 - \sigma_2)^2 + (\sigma_2 - \sigma_3)^2 + (\sigma_3 - \sigma_1)^2}{2}} \tag{6.1}$$

where:

$$\begin{cases} \sigma_1 = \dfrac{\sigma_x + \sigma_y + \sqrt{(\sigma_x - \sigma_y)^2 + 4\tau_{xy}^2}}{2} \\ \sigma_2 = 0 \\ \sigma_3 = \dfrac{\sigma_x + \sigma_y - \sqrt{(\sigma_x - \sigma_y)^2 + 4\tau_{xy}^2}}{2} \end{cases} \tag{6.2}$$

obtaining afterwards the 2D definition of the von Mises general stress:

$$\sigma_{VM} = \sqrt{\sigma_x^2 - \sigma_x \sigma_y + \sigma_y^2 + 3\tau_{xy}^2} \tag{6.3}$$

Note that the most demanding phenomena occurs around the leading edge wing-box boundary, specially at the corners of it because of the stress-concentration factor (that is why the wing-box corners have been rounded), not because of the shockwave appearance nor the pressure distribution itself. When embedding an object inside a flow, the first intrusion which will be the stagnation point, suffers from a higher pressure value on its boundary because of the flow's speed reduction. Therefore, at the leading part of the aerofoil there is a higher structural demand due to the pressure's distribution. Moreover, the obtained magnitudes are lower than the elastic failure parameters of the selected material (Aluminum allow 6061 $\sigma_{yield} = 276MPa$). Thus this distribution can deal perfectly with the flight conditions established.

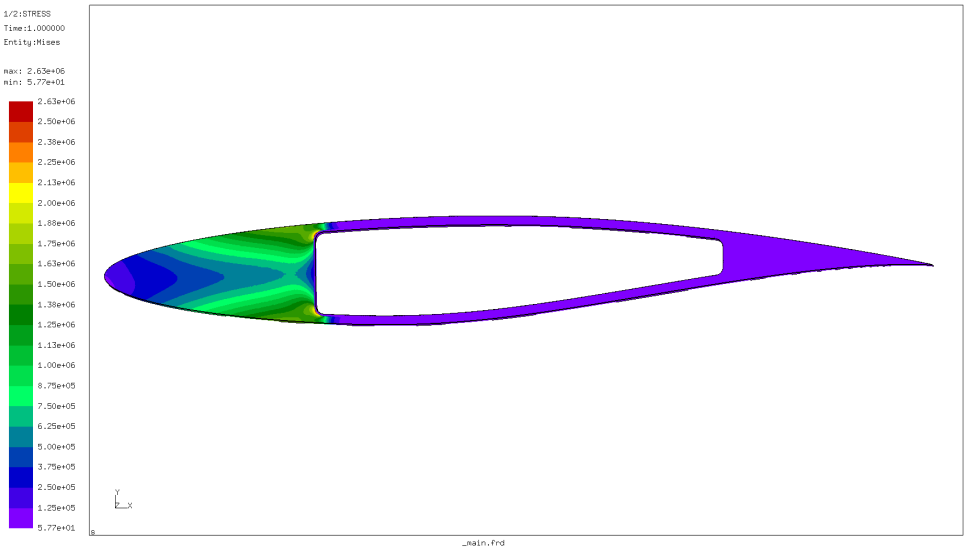

Figure 6.1: Von Mises distribution for the RAE 2822 case study.

Differently for the displacements in Figure (6.2), the maximum value is found at the leading edge of the aerofoil, which is expected as it is the most further way from the non-displacement constraint applied at the wing-box, analog to the standard case of a cantilever beam. Nevertheless, the magnitude of the displacement is small ($\sim 10\mu c$) and will not have a direct influence in the aerodynamic behaviour.

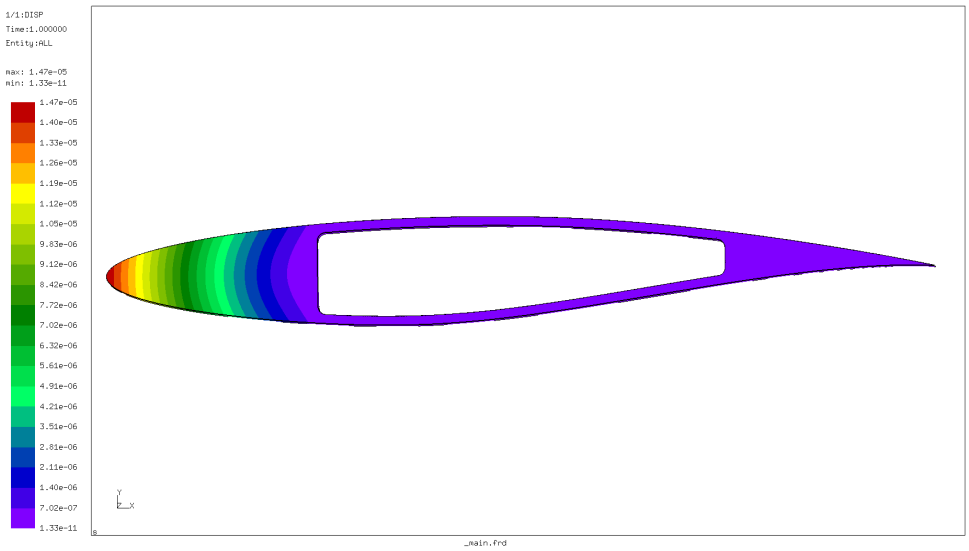

Figure 6.2: Displacements for the RAE 2822 case study.

From this point, and by checking the stress distribution inside the aerofoil plus the micro-displacements generated, one can guess that there is unnecessary material in this model. This is why a topology optimisation is actually applied to just use the optimal and necessary quantity of material in order to make the design efficient. The goal is to reduce weight such that few fuel is consumed, thus being more efficient from the operational/performance point of view.

In this case study, as one of the most critical parameters in the aeronautical field is the weight of the component, the structural safety of the aerofoil is being modified and analysed following a minimising procedure for the weight of the aerofoil. For instance, the following descriptions and results are directed towards the maximisation of the structural stiffness-to-weight ratio, also known as the minimisation of the compliance-to-weight of the object. Therefore, the expected results will show structural voids in different inner areas of the aerofoil which do not have a noticeable influence on the stiffness of the geometry, meaning that they can be neglected as the rest of the structure can absorb perfectly the respective loads.

Moreover, the topology study was carried out using the same Aluminum-6061 material stated previously in Table 4.1 as it has a wider interval of safety rather than other materials named in section 4. In Figure (6.3) the path followed by the solver in order to reach the specific weight goals of the optimisation is shown.

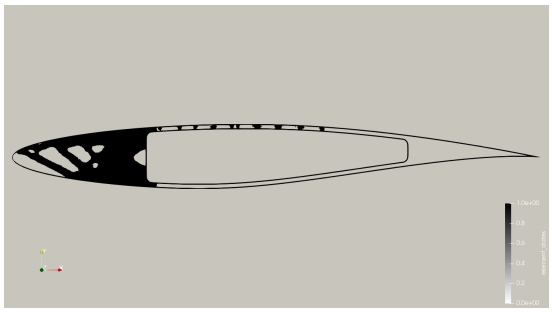

(a) Weight reduction target: 50%.

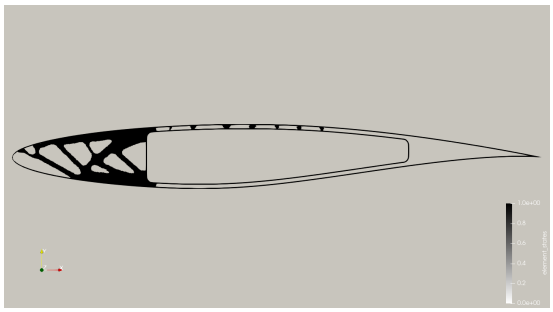

(b) Weight reduction target: 35%.

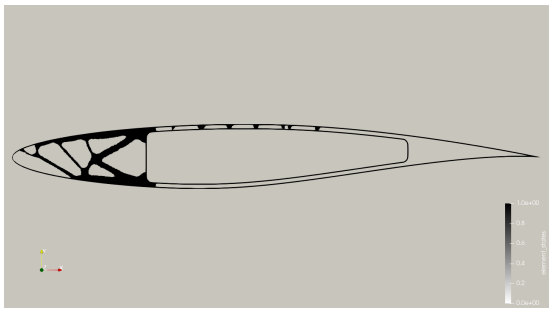

(c) Weight reduction target: 25%.

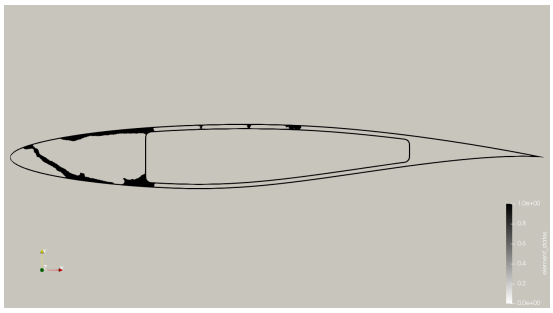

(d) Weight reduction target: 10%.

Figure 6.3: Topology optimisation procedure development for the case study.

Note that the wing-box constraint and the skin have been untouched by the solver and that the primordial structure lies just below the skin of the aerofoil, then, to avoid large deformations due to pressure, inner truss structures are required. Given the chosen mesh definition, the optimised structure is neither smooth nor easy to manufacture, thus a post-processing is required. On the upper side of the wing-box surface, a more reinforced structure is needed following the stress distribution showed in Figure (6.1), which could be solved by stringers. Even though the stresses are similar in the leading edge, connected bars have been understood to be the most optimal element to withstand the loads transferred by the skin.

Apart from that, the trailing edge inner areas are empty. It does not mean that it should be designed in such a way but any structure in that sub-region is negligible towards the final behaviour thus avoidable. Nevertheless, this void should be filled with a lighter material or other attachments so as to maintain the aerodynamic shape of the aerofoil; then, a secondary material could carry that function.

Regarding the optimised geometries given by the solver, the 25% weight constraint looks like an ideal shape for the design as, it is noticeably efficient in terms of mass reduction but not as simple and fragile-looking as the 10% case. To demonstrate its proper design, the following set, shown in Figures (6.4) and (6.5), analyses the failure index of the structure and the von Mises stress distribution. Note how, for the highest weight reduction target, the *FI* is higher and some parts of the resulting structure suffer from high demanding stresses, specially at the upper-left part of the aerofoil. In order to avoid ruptures or unexpected failures, it is better to reinforce the general layout even though the final weight is higher as one can observe in the result shown in Figure (6.5b).

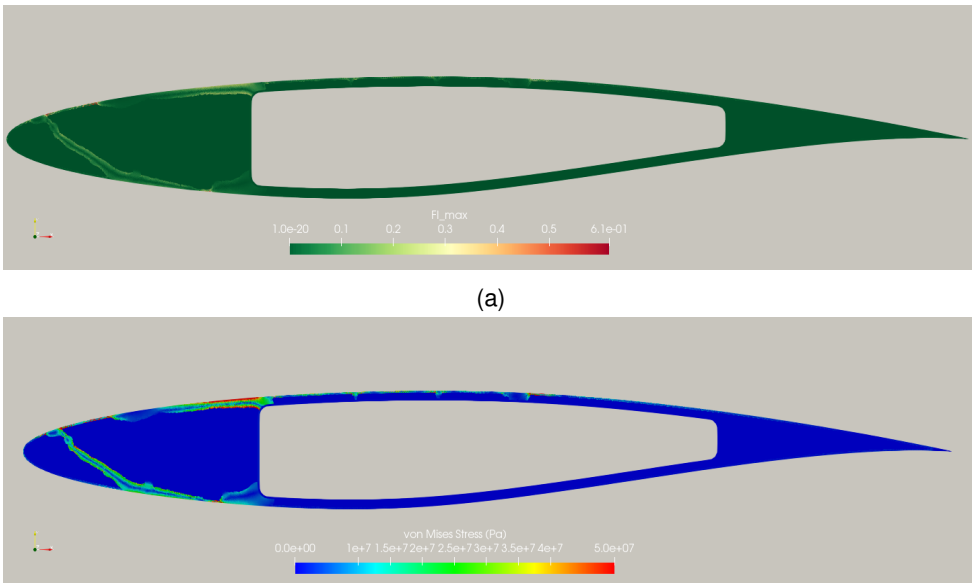

(a)

(b)

Figure 6.4: (a) Failure index distribution and (b) Von Mises stress distribution of the test case for a 10% mass reduction.

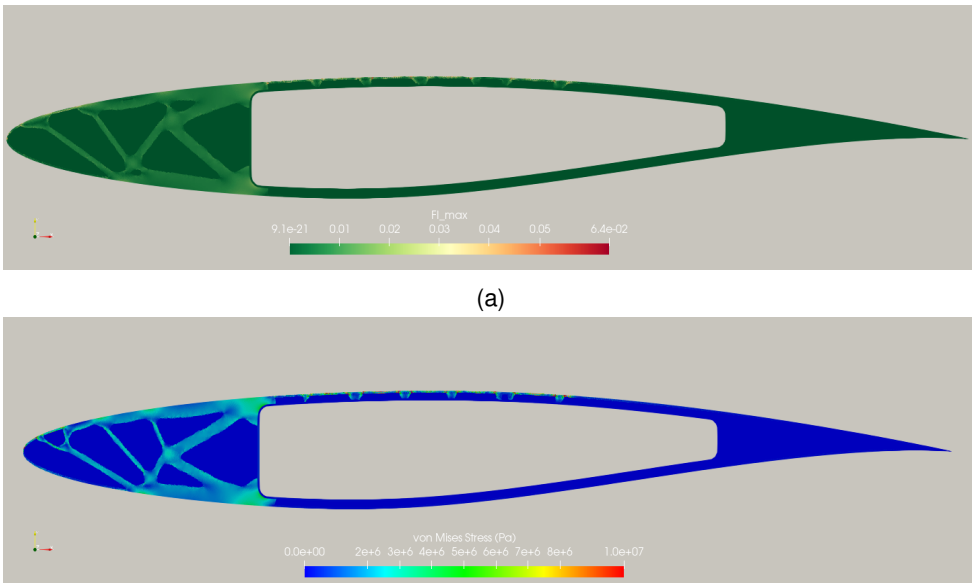

(a)

(b)

Figure 6.5: (a) Failure index distribution and (b) Von Mises stress distribution of the test case for a 25% mass reduction.

Chapter 7

Coupling between the optimised designs

In order for the approach to be completely efficient and useful in both of the studied fields, one should consider its interrelation. This means that one optimised result may not be compliant with the other optimisation target. For instance, an aerodynamically shape modification may lead to weak regions for the structure to withstand the loads of the flight regime, thus a common analysis is aimed so as to check the safety envelope. From this point, two methodologies arise.

On one hand there is what is known to be a sequential approach, for which, after the first optimisation procedure has been done for one of the targets, a second optimisation is carried out for a different goal. On the other hand and, in order for the final result to be more accurate, the optimisation procedure should be coupled, meaning that both techniques should be ran at the same time. In other words, when an optimised aerodynamic case is being done, another line of the code must check the compliance of the element *per iteration*, as any modification in the structure of the aerofoil is going to modify the flow's behaviour. Therefore, this procedure must be followed if the conditions at which the aerofoil is under will imply big sensitivities in both fields, such as in cases of aeroelasticity or thin surfaces.

In terms of the purpose of the work and, due to the simplicity the sequential approach offers plus the improvements it gives for both of the analysed fields, this process provides insightful information and results to be efficient, knowing that a coupled strategy would represent a more realistic case study and provide better accuracy, but at the cost of computational resources and complexity.

In the case of the thesis, a drag minimisation has been done using the *SU2* software followed by a topology optimisation carried out by means of an open-source script provided by *F. Löffelmann* in [28]. Therefore, initially the aerodynamics subject is going to be developed and followed by the structural one, which both include the respective optimisation procedures. Once the optimal is found by the solver, the output can be analysed. In Figure (7.1) there is a graphical representation of the followed methodology.

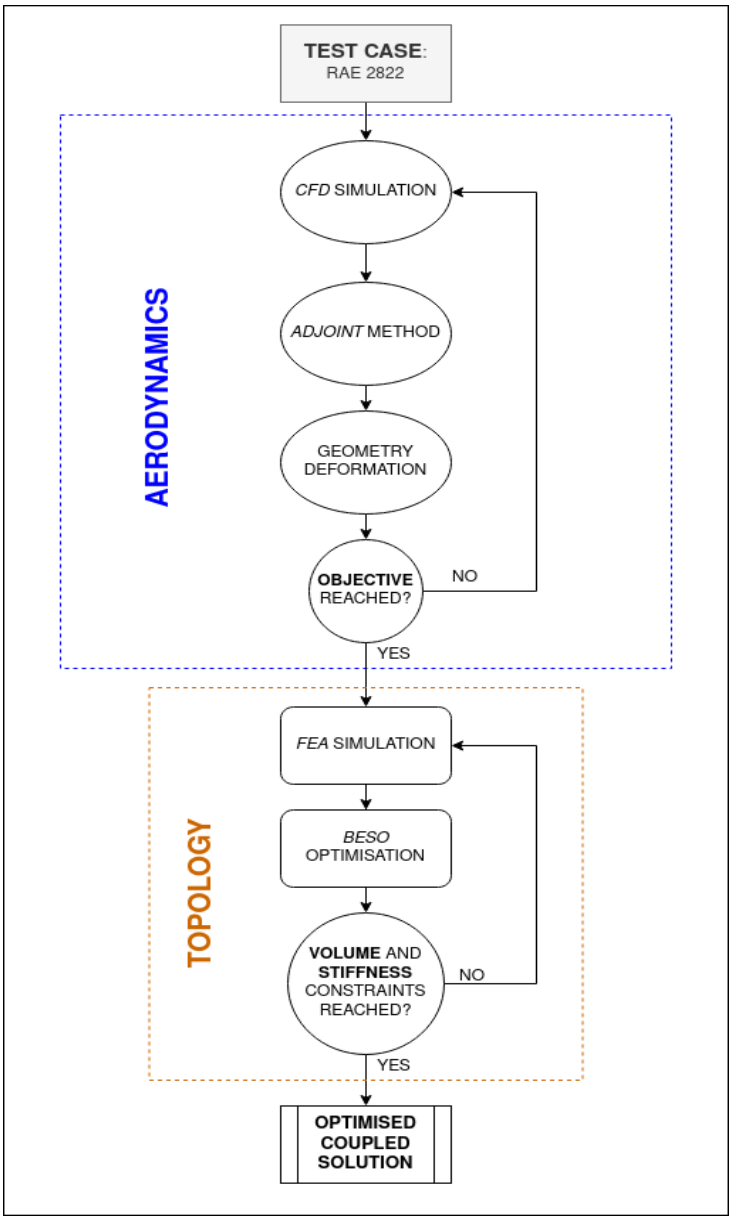

Figure 7.1: Sequential approach algorithm followed in this work.

Sequential approach: RAE 2822, M = 0.729 and $\mathbf{alpha} = 2.31^{\circ}$

Following the optimisation done in section 5.2 for the aerodynamic shape, the new load distribution has been applied to the optimised shape in Figure (7.2). Note that, compared to the general case, Figure (4.3), the upper loads adopted a more continuous distribution, downloading the magnitude at the leading edge and softening the shock. It couples then with the description provided in Figure (5.6) for the optimised pressure coefficient distribution regarding the new pressure gradients and their meaning.

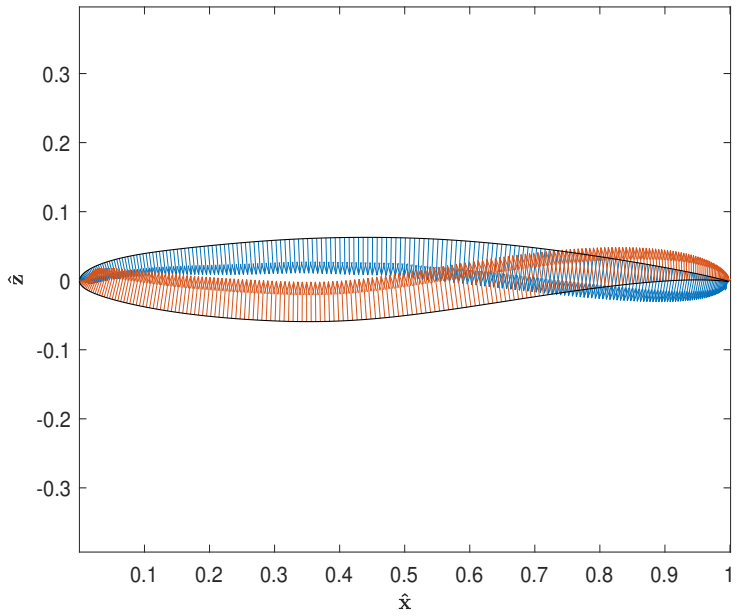

Figure 7.2: Pressure loads for the RAE 2822 first optimisation of the case study.

By checking the new-state stress distribution and displacements in Figures (7.3) and (7.4), the general view of the results do not seem analog to the ones provided above in the general case study basically because the modifications given by the aerodynamic-optimiser were quite specific. Moreover, the magnitudes have changed as it is a new case study.

Regarding the von Mises stresses, the maximum value has substantially decreased in 97%, from 2.63 MPa to 74.8 kPa. This modification should be a reference for future work as, because of the study settings, the sequential approach has delivered an interesting final output for the coupling step.

Note that, the stress distribution has moved towards the trailing edge, where it has the lowest material density. If Figure (6.1) and (7.3) are compared, the pressure loads are softened all along the aerofoil's surface driving towards a less demanded structural state.

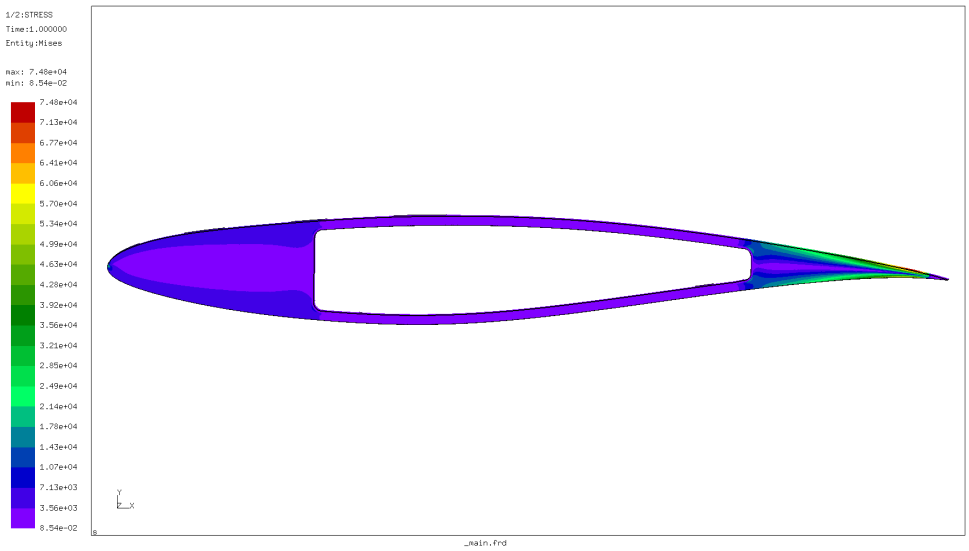

Figure 7.3: Von Mises distribution for the first optimisation done to the RAE 2822 case study for the aerofoil.

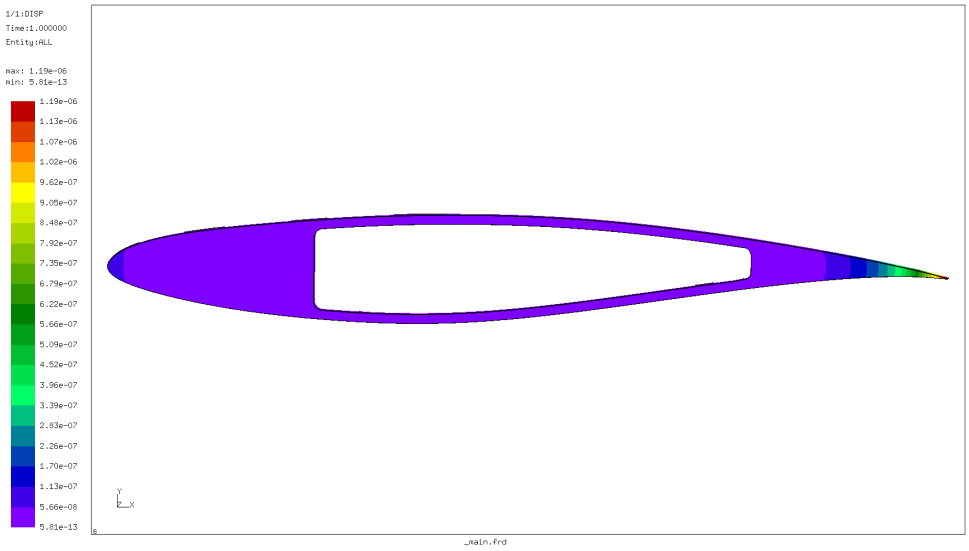

Figure 7.4: Displacements for the first optimisation done to the RAE 2822 case study for the aerofoil.

The higher stresses are located at the thinner part of the aerofoil. Those higher stresses are two orders of magnitude lower than in the non-optimised aerodynamic case, thus, no large deformations are expected. Actually, the maximum displacement magnitude in Figure (7.4) for the optimised shape is $\sim 92\%$ lower. It can be said that the aerodynamic optimisation has provided a far more relaxed state to the aerofoil and that the coupling of optimisations have reached an ideal as, both have been improved without entering in conflict with each other.

Following the thesis' structure, the topology optimisation for the latest case comes now presented. By using the stated parameters regarding the sensitivity filter and mass ratios ($r_{fil} = 0.01c$, $\nabla m = -3\%$), the

different weight constraint output solutions are provided in Figure (7.5).

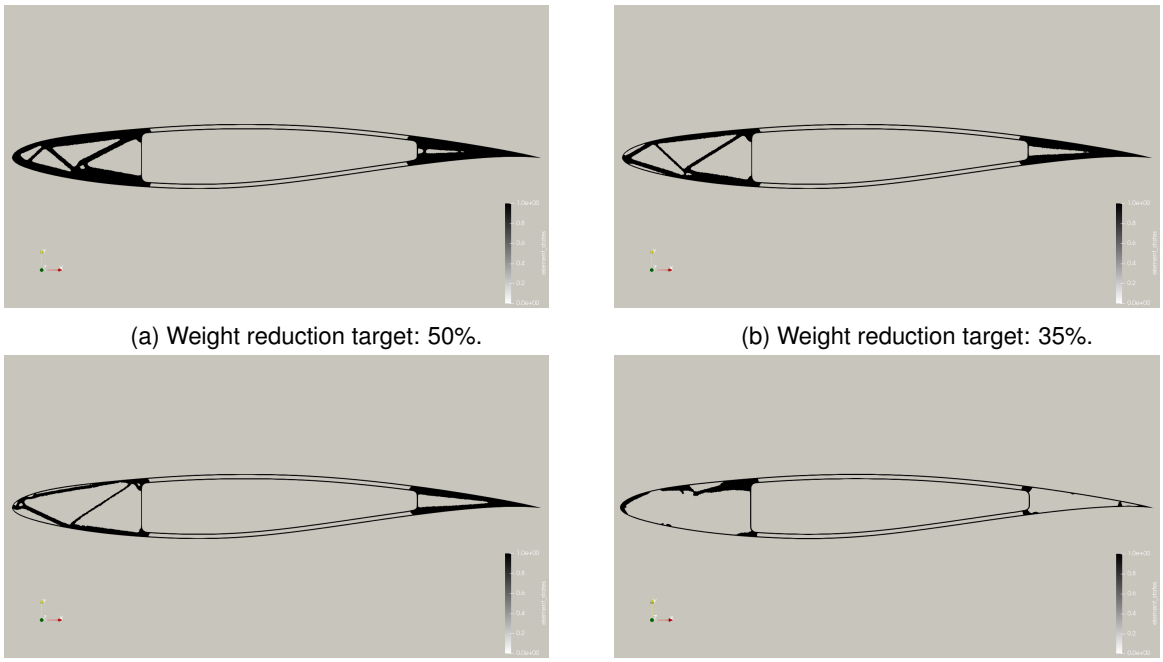

(a) Weight reduction target: 50%.

(b) Weight reduction target: 35%.

(c) Weight reduction target: 25%.

(d) Weight reduction target: 10%.

Figure 7.5: Topology optimisation procedure development for the optimisation of the case study.

In this latter case, there is one main difference in the topology between the general case and the aerodynamically optimised one. In the latter, no reinforcement elements are required inside the region between the upper surface and the wing-box area. Its main function was to provide stiffness to avoid high deformations and failures because of the shockwave apparition, whose pressure variation loads should be taken into consideration and, as the geometry has been previously optimised by providing a softer flow transition result, their presence may be neglected.

As the studied case suffers now from a higher loading state in the trailing edge, that area has had to be reinforced while the opposite occurs at the front of the aerofoil. Therefore, at the trailing edge, the skin is connected to the wing-box corners and a skin-reinforcement is required

Moreover, the 10% weight reduction target provides a weak solution as it seems to be 'unfinished'. Therefore, as in chapter 6, the ideal optimised layout is considered to be the one that has the 25% weight constraint, thus the following figures refer to the failure index and von Mises distribution of that specified case.

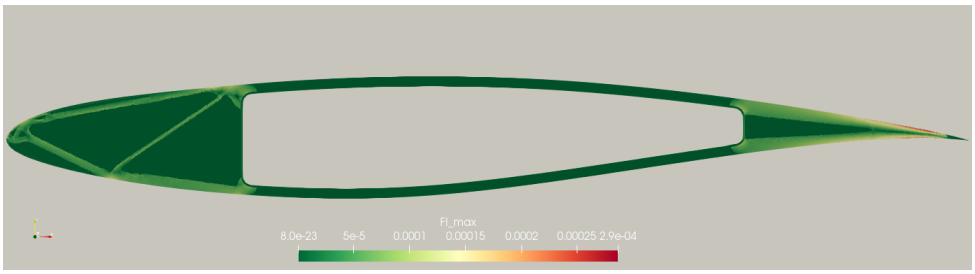

(a)

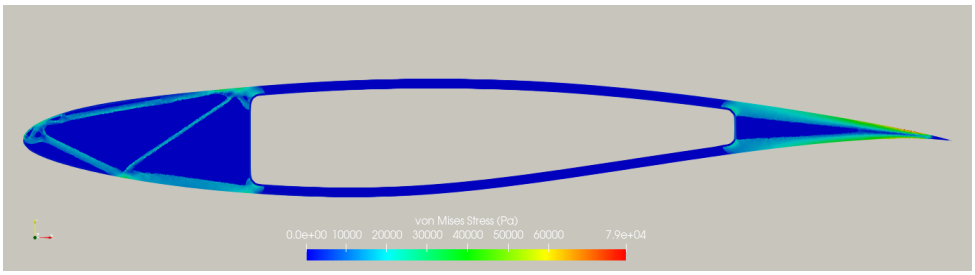

(b)

Figure 7.6: (a) Failure index distribution and (b) Von Mises stress distribution for the optimisation of the test case for a 25% mass reduction.

It is worth to point out how the *FI* of Figure (7.6a) is two orders of magnitude lower ($\sigma_{yield}^{a6061T} = 276$ MPa) than in Figure (6.5a), meaning that, from a first approach, the structure can perfectly withstand the loading state, considering as well an interval of more demanding situations. In terms of stresses, the structure finds itself in a more relaxed situation, not only because what was stated when describing Figure (7.3) but also because the absorption of loads due to the appearance of material in the leading edge region. Apart from this latest statement, note how the inner stresses have a higher value than in the completely material-filled aerofoil (but in the same magnitude's interval), which makes sense as the main purpose of the topology optimisation is to redistribute the loads towards specific regions of the geometry while removing the unnecessary ones.

Sequential approach: RAE 2822, M = 0.730 and $\mathbf{alpha} = 2.79°$

Aiming at higher modifications in the geometry, a second case study was selected, in which the flow conditions were modified. The reason behind this new strategy is to follow the modifications in the flow, structural behaviour and, at the end, the topology optimisation results in order to see if, for different setups, there were drastic changes or similar ones. Depending on the conclusion, a general aerodynamic and topology optimised aerofoil geometry could be provided for a certain flight regimes making it more available. Therefore, as in the development followed above, a comparison of the loads obtained by the nodal pressures for the general case and the optimised one is provided in Figure (7.7) and, afterwards, its structural analysis is presented.

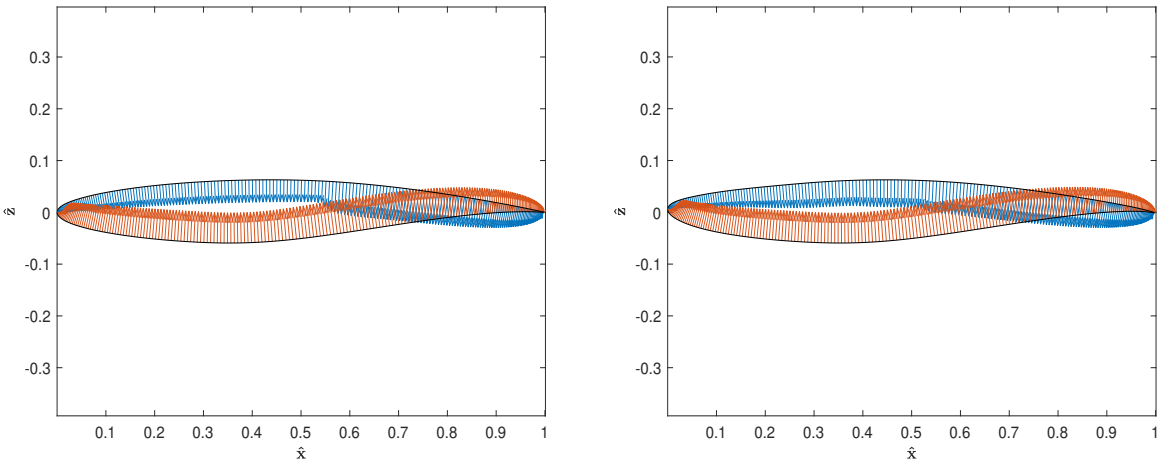

(a) (b)

Figure 7.7: Pressure loads distributions. (a) General case. (b) Optimised case.

As the initial setup is different from the general case study of the thesis, the expected behaviour should be a variant. The fact of having a higher angle of attack has changed the pressure distribution along the aerofoil. Check visually in Figures (6.1) and (7.8) how similar are the loads applied in the leading edge, where the primordial effects should be present because of the change of the angle of attack.

From this point and, as it can be seen in Figures (7.8) and (7.9), the most stress-demanded part of the aerofoil is close to the corner points at the wing-box closer to the leading edge, reaching again the magnitude of 10^6 Pa. Regarding the behaviour of the displacements, they have an analog distribution as in the previous case, being more noticeable in the leading edge.

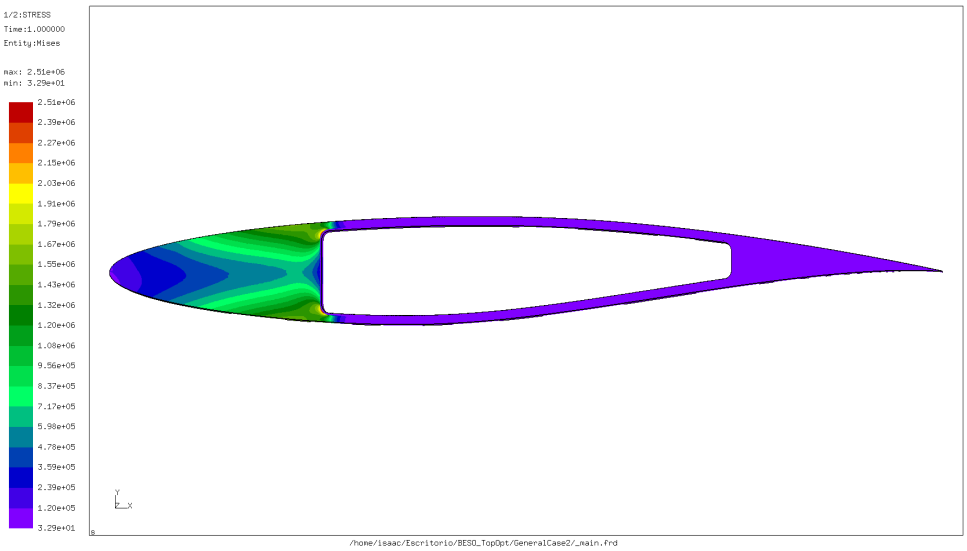

Figure 7.8: Von Mises distribution for the second RAE 2822 case study for the aerofoil.

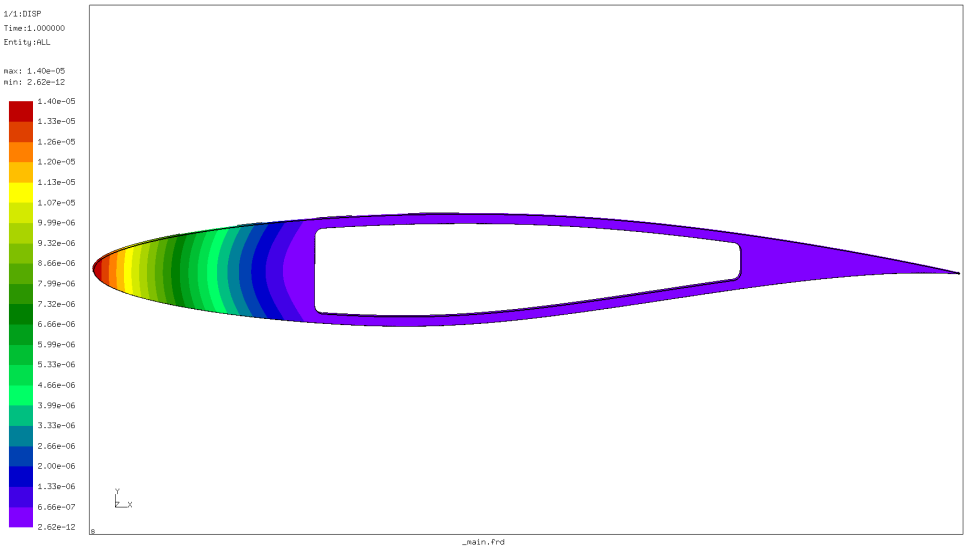

Figure 7.9: Displacements for the second RAE 2822 case study for the aerofoil.

Once the geometry has been optimised to reduce the produced drag at a constant lift value, a new loading state is produced (Figure (7.7b)), which again provides an unbalance between the two surfaces of the aerofoil. It can be checked in Figures (7.10) and (7.11), that the final state is totally optimised again in both fields of study, the fluid and solid mechanics. Regarding the stress distribution, it represents a 1.48% of the loading state for the initial case, reaching a maximum value of 37.2 KPa and a displacement of 0.403 μc. It is worth to note how very small changes in the surface of the aerofoil when optimising the geometry have a great influence on the stress distribution.

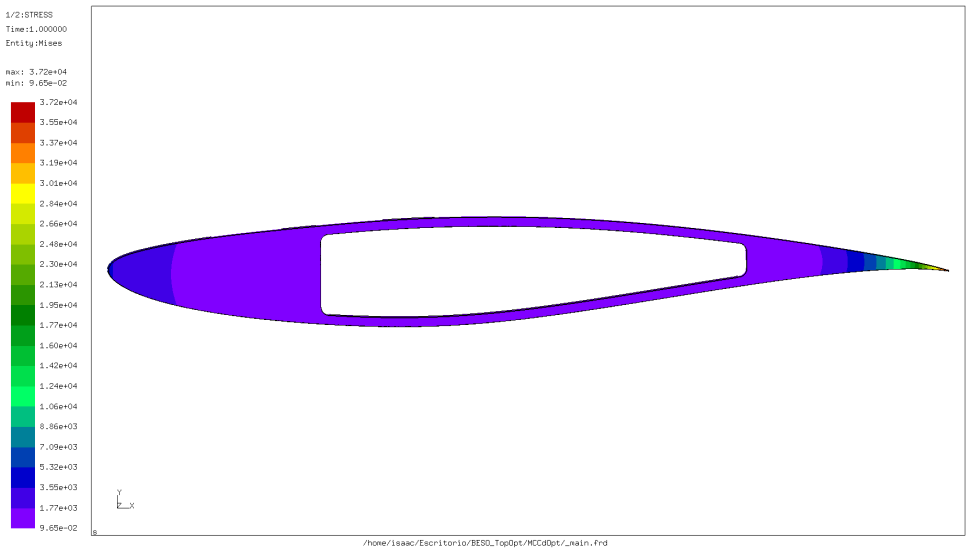

Figure 7.10: Von Mises distribution for the second optimisation done to the RAE 2822 case study for the aerofoil.

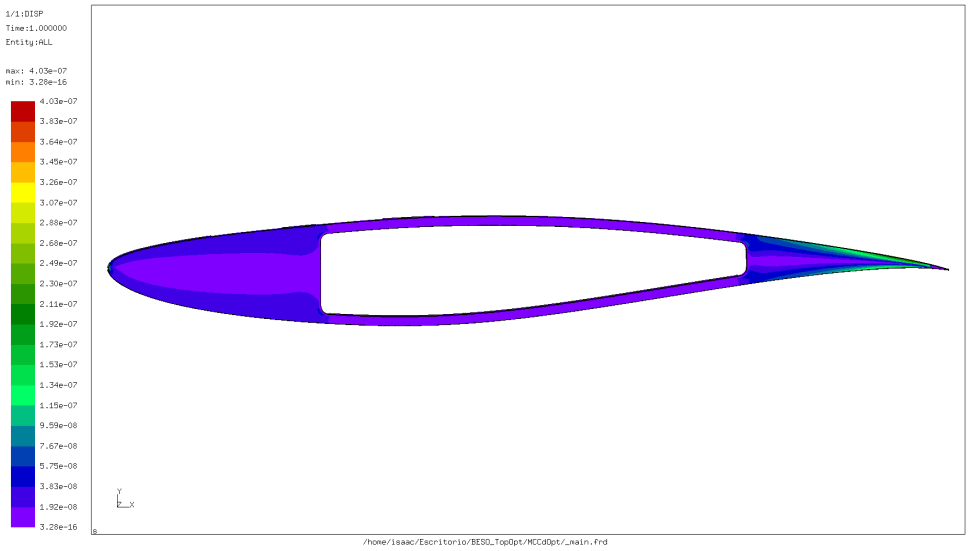

Figure 7.11: Displacements for the second optimisation done to the RAE 2822 case study for the aerofoil.

Once the aerodynamic optimisation provides its output geometry, the topology optimisation follows. Therefore, new states for the weight reductions (50%, 35%, 25% and 10%) are given in Figure (7.12).

First of all, note the difference the distribution has in the leading edge region compared to the previous optimisation case shown in Figure (7.5). In this actual case, the geometry has been modified in a more neutral way, balancing the upper and lower surfaces, while in the previous, the geometry is yet influenced by an uneven load distribution due to the specific angle of attack of the study characteristics. Regarding the optimal reduction target, following the same explanation for the optimisation of the general case study, the 25% target seems to be adequate. Therefore, the stress and failure index studies will be based

in that specific geometry which its main purpose is to demonstrate the feasibility of the topologically optimised structures.

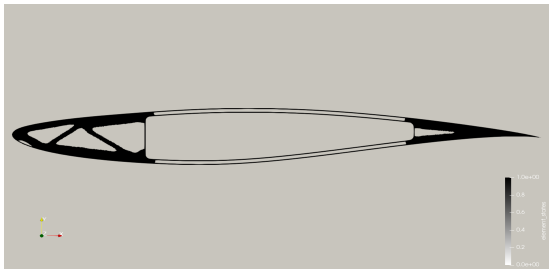

(a) Weight reduction target: 50%.

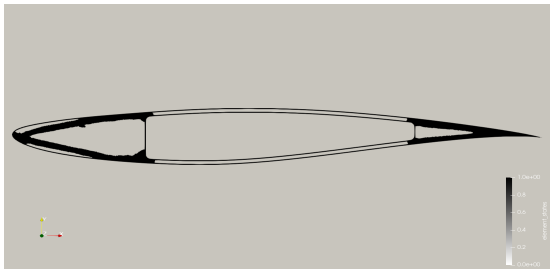

(b) Weight reduction target: 35%.

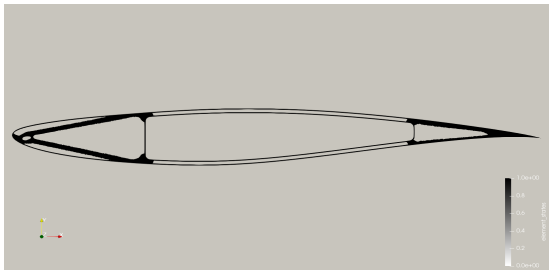

(c) Weight reduction target: 25%.

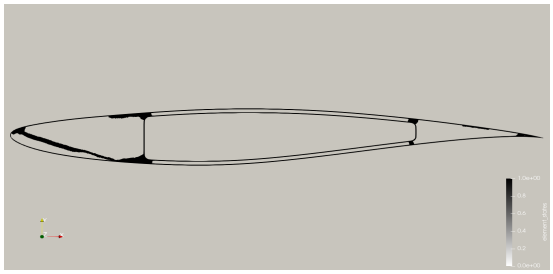

(d) Weight reduction target: 10%.

Figure 7.12: Topology optimisation procedure development for the optimisation of the second case study.

Again and, as a consequence of the aerodynamic optimisation of the loads dependency from the shock-wave, structural reinforcements are not strictly required for the main structure in between the wing-box and the upper surface of the aerofoil and only by holding and coupling the corners of the wing-box with the aerofoil's skin, a resistant component is obtained, with the capability to withstand higher loads. From this point, in Figure (7.13), the analog plots regarding the failure tendency and stresses are presented.

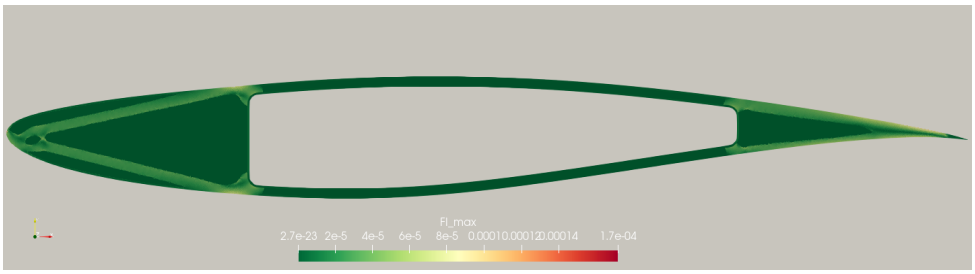

(a)

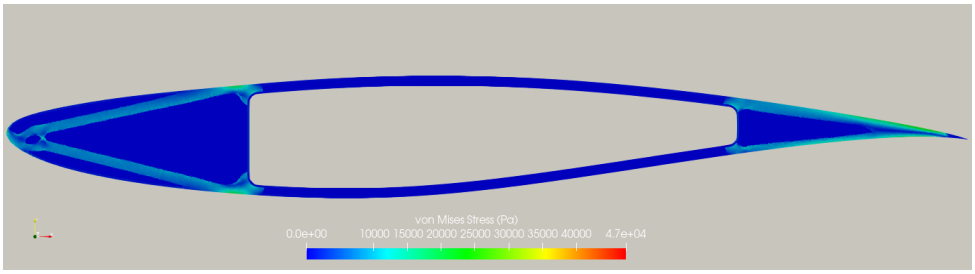

(b)

Figure 7.13: (a) Failure index distribution and (b) Von Mises stress distribution for the optimisation of the second test case for a 25% mass reduction.

By comparing Figure (7.10) and (7.13b), it is possible to note that the loading state has been increased again from the filled aerofoil as there is less material facing the stresses. Nevertheless, in this case where the highest stresses were found in the trailing edge, they have been reduced because of the use of two bars at the leading edge, which aim a more balanced distribution and gather part of the loading state of the geometry, while dealing perfectly with the transferred loads as the *FI* in Figure (7.13a) shows.

In conclusion, the main arguments to export from the study are: (i) the well-behaved output obtained by the sequential coupling; (ii) the noticeable influence a single parameter of the BESO method has in the final layout; (iii) and that, for 2D aerofoils only loaded by the aerodynamic loads, a high percentage of material removal can be obtained. Nevertheless, this study has been designed by a set of specific features that led to the final solutions shown. Therefore, a wider horizon of solutions may be found by other users by continuing or expanding the content shown in this thesis.

Chapter 8

Conclusions and Future Work

In this last chapter, the general and final conclusions reached along this study are drawn and presented, followed by recommendations and suggestions for future work.

8.1 Concluding remarks

This research aimed at coupling both aerodynamic and structural designs of aerofoils using efficient optimisation tools such as aerodynamic shape optimisation and topology optimisation. Firstly, based on the analysis carried out along the process to reach the stated target, it allowed to conclude that this field has capabilities to develop to highly-influential new designs, as it is built from a wide set of aspects and parameters which are able to propose new steps towards improvement. For instance, different optimisation setups can be chosen for both fields such as the mathematics behind the optimisation method and the inner parameters which define their computational implementation. Secondly, when defining a wing-box geometrical constraint, the optimisation algorithm is not allowed to change shape on that region, regardless of its potential to further improve the aerodynamic design. Another aspect to highlight are the results. Since the aerodynamic optimisation allowed for a pressure distribution that reduces the stress on the structure, a field coupled optimisation methodology was not used. Finally, it is important to point out the limits of the study, as a simplified option of the reality was used when using a bidimensional object without other restrictions which could be found inside the flight envelope, other wing-box constraints and the use of an empirical model for the fluid dynamics computation.

In terms of the aerodynamics, the study has shown that, for very small geometric modifications, noticeable changes in the behaviour were found. For instance, the shockwave was softened even for small shape changes of $0.1\%c$, leading to considerable drag reductions of 13.9% for $M = 0.729$ and $\alpha = 2.31°$ and 29.04% for $M = 0.730$ and $\alpha = 2.79°$. This phenomena, even though it came from the aerodynamics, could have had a direct influence on the general optimisation procedure since it has an impact on the structural behaviour in terms of stress and displacement. Nevertheless, the research has shown that, by

improving the aerodynamic behaviour of the aerofoil, the structural loading state is benefited. In terms of the von Mises stress distribution and displacements magnitude, it has decreased to a 3% reduction state and to a magnitude of two orders below the first study case respectively, which represent a magnitude of three orders fewer than the aerodynamic-born displacements; for the second test case, the von Mises maximum stress distribution decayed by 1.48% and three orders of magnitude for the displacements. This aftermath was expected as the total pressure was reduced from the aerodynamic optimised shapes.

The initial idea behind the scope of the thesis was a general optimisation coupling strategy, but the complexity it involved required a large amount of time and resources. Then, since the sequential approach represented a promising and a high degree of improvement for both studied engineering fields, the thesis path was reoriented towards the sequential perspective of the problem setup.

It can be concluded that the whole filled aerofoil is not practical nor effective, and that the designers, for this case study, dispose from the capability to rearrange the inner layout of material aiming at a more efficient and less resource-demanding configuration. Discussing then the inner topology distribution, the BESO method has shown to be a robust and practical optimisation method as not only removes material from the geometry but it also adds and redistributes it along all the iterations aiming at the better design by being compliant. Moreover, it offers the capability to set different parameters which are going to lead the path to the final design, meaning that the user disposes with free-choice matter to plan and drive the wanted component towards his idea in mind. Therefore, this tool can be considered very powerful not because of the numerical and computational resources but the free-choice design it offers.

From the analysed mass constraints for the material removal, by using the *Aluminum 6061T*, the higher material reduction reached a 10% of the initial mass, although its final geometrical output looked weak. Therefore, by approaching the case with a conservative view, the 25% constraint was selected to implement the new structural study, so as to check that it can deal with the loading state and that the BESO algorithm has provided a robust result. From this point, the study has shown that the topology optimisation procedure, in order to be able to remove the unnecessary mass, redistributes the inner stresses of the initial filled aerofoil towards the creation of truss structures while reducing the maximum magnitude shown in the non-optimised case as the layout finds by itself a more balanced state. Moreover, the reliability of the final optimised shape is secure when the study shows that the geometry is found inside the safety interval behaviour of the material, highlighting the orders of 10^{-2} for the non-optimised topology structures and 10^{-4} for the opposite ones, when the unity is for the maximal stress loading without failure and null is the non-loaded state.

At the end of the day, the software used provides an idea of the path that should be followed in order to reach specific optimisations targets, but as specified along the thesis, further post-processing work has to be done. For instance, once the aerodynamic shape is optimised, it is only for a specific flight conditions, thus it does not consider the whole flight envelop. Therefore, the technique described in this thesis could be implemented, for instance, into designing the range of modifications that a morphing geometry aerofoil should accomplish along the flight situation to be efficient at all stages. Moreover, apart from the aerodynamic point-of-view, more topology setups should be analysed aiming the structural compliance in the situations described above and, as it is demonstrated in the thesis, the mesh roughness provides to specific elements higher stresses than the ones they realistically support, thus improved outputs could be obtained by using finer meshes and/or keep performing topology optimisations after the previous optimised solution has been put through a new geometry redesign in terms of the optimised case.

8.2 Recommendations and Future Work

As previously introduced before, as future work is recommended to expand the case described in this thesis, beginning with the creation of the flight envelope graph including the different sets of aerodynamic-modified geometries for a 2-D aerofoil. Next and, in order to start from a more realistic and functional study, new geometrical constraints should be defined and the ones set previously in the state of the art, complemented. Then, the case can be expanded to the tridimensional space, thus a wing and all the systems it is related to. By doing so, a noticeable increase in difficulty of the computational process will be required but, using the knowledge of the open-source community and the commercial tools, these drawbacks can be surpassed.

References

[1] Airbus, "Airbus reveals new zero-emission concept aircraft." https://www.airbus.com/newsroom/press-releases/en/2020/09/airbus-reveals-new-zeroemission-concept-aircraft.html. [Online; last accessed 2020-09-29].

[2] T. A. Zang, "Airfoil/Wing Optimization," *Encyclopedia of Aerospace Engineering*, pp. 1–11, 2010.

[3] S. Bagy, B. Mohammadi, M. Meheut, M. Lallia, and P. Coat, "Aerodynamic shape optimization of aircraft engine nozzles based on Computer-Aided Design," no. January, pp. 1–14, 2020. in Proceedings of the AIAA SciTech 2020 Forum, Orlando, FL, 2020.

[4] I. Tyapin, M. Sandberg, M. Kokkolaras, A. Lundbladh, and O. Isaksson, "Jet engine design optimization using a knowledge-based master model," *Proceedings of the ASME Turbo Expo*, vol. 7, no. PARTS A AND B, pp. 41–47, 2012.

[5] L. Zhu, N. Li, and P. R. Childs, "Light-weighting in aerospace component and system design," *Propulsion and Power Research*, vol. 7, no. 2, pp. 103–119, 2018.

[6] S. N. Skinner and H. Zare-Behtash, "State-of-the-art in aerodynamic shape optimisation methods," *Applied Soft Computing Journal*, vol. 62, pp. 933–962, 2018.

[7] A. R. Taherkhani, C. Gilkeson, P. Gaskell, R. Hewson, V. Toropov, A. Rezaienia, and H. Thompson, "Aerodynamic CFD Based Optimization of Police Car Using Bezier Curves," *SAE International Journal of Materials and Manufacturing*, vol. 10, no. 2, 2017.

[8] S. Gholizadeh, A. Barzegar, and C. Gheyratmand, "Shape Optimization of Structures By Modified Harmony Search," pp. 485–494, 2011.

[9] M. E. Aguirre and M. Frecker, "Design innovation size and shape optimization of a 1.0 mm multifunctional forceps-scissors surgical instrument," *Journal of Medical Devices, Transactions of the ASME*, vol. 2, no. 1, pp. 1–7, 2008.

[10] M. Secanell, A. Suleman, and P. Gamboa, "Design of a morphing airfoil using aerodynamic shape optimization," *AIAA Journal*, vol. 44, no. 7, pp. 1550–1562, 2006.

[11] J. Li, Z. Gao, J. Huang, and K. Zhao, “Aerodynamic design optimization of nacelle/pylon position on an aircraft,” *Chinese Journal of Aeronautics*, vol. 26, no. 4, pp. 850–857, 2013.

[12] V. Nejati and K. Matsuuchi, “Aerodynamics design and genetic algorithms for optimization of airship bodies,” *JSME International Journal, Series B: Fluids and Thermal Engineering*, vol. 46, no. 4, pp. 610–617, 2003.

[13] M. W. Lohry, L. Martinelliy, and J. S. Kollasch, “Genetic algorithm optimization of periodic wing protuberances for stall mitigation,” *31st AIAA Applied Aerodynamics Conference*, no. March 2016, 2013.

[14] N. F. Foster and G. S. Dulikravich, “Three-dimensional aerodynamic shape optimization using genetic and gradient search algorithms,” *Journal of Spacecraft and Rockets*, vol. 34, no. 1, pp. 36–42, 1997.

[15] S. K. Nadarajah and A. Jameson, “Studies of the continuous and discrete adjoint approaches to viscous automatic aerodynamic shape optimization,” *15th AIAA Computational Fluid Dynamics Conference*, 2001.

[16] T. D. Economon, J. J. Alonso, T. Albring, and N. R. Gauger, “Adjoint formulation investigations of benchmark aerodynamic design cases in SU2,” *35th AIAA Applied Aerodynamics Conference, 2017*, no. June, pp. 1–13, 2017.

[17] S. K. Nadarajah and A. Jameson, “A comparison of the continuous and discrete adjoint approach to automatic aerodynamic optimization,” *38th Aerospace Sciences Meeting and Exhibit*, 2000.

[18] A. Bueno-Orovio, C. Castro, F. Palacios, and E. Zuazua, “Continuous adjoint approach for the spalart-allmaras model in aerodynamic optimization,” *AIAA Journal*, vol. 50, no. 3, pp. 631–646, 2012.

[19] M. Nemec and M. J. Aftosmis, “Aerodynamic shape optimization using a cartesian adjoint method and CAD geometry,” *Collection of Technical Papers - AIAA Applied Aerodynamics Conference*, vol. 3, no. July, pp. 1423–1437, 2006.

[20] E. I. Amoiralis and I. K. Nikolos, “Freeform deformation versus B-Spline representation in inverse airfoil design,” *Journal of Computing and Information Science in Engineering*, vol. 8, no. 2, pp. 0240011–02400113, 2008.

[21] O. Amoignon, J. Hradil, and J. Navŕatil, “A numerical study of adaptive FFD in aerodynamic shape optimization,” *52nd AIAA Aerospace Sciences Meeting - AIAA Science and Technology Forum and Exposition, SciTech 2014*, no. November, 2014.

[22] J. J. Kingman, K. D. Tsavdaridis, and V. V. Toropov, “Applications of topology optimization in structural engineering.,” *Civil Engineering for Sustainability and Resilience International Conference (CESARE)*, no. November, 2014.

[23] M. P. Bendsøe, “Optimal shape design as a material distribution problem,” *Structural Optimization*, vol. 1, no. 4, pp. 193–202, 1989.

[24] O. M. Querin, G. P. Steven, and Y. M. Xie, “Evolutionary structural optimisation (ESO) using a bidirectional algorithm,” *Engineering Computations (Swansea, Wales)*, vol. 15, no. 8, pp. 1031–1048, 1998.

[25] P. Gomes and R. Palacios, “Aerodynamic Driven Multidisciplinary Topology Optimization of Compliant Airfoils,” no. January, pp. 1–17, 2020.

[26] G. Capasso, J. Morlier, M. Charlotte, and S. Coniglio, “Stress-based topology optimization of compliant mechanisms using nonlinear mechanics,” *Mechanics and Industry*, vol. 21, no. 3, 2020.

[27] L. Xia, Q. Xia, X. Huang, and Y. M. Xie, “Bi-directional Evolutionary Structural Optimization on Advanced Structures and Materials: A Comprehensive Review,” *Archives of Computational Methods in Engineering*, vol. 25, no. 2, pp. 437–478, 2018.

[28] F. Löffelmann, “Failure Index Based Topology Optimization for Multiple Properties,” in *ENGINEERING MECHANICS 2017*, no. May, pp. 15–18, 2017.

[29] J. H. Zhu, W. H. Zhang, and L. Xia, “Topology Optimization in Aircraft and Aerospace Structures Design,” *Archives of Computational Methods in Engineering*, vol. 23, no. 4, pp. 595–622, 2016.

[30] S. Grihon, L. Krog, and K. Hertel, “A380 Weight Savings Using Numerical Structural Optimization,” *Proceedings of 20TH AAAF Colloquium, Material for Aerospace Applications*, pp. 1–16, 2004.

[31] K. Maute, M. Nikbay, and C. Farhat, “Coupled analytical sensitivity analysis and optimization of three-dimensional nonlinear aeroelastic systems,” *AIAA Journal*, vol. 39, no. 11, pp. 2051–2061, 2001.

[32] P. R. Spalart and S. R. Allmaras, “One-equation turbulence model for aerodynamic flows,” *Recherche aerospatiale*, no. 1, pp. 5–21, 1994.

[33] J. D. Anderson, “Fundamentals of aerodynamics.,” 1984.

[34] G. Laccarino, “Simulation of Turbulent Flows.” Center for Turbulence Research, University of Standford, Academic Resources, [Online; accessed 2020-05-12].

[35] B. S. Baldwin and T. J. Barth, “A One-EquationTurbulenceTransport Model for High Reynolds Number Wall-Bounded Flows,” tech. rep., Ames Research Center, NASA, Moffet Field, California, 1990.

[36] L. Nezu and A. TOMINAGA, “Law of the wall.” `https://en.wikipedia.org/wiki/Law_of_the_wall#/media/File:Law_of_the_wall_(English).svg`. [Online; last accessed 2020-09-29].

[37] D. Coles, “The law of the wake in the turbulent boundary layer,” *Journal of Fluid Mechanics*, vol. 1, no. 2, pp. 191–226, 1956.

[38] G. L. Mellor and H. J. Herring, “A study of turbulent boundary layer models Part II, mMellor, G. L., & Herring, H. J. (1971). A study of turbulent boundary layer models Part II, mean turbulent field closure (Issue January).ean turbulent field closure,” Tech. Rep. January, Princeton University, 1971.

[39] L. S. Roberts, M. V. Finnis, and K. Knowles, “Forcing Boundary-Layer Transition on a Single-Element Wing in Ground Effect,” *Journal of Fluids Engineering, Transactions of the ASME*, vol. 139, no. 10, pp. 1–12, 2017.

[40] N. Langley Research Center, “Turbulence Modeling Resource.” https://turbmodels.larc.nasa.gov/spalart.html [Online; last accessed 2020-09-22].

[41] F. Palacios, M. R. Colonno, A. C. Aranake, A. Campos, S. R. Copeland, T. D. Economon, A. K. Lonkar, T. W. Lukaczyk, T. W. Taylor, and J. J. Alonso, “Stanford University Unstructured (SU2): An open-source integrated computational environment for multi-physics simulation and design,” *51st AIAA Aerospace Sciences Meeting including the New Horizons Forum and Aerospace Exposition 2013*, no. January, pp. 1–60, 2013.

[42] D. J. Mavriplis and M. Castagne, “Adjoint-Based Sensitivity Analysis for Computational Fluid Dynamics,” tech. rep., Department of Mechanical Engineering, University of Wyoming, Laramie, WY USA.

[43] D. Hansford, “Chapter 4 - Bézier Techniques,” *Handbook of Computer Aided Geometric Design*, pp. 75–109, 2002.

[44] L. Piegl and W. Tiller, *The NURBS Book (Monographs in Visual Communication)*. 1996.

[45] D. A. Masters, N. J. Taylory, T. C. Rendall, C. B. Allen, and D. J. Poole, “Review of aerofoil parameterisation methods for aerodynamic shape optimisation,” *53rd AIAA Aerospace Sciences Meeting*, no. January, 2015.

[46] T. W. Sederberg and S. R. Parry, “Free-Form Deformation of Solid Geometric Models.,” *Computer Graphics (ACM)*, vol. 20, no. 4, pp. 151–160, 1986.

[47] J.-d. Cao, “A Generalization of the Bernstein Polynomials,” *Journal of Mathematical Analysis and Applications*, vol. 209, pp. 140–146, 1997.

[48] A. Koshakji, A. Quarteroni, G. Rozza, N. Energy, and A. Modeling, “Mathematics Institute of Computational Science and Engineering Free form deformation techniques applied to 3D shape optimization problems,” no. January, 2013.

[49] R. Duvigneau, “Adaptive Parameterization using Free-Form Deformation for Aerodynamic Shape Optimization Régis Duvigneau,” tech. rep., HAL Id: inria-00085058, 2006.

[50] Y. Yang, “Application of Spring Analogy Mesh Deformation Technique in Airfoil Design Optimization,” no. July, 2015.

[51] T. J. Baker and C. Peter A, "Dynamic Adaptation for Deforming Tetrahedral Meshes," *American Institute of Aeronautics and Astronautics*, no. c, 1999.

[52] R. Biswas and R. C. Strawn, "Tetrahedral and hexahedral mesh adaptation for CFD problems," *Applied Numerical Mathematics*, vol. 26, no. 196, pp. 135–151, 1998.

[53] R. Biswas and R. C. Strawn, "A new procedure for dynamic adaption of three-dimensional unstructured grids," *Applied Numerical Mathematics*, vol. 13, no. 6, pp. 437–452, 1994.

[54] X. Huang and Y. M. Xie, "Convergent and mesh-independent solutions for the bi-directional evolutionary structural optimization method," *Finite Elements in Analysis and Design*, vol. 43, no. 14, pp. 1039–1049, 2007.

[55] P. R. Lancaster and D. Mitchell, *Advanced Solid Mechanics*. No. March, 1980.

[56] X. Y. Yang, Y. M. Xie, G. P. Steven, and O. M. Querin, "Bi-directional evolutionary method for stiffness optimisation," *7th AIAA/USAF/NASA/ISSMO Symposium on Multidisciplinary Analysis and Optimization*, vol. 37, no. 11, pp. 1449–1457, 1998.

[57] A. Díaz and O. Sigmund, "Checkerboard patterns in layout optimization," *Structural Optimization*, vol. 10, no. 1, pp. 40–45, 1995.

[58] O. Sigmund, "Design of material structures using topology optimization," *Department of Solid Mechanics*, 1994.

[59] C. G. Pedersen, J. J. Lund, L. Damkilde, and A. S. Kristensen, "Topology Optimization - Improved Checker-Board Filtering With Sharp Contours," *19th Nordic Seminar on Computational Mechanics*, vol. 1, no. 1, 2006.

[60] E. Andreassen, A. Clausen, M. Schevenels, B. S. Lazarov, and O. Sigmund, "Efficient topology optimization in MATLAB using 88 lines of code," *Structural and Multidisciplinary Optimization*, vol. 43, no. 1, pp. 1–16, 2011.

[61] S. Li, D. Zhou, Y. Zhang, and Q. Qu, *Aerodynamic Investigation of RAE2822 Airfoil in Ground Effect*, vol. 126. Elsevier B.V., 2015.

[62] U. A. A. Group, "UIUC Airfoil Data Site." https://m-selig.ae.illinois.edu/ads/coord_database.html [Online; last accessed 2020-09-22].

[63] S. R. Allmaras, V. Venkatakrishnan, and F. T. Johnson, "Farfield boundary conditions for 2-D airfoils," *17th AIAA Computational Fluid Dynamics Conference*, no. June, pp. 1–15, 2005.

[64] KTH Royal Institute of Technology in Stockholm, "Boundary Conditions." Academic Resources, [Online; last accessed 2020-07-01].

[65] North Atlantic Treaty Organization. Advisory Group for Aerospace Research and Development. Fluid Dynamics Panel. Working Group 04., "Experimental data base for computer program assessment," tech. rep., 1979.

[66] F. Palacios, T. D. Economon, A. C. Aranake, S. R. Copeland, A. K. Lonkar, T. W. Lukaczyk, D. E. Manosalvas, K. R. Naik, A. Santiago Padrón, B. Tracey, A. Variyar, and J. J. Alonso, "Stanford university unstructured (SU2): Open-source analysis and design technology for turbulent flows," *52nd Aerospace Sciences Meeting*, no. January, pp. 1–33, 2014.

[67] O. J. Chit, A. A. Omar, and W. Asrar, "Reynolds Averaged Navier-Stokes Flow Computation of RAE2822 Airfoil Using Gas-kinetic BGK Scheme," *Lecture Notes in Engineering and Computer Science*, vol. 2175, no. 1, pp. 2179–2183, 2009.

[68] AMAG Rolling GmbH, "Amag Advanced Aa6061 Alloy for Aerospace Applications," *AluReport*, pp. 12–13, 2012.

[69] M. S. Wilk and R. E. Sliwa, "The influence of features of aluminium alloys 2024, 6061 and 7075 on the properties of glare-type composites," *Archives of Metallurgy and Materials*, vol. 60, no. 4, pp. 3101–3108, 2015.

[70] O. Sigmund, "Morphology-based black and white filters for topology optimization," *Structural and Multidisciplinary Optimization*, vol. 33, no. 4-5, pp. 401–424, 2007.

[71] K. E. Tatum and J. W. Slater, "The Validation Archive of the NPARC Alliance, AIAA 99-0747," in *37th AIAA Aerospace Sciences Meeting and Exhibit*, 1999.

[72] N. U. Guide, T. N-dimensional, I. O. Arrays, T. A. Interface, C. Rules, and O. Ufunc, "NumPy Reference," 2020.

[73] SciPy Community, "SciPy Reference Guide 0.7," p. 1229, 2013.

[74] G. Yang, A. Da Ronch, J. Drofelnik, and Z. T. Xie, "Sensitivity assessment of optimal solution in aerodynamic design optimisation using SU2," *Aerospace Science and Technology*, vol. 81, pp. 362–374, 2018.

[75] S. Nadarajah, "Aerodynamic Design Optimization: Drag Minimization of the RAE 2822 in Transonic Viscous Flow," tech. rep., Montreal, Canada, 2013.

Appendix A

Matlab® script used to connect SU2 with Calculix

```
%%%%%%%%%%%%%%%%%%%%%%%%%%%%%%%%%%%%%%%%%%%%%%%%%%%%%%%%%%%%%%%%%%%%%%%%%%%%%%%%
%                                                                               %
%% %%%%%%%%%%%%%%%%%%%   AUTHOR:   ISAAC GIBERT MARTINEZ   %%%%%%%%%%%%%%%%%%%
%%%%%%%%%%%%%%%%%%%%%%%         DATE: NOVEMBER 2020         %%%%%%%%%%%%%%%%%%%%
%                                                                               %
%%                                MASTER THESIS:                               %%
%%%%%%%%%%%%%%%%%%%%%%%%%%%%%%%%%%%%%%%%%%%%%%%%%%%%%%%%%%%%%%%%%%%%%%%%%%%%%%%%
%                                                                               %
%       AERODYNAMIC OPTIMISATION OF A CONSTRAINED AEROFOIL'S SHAPE              %
%      COUPLED WITH AN OPTIMISATION OF ITS INNER STRUCTURAL TOPOLOGY            %
%                                                                               %
%%%%%%%%%%%%%%%%%%%%%%%%%%%%%%%%%%%%%%%%%%%%%%%%%%%%%%%%%%%%%%%%%%%%%%%%%%%%%%%%
%                                                                               %
%%%%%%%%%%       SCRIPT DEVELOPED TO PROCESS THE DATA FROM SU2      %%%%%%%%%%
%%%%%%%%%%  (*.csv) FILE INTO CALCULIX (ABACUS *.inp) ENVIRONMENT  %%%%%%%%%%
%                                                                               %
% ----------------------------------------------------------------------------- %
%%                         INSTITUTO TECNICO LISBOA IST                        %%
%%%%%%%%%%%%%%%%%%%%%%%%%%%%%%%%%%%%%%%%%%%%%%%%%%%%%%%%%%%%%%%%%%%%%%%%%%%%%%%%

clear all
clc

% ----------------------------------------------------------------------------- %
%% Data Acquisition from SU2 using Paraview to provide the CSV file
surfDATA = readtable('CSVFile.csv', 'HeaderLines', 1);
surfaceData = table2array(surfDATA);

% ----------------------------------------------------------------------------- %
%% Data treatment and post-processing

% Add/Remove/Modify the problematic aerofoil nodes

% ----------------------------------------------------------------------------- %
%% New *.geo file for GMSH as some nodes have been moved/removed/modified

% GEOMETRICAL DIFFERENTIATION FOR POST-PROCESSING PURPOSES
wingboxUP = [surfaceData(65:137,12), surfaceData(65:137,13)];
wingboxLOW = [surfaceData(268:340,12), surfaceData(268:340,13)];

% GENERATION OF *.TXT FILE CONTAINING THE NODES POSITION FOR GMSH
fileID2 = fopen('SurfaceTOGeoFile_MCinit.txt','w');

% PRINTING OF VALUES:
```

```
for i=1:length(surfaceData)
    % ------------ ALL NODES CHARACTERISATION %
    % -------- formatSpec => Point(ID_NODE) = {x, y, z, Size}; --------- %
   compt = i;
   fprintf(fileID2, 'Point(%.0f) = {%.8f, %.8f, 0, Size};\n', ...
       surfaceData(i,24), surfaceData(i,12), surfaceData(i,13));
end

for i=1:length(wingboxUP)
    % ------------ UPPER WING-BOX NODES CHARACTERISATION %
    % ------------ formatSpec = Point(i) = {x, y, z, Size}; ----------- %
   compt = 1000;        % NEW 'ID_NODE' FOR CLARITY PURPOSES
   fprintf(fileID2, 'Point(%.0f) = {%.8f, %.8f - dist, 0, Size};\n', ...
       compt+i, wingboxUP(i,1), wingboxUP(i,2));
            % 'dist' is the vertical translation from the aerofoil
                % surface nodes to the wing-box
end

for i=1:length(wingboxLOW)
    % ------------ UPPER WING-BOX NODES CHARACTERISATION %
    % ------------ formatSpec = Point(i) = {x, y, z, Size}; ----------- %
   compt = 2000;        % NEW 'ID_NODE' FOR CLARITY PURPOSES
   fprintf(fileID2, 'Point(%.0f) = {%.8f, %.8f + dist, 0, Size};\n', ...
       compt+i, wingboxLOW(i,1), wingboxLOW(i,2));
            % 'dist' is the vertical translation from the aerofoil
                % surface nodes to the wing-box
end

% CLOSE GENERATED *.TXT FILE
fclose(fileID2);

% ------------------------------------------------------------------------- %
%% Pre-Processing of the CFD results
% Final separation between upper and lower sides of the aerofoil
    % The values '200' and '201' depend on the used mesh
upperData = surfaceData(1:200,:);
lowerData = surfaceData(201:end,:);


% Sort by x-position in both sides
    % UPPER
[~,s] = sort(upperData(:,12));
A = upperData(s,:);
upperData = A;
    % LOWER
[~,r] = sort(lowerData(:,12));
B = lowerData(r,:);
lowerData = B;

% SAVING pressure loads for each of the nodes from the classified data
pvalue_UP = upperData(:,16);
nodesID_UP = upperData(:,24);

pvalue_LOW = lowerData(:,16);
nodesID_LOW = lowerData(:,24);

% ------------------------------------------------------------------------- %
%% Position vectors used for obtaining the force by the pressure values

    % INITIALISATION OF THE ARRAYS
SEGMENTUp = zeros(length(lowerData)-1, 1);  % Segment length variable
normalUp = zeros(length(lowerData)-1, 2);   % Normal vector variable
    % USE OF THE PREVIOUS DATA
xUp = upperData(:,12);
yUp = upperData(:,13);
lengtharrayUP = (length(upperData));

for i=1:(lengtharrayUP-1)
   dxUp = xUp(i+1) - xUp(i);    % X-Distance
   dyUp = yUp(i+1) - yUp(i);    % Y-Distance
   alpha = dyUp/dxUp;           % Angle
```

```
   cosAlpha = cos(alpha);
   sinAlpha = sin(alpha);

   x = dxUp*dxUp;
   y = dyUp*dyUp;
   dist = x + y;
   SEGMENTUp(i) = sqrt(dist);   % Length of the Segment

   xnorm = dyUp;
   ynorm = -dxUp;
   nx = xnorm/SEGMENTUp(i);
   ny = ynorm/SEGMENTUp(i);
   normalUp(i,:) = [nx, ny];    % Normal Vector of the Segment
end

    % ---------- ANALOG PROCEDURE FOR THE LOWER SIDE NODES --------- %
SEGMENTLow = zeros(length(lowerData)-1, 1);
normalLow = zeros(length(lowerData)-1, 2);

xLow = lowerData(:,12);
yLow = lowerData(:,13);
lengtharrayLow = (length(lowerData));

for i=1:(lengtharrayLow-1)
   dxLow = xLow(i+1) - xLow(i);
   dyLow = yLow(i+1) - yLow(i);
   alphaLow = dyLow/dxLow;
   cosAlphaL = cos(alphaLow);
   sinAlphaL = sin(alphaLow);

   xL = dxLow*dxLow;
   yL= dyLow*dyLow;
   lengthSegL = xL + yL;
   SEGMENTLow(i) = sqrt(lengthSegL);

   xnormL = dyLow;
   ynormL = -dxLow;
   nxL = xnormL/SEGMENTLow(i);
   nyL = ynormL/SEGMENTLow(i);
   normalLow(i,:) = [nxL, nyL];
end

        % ---------- ANALOG PROCEDURE FOR THE BOUNDARY NODES --------- %
% Leading Edge
dxLE = xUp(1) - xLow(1);
dyLE = yUp(1) - yLow(1);
alphaLE = dyLE/dxLE;
cosAlphaLE = cos(alphaLE);
sinAlphaLE = sin(alphaLE);

xLE = dxLE*dxLE;
yLE= dyLE*dyLE;
lengthSegLE = xLE + yLE;
SEGMENTLE = sqrt(lengthSegLE);
xnormLE = -dyLE;
ynormLE = dxLE;

nxLE = xnormLE/SEGMENTLE;
nyLE = ynormLE/SEGMENTLE;
normalLE = [nxLE, nyLE];

% Trailing Edge
dxTE = xUp(end) - xLow(end);
dyTE = yUp(end) - yLow(end);
alphaTE = dyTE/dxTE;
cosAlphaTE = cos(alphaTE);
sinAlphaTE = sin(alphaTE);

xTE = dxTE*dxTE;
yTE = dyTE*dyTE;
lengthSegTE = xTE + yTE;
```

```
SEGMENTTE = sqrt(lengthSegTE);
xnormTE = dyTE;
ynormTE = dxTE;

nxTE = xnormTE/SEGMENTTE;
nyTE = ynormTE/SEGMENTTE;
normalTE = [nxTE, nyTE];

% ------------------------------------------------------------------------- %
%% Load provided by the pressure
% It is considered that the pressure is applied at the correspondent node
% but the surface used to apply the load is the sum of the halves of the
% contiguous segments: LENGTH = (X1 + X2)/2
%    ( NODE_I-1 )  <~~~~~X1~~~~~>  ( NODE_I )  <~~~X2~~~>  ( NODE_I+1 )
% Moreover, the 2nd dimension is considered to be the unity as the case is
% 2D::: F = P * A = P * avg(dist) * 1

% ARRAYS INITIALISATION
LoadUP = zeros(1,lengtharrayUP);
LoadLOW = zeros(1,lengtharrayLow);
LoadUP_X = zeros(1,lengtharrayUP);
LoadUP_Y = zeros(1,lengtharrayUP);
LoadLOW_X = zeros(1,lengtharrayLow);
LoadLOW_Y = zeros(1,lengtharrayLow);

% ---------------------------- Leading Edge Nodes ----------------------------%

                avgDistLEUp = SEGMENTLE/2 + SEGMENTUp(1)/2;
                LoadUP(1) = -pvalue_UP(1)*avgDistLEUp;

                avgDistLELow = SEGMENTLE/2 + SEGMENTLow(1)/2;
                LoadLOW(1) = -pvalue_LOW(1)*avgDistLELow;

                LoadUP_X(1) = LoadUP(1)*normalLE(1,1);
                LoadUP_Y(1) = LoadUP(1)*normalLE(1,2);
                LoadLOW_X(1) = LoadLOW(1)*normalLE(1,1);
                LoadLOW_Y(1) = LoadLOW(1)*normalLE(1,2);

% ---------------------------- Trailing Edge Nodes----------------------------%

                avgDistTEUp = SEGMENTTE/2 + SEGMENTUp(end-1)/2;
                LoadUP(end) = -pvalue_UP(end)*avgDistTEUp;

                avgDistTELow = SEGMENTTE/2 + SEGMENTLow(end-1)/2;
                LoadLOW(end) = pvalue_LOW(end)*avgDistTELow;

                LoadUP_X(end) = LoadUP(end)*normalTE(1,1);
                LoadUP_Y(end) = LoadUP(end)*normalTE(1,2);
                LoadLOW_X(end) = LoadLOW(end)*normalTE(1,1);
                LoadLOW_Y(end) = LoadLOW(end)*normalTE(1,2);

% ---------------------------- For the Rest of the Nodes ---------------------%

for i=2:(lengtharrayUP-1)
                    avgDistUP = SEGMENTUp(i-1)/2 + SEGMENTUp(i)/2;
                    LoadUP(i) = pvalue_UP(i)*avgDistUP;

                    LoadUP_X(i) = LoadUP(i)*normalUp(i,1);
                    LoadUP_Y(i) = LoadUP(i)*normalUp(i,2);

                    PXu(i) = pvalue_UP(i)*normalUp(i,1);
                    PYu(i) = pvalue_UP(i)*normalUp(i,2);
end

for i=2:(lengtharrayLow-1)
                    avgDistLOW = SEGMENTLow(i-1)/2 + SEGMENTLow(i)/2;
                    LoadLOW(i) = -pvalue_LOW(i)*avgDistLOW;

                    LoadLOW_X(i) = LoadLOW(i)*normalLow(i,1);
                    LoadLOW_Y(i) = LoadLOW(i)*normalLow(i,2);

```

```
                    PXl(i) = pvalue_LOW(i)*normalLow(i,1);
                    PYl(i) = pvalue_LOW(i)*normalLow(i,2);
end

% ------------------------------------------------------------------------- %
%% Writing the *.txt file

% NEW *.TXT FILE USED AS AN INPUT FOR CALCULIX NOMENCLATURE (ABACUS *.INP)
fileID = fopen('Su2_to_Calculix_LOADS.txt','w');

for i=1:lengtharrayUP

    % -----formatSpec = 'Node%.0f, axis-direction, Magnitude%6.1f \n'; ---- %
   fprintf(fileID, '%.0f, 1, %8.4f \n', nodesID_UP(i,1), LoadUP_X(i));
   fprintf(fileID, '%.0f, 2, %8.4f \n', nodesID_UP(i,1), LoadUP_Y(i));
end

for i=1:lengtharrayLow

    % -----formatSpec = 'Node%.0f, axis-direction, Magnitude%6.1f \n'; ---- %
   fprintf(fileID, '%.0f, 1, %8.4f \n', nodesID_LOW(i,1), LoadLOW_X(i));
   fprintf(fileID, '%.0f, 2, %8.4f \n', nodesID_LOW(i,1), LoadLOW_Y(i));
end

% SAVE AND CLOSE GENERATED FILE
fclose(fileID);

% ------------------------------------------------------------------------- %
%% TOPOLOGY OPTIMISATION  ----------> INCLUDES:
% AEROFOIL SKIN for topology optimisation BOUNDARY CONSTRAINT ::> 2mm
% WING-BOX SKIN for topology optimisation BOUNDARY CONSTRAINT ::> 2mm

                % Save data into new variables
skinUP = [upperData(4:184,12), upperData(4:184,13)];
skinLOW = [lowerData(4:181,12), lowerData(4:181,13)];
distSkin = 0.002;

    % RE-OPEN GMSH GEOMETRIC INPUT FILE TO PRINT THE SKIN CONSTRAINT
fileID2 = fopen('SurfaceTOGeoFile.txt','w');

           % FIRST node UPPER (LE) needs a different treatment
fprintf(fileID2, 'Point(6000) = {%.8f + distSkin, %.8f, 0, Size};\n',...
       skinUP(1,1), skinUP(1,2));
skinU(1,:) = [upperData(1,12) + 0.4*distSkin, upperData(1,13)- 0.4*distSkin];

                        % GENERAL UPPER NODES
for i=2:length(skinUP)

        % -------- formatSpec = Point(i) = {x, y, z, Size}; --------- %
   compt = 6000;        % NEW 'ID_NODE' FOR CLARITY PURPOSES
   fprintf(fileID2, 'Point(%.0f) = {%.8f, %.8f - distSkin, 0, Size};\n',...
       compt+i, skinUP(i,1), skinUP(i,2));
   skinU(i,:) = [skinUP(i,1), skinUP(i,2) - distSkin]; % VERTICAL DISPL.
end

           % FIRST node LOWER (LE) needs a different treatment
fprintf(fileID2, 'Point(7000) = {%.8f + distSkin, %.8f, 0, Size};\n',...
       skinLOW(1,1), skinLOW(1,2));
skinL(1,:) = [lowerData(1,12)+ 0.4*distSkin, lowerData(1,13)];

                        % GENERAL LOWER NODES
for i=2:length(skinLOW)
%    formatSpec = Point(i) = {x, y, z, Size};
   compt = 7000;        % NEW 'ID_NODE' FOR CLARITY PURPOSES
   fprintf(fileID2, 'Point(%.0f) = {%.8f, %.8f - distSkin, 0, Size};\n',...
       compt+i, skinLOW(i,1), skinLOW(i,2));
   skinL(i,:) = [skinLOW(i,1), skinLOW(i,2) + distSkin]; % VERTICAL DISPL.
end


    % GMSH GEOMETRIC INPUT FILE TO PRINT THE WING-BOX SKIN CONSTRAINT
```

```
for i=1:length(wingboxUP)

        % ------ formatSpec = Point(i) = {x, y, z, Size}; ------ %
   compt = 8000;        % NEW 'ID_NODE' FOR CLARITY PURPOSES
   fprintf(fileID2, 'Point(%.0f) = {%.8f, %.8f - distWB, 0, Size};\n', ...
       compt+i, wingboxUP(i,1), wingboxUP(i,2));        % VERTICAL DISPL.
end

for i=1:length(wingboxLOW)

        % ------ formatSpec = Point(i) = {x, y, z, Size}; ------ %
   compt = 9000;        % NEW 'ID_NODE' FOR CLARITY PURPOSES
   fprintf(fileID2, 'Point(%.0f) = {%.8f, %.8f + distWB, 0, Size};\n', ...
       compt+i, wingboxLOW(i,1), wingboxLOW(i,2));      % VERTICAL DISPL.
end
% ------------------------------------------------------------------------ %
```